Microscale Infrared Technologies for Spectral Filtering and Wireless Neural Dust

by

Michael Barrow

A dissertation submitted in partial fulfillment
of the requirements for the degree of
Doctor of Philosophy
(Electrical and Computer Engineering)
in the University of Michigan
2021

Doctoral Committee:

Professor David Blaauw, Co-Chair
Professor Jamie Phillips, Co-Chair
Associate Professor Cynthia Chestek
Professor Anthony Grbic

Michael Barrow

barrowm@umich.edu

ORCID iD: 0000-0002-4038-3451

© Michael Barrow 2021

ACKNOWLEDGMENTS

This dissertation would not be possible without the support and guidance of many. Thank you to everyone who helped me grow as a researcher and made this such a worthwhile experience.

I am forever grateful for the invitation to join Professor Phillips's research group. In every situation Professor Phillips was fully supportive in both professional and personal matters. His genuine care extends beyond our group, enriching countless graduate and undergraduate students. The many opportunities to collaborate on a broad range of topics has been critical to my growth. I appreciate his trust in me to tackle these difficult questions, and his patience during the endless challenges of experimental work.

I would also like to recognize my teammates on the NIH Brain Initiative "ReMote" project. I thank the investigators for offering me this special opportunity, and in particular Professor Blaauw and Professor Chestek for their mentorship and for serving on my thesis committee. It was great to work with you all.

I would like to thank Piyush Shah and Robert Woods of the Air Force Research Lab. They shared several interesting research problems and are excellent collaborators.

Furthermore, I thank the Rackham Graduate School for the Rackham Merit Fellowship and travel grants. Without their financial assistance to attend conferences, I would not have half of the confidence that I do today.

Past and present members of the Phillips research group helped make these past five years a fulfilling experience. For their interesting discussion (technical and otherwise), I would like to thank Eunseong Moon, Hannah Masten, Minhyung Ahn, Justin Easley, Armando Gil, Rebecca Lentz, Marty Scherr, Arynn Gallegos, and Sarah Puzycki. Eunseong Moon deserves special recognition for his invaluable mentorship. I am glad I was able to meet you all.

Many others in the College of Engineering helped make this dissertation possible. I would like to thank Professor Grbic for taking the time to join my thesis committee and for instructing a very interesting course on electromagnetic metamaterials. On several occasions, Steve Young took time from his day to assist with electromagnetic modeling. I would like to acknowledge Jongyup Lim, Joseph Letner, and Joseph Costello for their expertise and for being a pleasure to work with. I thank Kishwar Mashooq for being a top-notch friend and colleague. Lastly, I would like to thank the Department of Electrical Engineering staff for keeping everything running smoothly while we conduct research.

Next, I want to recognize the staff at the Lurie Nanofabrication Facility. The University of Michigan would not be a leader in solid state devices without their hard work and professionalism. During the experiments in this dissertation, the number of issues resolved by LNF staff are too many to recount.

My parents, Laura and Richard, taught me to follow the hard path and have given their unwavering love along every step of the way. Finally, I thank my partner, Jenna, for undertaking so much while still supporting my goals and making me laugh everyday. I love you all.

TABLE OF CONTENTS

Acknowledgments . . . . **ii**

List of Figures . . . . **vii**

List of Tables . . . . **xiii**

Abstract . . . . **xiv**

Chapter

1 Introduction **1**

1.1 Microscale Infrared Technologies 1
1.2 Dielectric Subwavelength Gratings 2
1.3 Wireless Neural Motes 6
1.4 Thesis Organization 9

2 Symmetric Subwavelength Grating Transmittance Filters **11**

2.1 Fundamental Principles 11
2.1.1 The Resonant Subwavelength Region 11
2.1.2 Homogeneous Slab Analysis 14
2.1.3 Guided Mode Resonant Gratings 15
2.2 Characteristics of Guided Mode Resonances in SWGs 16
2.2.1 Symmetry-Protected Modes 16
2.2.2 Resonance Linewidth 18
2.2.3 Angular Tolerance 18
2.3 Subwavelength Grating Geometries 19
2.4 Experimental Methods 21
2.4.1 Numerical Modeling 21
2.4.2 Subwavelength Grating Fabrication 24
2.4.3 Optical Characterization 25
2.5 1D Zero-Contrast Grating MWIR Transmittance Filters 26
2.6 2D Zero-Contrast Grating MWIR Transmittance Filters 29
2.7 Effects of Finite Periodicity 32

3 GaAs High-Contrast Grating Transmission Filters **37**

3.1 Introduction 37
3.2 HCG Design 38

3.3 Grating Fabrication . . . 40
3.3.1 GaAs Dry Etch . . . 40
3.3.2 Gratings Release . . . 42
3.4 Optical Performance . . . 44

4 Access to Symmetry-Protected Modes in Asymmetric Subwavelength Gratings . . . 48

4.1 Background . . . 48
4.1.1 Photonic Bound States in the Continuum . . . 48
4.1.2 Group Theoretical Analysis . . . 50
4.2 Two-Step Asymmetric Gratings . . . 51
4.2.1 Design . . . 51
4.2.2 Diffraction Efficiency Symmetry . . . 53
4.2.3 Fano Analysis . . . 54
4.2.4 Experimental Two-Step HCGs . . . 59
4.3 Reduced Symmetry Hexagonal Gratings . . . 62
4.3.1 Reduced Symmetry Square Grating . . . 63
4.3.2 Reduced Symmetry Hexagonal Grating . . . 65

5 Emission and Propagation of Infrared Light in Subcranial Tissue . . . 69

5.1 Introduction . . . 69
5.2 Monte Carlo Simulations of NIR Propagation in Tissue . . . 71
5.2.1 Model Details . . . 71
5.2.2 NIR Link Efficiency . . . 72
5.3 Experimental Pulse Detection . . . 75
5.3.1 Experimental Setup . . . 75
5.3.2 Empirical Pulse Detection Probability . . . 78

6 Hybrid Integration of GaAs-Based Optoelectronic Devices and Si CMOS Chips for Neural Systems . . . 81

6.1 Mote Assembly Overview . . . 81
6.2 GaAs Through-Wafer Vias . . . 83
6.2.1 Via Hole Definition . . . 83
6.2.2 Thin Film TWVs . . . 85
6.2.3 Seed Layer Patterned TWVs . . . 86
6.2.4 Selective Damascene Plating . . . 88
6.3 Blind Si Vias for Carbon Fiber Probe Insertion . . . 91
6.4 Heterogeneously Integrating GaAs and Si CMOS Chips . . . 94

7 Future Work and Conclusions . . . 98

7.1 Hyperspectral Imaging via Subwavelength Grating Filters . . . 98
7.2 Neural Mote Assembly . . . 99
7.2.1 Heterogeneous Integration . . . 99
7.2.2 Mote Singulation . . . 100
7.2.3 Carbon Fiber Probe Insertion . . . 101
7.2.4 Mote Encapsulation . . . 103
7.3 The ”Last Millimeter” Gap of the Neural Dust Interface . . . 103

7.4 Enhancing LED Light Extraction Efficiency 104
7.5 Conclusions 105

Appendix **108**

Bibliography **119**

LIST OF FIGURES

FIGURE

1.1 IR spectrum and important wavelengths. The two red curves are approximate black-body radiation spectra corresponding to objects at 5770 K and 300 K. 1
1.2 Schematic of a conventional dielectric subwavelength grating. 3
1.3 (left) SEM micrograph of cross-sectioned silicon-on-sapphire GMR grating. (right) Angular-dependent reflectance spectra. Figures are published in [9]. 4
1.4 Transmittance spectrum of the Earth's atmosphere showing the resonant absorption wavelengths for common gaseous molecules. 5
1.5 Schematic of a hyperspectral imaging pixel. 6
1.6 Progress in neural interface scaling. The smallest device (labeled [38] in the figure) was published by Lim et al. at the University of Michigan [84]. Figure is adopted from [83]. Reference labels apply to original publication. 8
1.7 Schematic of the wireless neural dust system showing subdural implanted motes, NIR power and data uplink, and subcranial repeater unit. b) Schematic of an implanted wireless neural dust mote. Figure is referenced from [87]. 9

2.1 Schematic of guided mode resonance, the coupling of incident light into quasi-guided modes. The background image is an SEM cross-section of a SWG filter. 12
2.2 Simulated transmittance spectra of a slab waveguide and a SWG. The effective index of the slab waveguide is given by Equation 2.3. The thickness, t, is the same in each case. 13
2.3 a) Schematic of a slab waveguide. (b,c) Dispersion relations of b) a slab waveguide and c) a SWG. Blue(green) curves correspond to TE(TM) modes. The black line is the light line. 14
2.4 Illustration of symmetry mismatch between a normally incident plane wave and a resonant mode with odd field symmetry. Mirror symmetries are referenced to the yz-plane, as depicted by the dashed black line. The angle θ is the polar angle of incidence. 17
2.5 a) Simulated transmittance spectra of a rectangular SWG for varying angle of incidence. b) SWG dispersion near zone center (Γ-point). The red line is the light line at $\theta = 9°$. 18
2.6 a,c) The two ”high-contrast grating” definitions. b) A ”low-contrast grating”. d) A ”zero-contrast grating”. The dashed yellow line signifies the interface referred to by the high-/zero- contrast distinction. 20
2.7 Meshed FEM models of 1D and 2D SWG unit cells with labels for the excitation (top) port, listener (bottom) port, and periodic boundary conditions. 22

2.8 SWG geometry optimization via a genetic algorithm. a) Solution convergence as a function of iteration number. b) High-level flow chart of the genetic algorithm. 23
2.9 Basic SWG microfabrication process flow. a) Thin device layer to target thickness b) Clean substrate with solvents and a plasma descum. c) Apply adhesion promoter and spin photoresist. d) Expose and develop grating pattern. (e,f) Dry etch to define e) ZCGs and f) HCGs. g) Dip in HF to release HCGs from the etch stop. 24
2.10 Schematic of the FTIR optical setup. 26
2.11 a) Schematic of surface smoothing by thermal oxidation and etching. b) AFM images of the ZCG surface before and after the oxidation and etch treatment. 27
2.12 a) Scanning electron micrograph of a cross-sectioned air/Si/SiO_2 ZCG MWIR transmittance filter. b) Experimental transmittance spectrum of ZCG in (a). The insets show FEM-calculated field profiles for the resonances at 4.45 µm and 4.6 µm. Figure referenced from [68]. 28
2.13 Experimental transmittance spectra showing the effects of surface smoothing. 28
2.14 a) Schematic of a ZCG, defining polarization states and incidence angles. b) Grating response for varying polar angle θ for fixed $\phi = 0°$. c) Grating response for varying azimuthal angle ϕ for fixed $\theta = 6°$. Figure referenced from [68]. 29
2.15 Experimental transmittance spectra of the 1D ZCG for TE- and TM-polarization and an intermediate polarization $(45°)$ containing equal TE and TM components. 30
2.16 Schematic of a polarization-independent MWIR transmittance filter via a square lattice ZCG. 31
2.17 a) Tilted SEM image of a square array 2D air/Si/SiO_2 ZCG. b) Simulated transmittance spectrum (dotted curve) and experimental transmittance spectra (solid curves) for orthogonal incident polarization states. c) Experimental transmittance spectra for ZCG with two different periods. Figure referenced from [68]. 31
2.18 Resonant H-field profile for a HCG with 40 periods. 32
2.19 Simulated transmittance spectra for finite HCGs under a) near-normal and b) highly oblique incidence conditions. The spectra include HCGs with varying numbers of periods (simulated in a finite domain) compared to one of indefinite periodicity. Figure referenced from [69]. 33
2.20 a) Quality factor (Q) and peak transmittance (T_{peak}) as a function of number of periods. b) Experimental transmittance spectra for varying number of periods. Each grating is 180 µm long. The angle of incidence is $\theta =\approx \pm 3°$ and $\phi =\approx 14 - 20°$. . . . 34
2.21 Quality factor (Q) and peak transmittance (T_{peak}) as a function of grating length. b) Experimental transmittance spectra as a function of grating length. Each grating is 40 periods. The angle of incidence is $\theta =\approx \pm 3°$ and $\phi =\approx 14 - 20°$. 35
2.22 a) Schematic of a CRIGF employing gold metallic reflectors. b) Simulated transmittance spectra comparing the CRIGF to finite and infinitely periodic HCG filters. The SWG parameters are Λ = 4.68 µm, FF = 0.65, t_g = 2.82 µm, and t_s = 1.66 µm. The finite grating and CRIGFs have 15 periods. 36

3.1 Schematic of a suspended GaAs/AlGaAs HCG. The etch stop layer is $Al_{0.9}Ga_{0.1}As$ before an HF dip, and air after. 38
3.2 a) Simulated transmittance spectra for varying air gap heights, t_a. b) Normalized E-field for three representative air gaps on resonance (λ = 5.85 µm). 39

3.3 a) SEM cross-section of a HCG after the GaAs RIE step. b) Top-down SEM image of grating lines. 41
3.4 SEM image of an isolated grating line showing the Si-rich passivation layer. An isolated line is imaged for visibility, as the passivation thickness decreases with aspect ratio. 42
3.5 Top-down SEM images of 115 μm and 50 μm long HCGs after the release step. Images are taken near the center of the gratings. The white dashed circle draws attention to bowing. 43
3.6 Statistical distribution of the measured trench widths for varying HCG lengths. Measurements are extracted from SEM images such as those in Figure 3.5. Images are taken near the center of the gratings and are averaged over 10 measurements. 43
3.7 Simulated transmittance spectra for GaAs HCGs with varying sidewall slope. 44
3.8 a) Experimental and simulated transmittance spectra for a suspended GaAs/AlGaAs HCG. b) Experimental transmittance spectra for HCGs with varying *FF*. c) Measured *Q* and peak transmittance for the curves in (b). All measurements refer to HCGs 90 μm long with Λ = 3.15 μm and are referenced to an air background. 45
3.9 Figure 3.8b remeasured with a GaAs handle wafer reference. 46

4.1 a) Illustration of a SWG showing a guided mode resonance and the continuum of radiative states. Incident light has a continuous distribution for incident angle, θ, and wavenumber, $k_0 = 2\pi/\lambda$. b) SWG dispersion relation showing discrete, bound states within the radiative continuum (yellow region). 49
4.2 a) Illustration of the transverse component of the magnetic field of the first-order stable BIC (for TM-polarization) in a rectangular SWG. b) Components of a normally incident TM-polarized plane wave. Both (a) and (b) define reflection symmetry planes (σ_j) and 180° rotational symmetry axes (C_{2j}), where *j* is one of the Cartesian directions. 50
4.3 Schematic of the two-step asymmetric HCG. Figure referenced from [43]. 52
4.4 a) H-field profiles for a two-step HCG at three representative step heights. (b, c) Simulated transmittance spectra for varying step b) height and c) width. Figure referenced from [15]. 53
4.5 a) Diffraction in a two-step HCG. (b, c) Scattering parameters for b) symmetric (t_s = 0) and c) asymmetric (t_s = 0.017λ_0) HCGs at normal incidence. Figure referenced from [70]. 54
4.6 Fano lineshape for three values of the asymmetry factor, q. 56
4.7 Extracted *Q* and peak transmittance as a function of step height. Equation 4.5 is fit to a numerical transmittance spectra at normal incidence with $\kappa_{Si} = 1 \times 10^{-4}$. Figure referenced from [15]. 57
4.8 a) Relationship between the total decay rate, γ, and the absorption probability, η_{abs} as a function of step height. b) Step height optimization via an ad hoc figure of merit, $Q \times T_{peak}$. Figure referenced from [15]. 58
4.9 Ratio of the radiation probabilities for ports 1 and 2 for varying step heights. (inset) Absorbance spectra near resonance for light incident from above and below the gratings. 59
4.10 SEM images of a cross-sectioned silicon two-step HCG. Figure referenced from [43]. . 60
4.11 a) Comparison of measured and simulated transmittance spectra. b) Peak wavelength tuning by lithographically varying the grating period. Figure referenced from [43]. . . 61

4.12 Measured transmittance spectra of two-step HCG with varying step heights. Figure referenced from [15]. . . . 62
4.13 a) Unit cell of the C_s symmetry square lattice SWG. b) Simulated transmittance spectra of symmetric and asymmetric (C_s) square lattice SWGs. . . . 64
4.14 a) Definition of polarization directions in the C_s symmetry square lattice SWG. b) Simulated transmittance spectra for three high-symmetry polarization states. . . . 64
4.15 Schematic of the reduced symmetry hexagonal grating from a) perspective and b) top-down viewpoints. The E-field is parallel to the plane of incidence in the "in-plane" polarization state. The parameter p is the polarization angle. Figure referenced from [70]. . . . 65
4.16 a) Simulated transmittance spectra as a function of the asymmetry parameter, a, at normal incidence. b) Normal incidence transmittance spectrum for the parameters FF = 0.826, $t = 0.224\Lambda$, and $a = 0.006\Lambda$. The inset shows the out-of-plane E-field profile at the $\lambda = 1.26\Lambda$ resonance. Figure referenced from [70]. . . . 66
4.17 a) Reduced symmetry hexagonal grating schematic with definition of first-order diffraction vectors and polarization angle, p. b) Simulated out-of-plane scattering parameters at normal incidence and $p = 0°$. The grating parameters are FF = 0.826, $t = 0.22\Lambda$, and $a = 0.015\Lambda$. Figure referenced from [70]. . . . 67
4.18 Dependence of scattering parameters on polarization angle for the a) symmetric and b) reduced symmetry hexagonal SWGs at the 1.26Λ resonance. The FF and t values are the same as in Figure 4.17. Figure referenced from [70]. . . . 68

5.1 Optical beam path between an implanted mote and the detector/repeater unit. . . . 70
5.2 Illustration of example photon paths (not simulated). Figure displays the three scattering events: absorption, anisotropic defect scattering, and specular reflection at material interfaces. . . . 72
5.3 (a) Monte Carlo simulation of propagation through cerebrospinal fluid at λ = 1000 nm. The optical parameters are $n = 1.4$, $\mu_\alpha = 0.04$ cm^{-1}, $\mu_s = 1$ cm^{-1}, and $g = 0.89$. (b) Link efficiency for varying detector distance. . . . 73
5.4 Monte Carlo simulation of NIR propagation through dura mater at λ = 1000 m. The dura optical parameters are $n = 1.4$, $\mu_\alpha = 0.8$ cm^{-1}, $\mu_s = 45$ cm^{-1}, and $g = 0.75$. . . . 75
5.5 Schematic of integrated PV and CMOS chips interfaced with the Y-probe optical setup. All of the components in the Y-probe setup are fiber-coupled. Figure referenced from [179]. . . . 76
5.6 Afterpulsing after a 10 µs LED pulse for several dead time durations. (The measurements and figure are provided by Jongyup Lim). . . . 77
5.7 Photographs of the optical setup showing a) the total setup and b) a closer view of the sample/probe interface. . . . 78

6.1 Schematic cross-section of the fully assembled wireless neural mote. . . . 82
6.2 SEM cross-sectional images of a GaAs TWV a) immediately after ICP and b) after a BHF dip and O_2 treatment. c) SEM image of post-etch sidewall passivation. d) Energy-dispersive X-ray spectroscopic imaging of (c) for energies corresponding to Si transitions. . . . 84

6.3 a) Optical microscope image of the backside of a thinned GaAs sample, showing Ti/Au contact pads above parylene-infilled thin film TWVs. b) Measured I-V curves for several representative GaAs TWVs. 86
6.4 Optical microscope images of a) Pt seed layer patterning b) Cu-plated interconnects c) the backside of a thinned GaAs chip after ECD. d) SEM cross-sectional image of a plated TWV. e) Measured via resistances for several opening widths. f) Measured I-V curves. 88
6.5 Pulse timing program for pulse reverse current plating. 89
6.6 SEM cross-sections of Cu-infilled GaAs TWVs. The top row was subject to the PRC program while the bottom had only forward pulses. The slot vias are 100 µm long. . . 90
6.7 Top-down optical microscope images of GaAs TWVs plated with a a) pulse forward and b) PRC program. c) SEM micrograph of a TWV after pulse forward plating, showing Cu deposition beneath TiO_2. 91
6.8 Schematic of the fully processed CMOS chip, including blind probe via, through-wafer alignment mark, and Ni/Au solder contacts for flip-chip bonding. The dashed black circles indicate 1) the buried Al etch stop junction 2) the edge leakage path. . . . 92
6.9 a) Measured resistance of blind Si vias with varying nominal widths. b) Characteristic I-V curves for several of the structures in (a). 93
6.10 a) Optical microscope image showing the measurement setup for the isolation measurements. b) Collection of I-V curves between adjacent disconnected vias. For most of the voltage sweep, the current is below the source meter detection limit. 94
6.11 Perspective SEM images of solder bumps jetted onto Ni/Au UBM after reflow. 95
6.12 a) Photo of a 50 µm thick Si test structured mounted to a Si carrier with beeswax. The black arrow indicates the profilometric path taken in (b). b) Contact profilometry of the mounted Si piece in (a). 96
6.13 X-ray image of the bonded solder junctions after flip-chip alignment and reflow. . . . 97

7.1 Schematic of a hyperspectral imaging pixel, containing a SWG filter array integrated with a solid state detector array. 98
7.2 Schematic of flip-chip bonding using a non-conductive adhesive. 100
7.3 Mechanically diced Si test motes. a) Photograph showing ≈20% die loss. b) Optical micrograph of diced test motes. Figures courtesy of Eunseong Moon. 100
7.4 Schematic of the proposed plasma dicing scheme. 101
7.5 Optical micrographs of a) Si test motes singulated via switched reactive ion etching and b) a Si test mote tipped on its side showing sidewall profile. 102
7.6 a) A Si test mote inserted with a carbon fiber probe. b) A 3×2 array of Si test motes inserted with carbon fiber probes and mounted to an insertion rig with a putty. (Figures courtesy of Joey Letner). 102
7.7 Demonstration of end-to-end recording, beginning with an input neural signal and ending with decoded neural events. Figure is referenced from [87]. 104
7.8 a) Calculated LEE enhancement for several pseudorandom surface textures. Enhancement is relative to the unpatterned, planar structure. b) E-field radiation pattern of textured GaAs LED with "Texture 1". The texture depth is 200 nm and the dipole radiates at 1000 nm. 105

A.1 a) GaAs etch rate and $Al_{0.2}Ga_{0.8}As$ for varying RF chuck power. b) SEM cross-section for the 40 W point in (a). 109
A.2 SEM cross-sections showing dependence of sidewall quality on feature size. Figures (a-c) and (e-g) are patterned with 1D rectangular gratings with nominal periods of (a,d) 3000 nm, (b,c) 1000 nm, and (c,g) 700 nm with a 50% nominal duty cycle. (d) and (h) show isolated 500 nm lines. The RF chuck power is (a-d) 50 W and (e-h) 120 W. 109
A.3 GaAs etch rate and selectivity to $Al_{0.2}Ga_{0.8}As$ and photoresist (SPR) for varying a) RF chuck bias and b) SF_6 flow rate. The AlGaAs selectivity is unmeasurable at 30 sccm SF_6 flow. 110
A.4 Fabrication process flow for the thin film GaAs TWVs. 111
A.5 a) Photo of the tape removal process for a thinned Si wafer. b) Two thinned 3" Si wafers mounted to 4" carrier wafers after tape removal. c) Thinned sample mounting using thick SPR 220 photoresist. 112
A.6 Fabrication process flow for the selective seed layer patterning technique. 113
A.7 Fabrication process flow for the selective damascene plating technique. 114
A.8 Optical micrograph of an array of PV/LED cells for the neural motes, showing successful integration with the GaAs TWV flow in Figure A.7. (Figures from Eunseong Moon) 114
A.9 Optical micrographs and schematics showing a) the PR mask for the parylene etch b) the parylene etch c) DRIE through the parylene mask into Si d) Au contacts for electrically characterizing the vias. 116
A.10 Optical micrograph showing a) a through-wafer alignment mark within the CMOS mote circuitry and b) a blind Si probe via fabricated on the backside of a thinned CMOS chip. 117
A.11 Optical micrographs of a) Ni/Au UBM before solder bump jetting b) Ni/Au UBM after solder bump jetting and laser reflow and c) Ni UBM fabricated on the backside of a thinned GaAs wafer, aligned above GaAs TWVs. 118

LIST OF TABLES

TABLE

2.1 Specifications of the commercial SOI wafer. 25

3.1 Summary of previous work in SWG filters, highlighting the grating materials and key performance metrics. The approximate values are estimated from published figures. . 47

4.1 Character table for the D_{2h} point group at the Γ point. 51

5.1 Influence of the dura optical parameters on link efficiency at λ = 1000 nm. The layer thicknesses, optical parameters of water, and dura refractive index are all fixed. 74

6.1 Parameters for the pulse forward and pulse reverse plating programs in Figure 6.6 . . . 89

7.1 Proposed etching techniques to singulate the motes without mechanical dicing. 101

ABSTRACT

Pivotal technologies, such as optical computing, autonomous vehicles, and biomedical implantables, motivate microscale infrared (IR) components. Hyperspectral imagers (HSI), for example, require compact and narrowband filters to obtain high-spatial *and* -spectral resolution images. HSIs acquire continuous spectra at each pixel, enabling non-destructive analyses by resolving IR scattering/absorption signatures. Toward this end, dielectric subwavelength gratings (SWG) are intriguing filter candidates since they are low-loss, have no moving parts, and exhibit narrow spectral features. Wireless neural implantables are another apropos microscale IR technology. Wireless IR data and power transfer disposes of infection-prone percutaneous wires by leveraging the IR transparency window in biological tissue. This dissertation contains two related topics. The first details SWG IR filters, and the second studies progress toward wireless neural motes.

This work extends the capabilities of SWG IR filters. Following a thorough theoretical background, mid-wave infrared (MWIR, 3-7 μm) transmittance filters are experimentally demonstrated using the zero-contrast grating scheme. Via a facile silicon fabrication process, we realize narrowband polarization-dependent (Q = 175) and polarization-independent (Q = 101) MWIR transmittance filters with some of the highest Q observed in MWIR SWGs. An empirical study confirms the relationship between filter performance and grating size, an important trade-off for HSIs. We then demonstrate GaAs SWG filters for monolithic integration with active optoelectronic devices. GaAs SWGs perform comparably to their silicon counterparts, with $Q > 50$ and $> 50\%$ transmission efficiency.

To enable narrowband filtering at normal incidence, we investigate symmetry-breaking in geometrically asymmetric gratings. The presented SWG geometries access quasi-bound states in the continuum (BIC) with long mode lifetimes. Studies in Fano resonance and diffraction efficiency symmetry provide physical insight. Asymmetric 1D and 2D SWGs furnish polarization-dependent and -independent filtering, respectively. We experimentally demonstrate normal incidence long-wave IR (LWIR, 7-12 μm) transmittance filtering in asymmetric SWGs and confirm symmetry-breaking implications. Best structures exhibit 159 nm resolution with a 1.22x10^4 μm^2 filter size. A reduced-symmetry hexagonal pattern presents an early design for truly polarization-independent quasi-BIC coupling in SWGs.

Advancements in implantable neural devices promise great leaps in brain mapping and thera-

peutic intervention. To meet this challenge, we investigated a wireless neural mote system using near-infrared (NIR, 800 nm – 3 μm) photovoltaics and LEDs to wirelessly harvest power and transmit data. The neural recorders consist of three subsystems: an epitaxial GaAs-based optoelectronic chip, a Si CMOS IC, and a carbon fiber probe. Though this work encompasses the diverse efforts of many, this dissertation outlines contributions in a few critical areas. To overcome the limits of low-flux LED emission, we devise an optical setup with $\approx$0.1% photon detection efficiency. Monte Carlo techniques model NIR scattering in biological tissue. Another steep challenge is the heterogeneous integration of the three material systems in a compact (200x170x150 μm^3) package. To relay data and power between the GaAs and CMOS chips, through-wafer vias are critical. Using a novel selective copper plating technique, we demonstrate through-wafer GaAs vias with $<2\ \Omega$ series resistance. Additionally, conductive blind vias are presented for carbon fiber probe insertion. A self-aligned parylene etch mask permits sub-kΩ connection to a buried metal contact while maintaining GΩ substrate isolation. Both via structures meet the requirements of being low-resistance, insulated from the substrate, and amendable to thinned wafer processing. Finally, we demonstrate extensive processing on thinned chips and advances toward full heterogeneous integration via flip-chip alignment and solder bump bonding.

CHAPTER 1

Introduction

1.1 Microscale Infrared Technologies

Though invisible to the human eye, infrared (IR) radiation has an irreplaceable societal role. Roughly encompassing the wavelengths between 700 nm (the edge of human vision) and 15 μm (the far-IR), the IR waveband is integral to many fields. These notably include fiber optics, thermal imaging, night vision, atmospheric studies, IR astronomy, photovoltaics, and IR spectroscopy. Objects near room temperature radiate electromagnetic energy that is almost entirely IR, while at our sun's temperature (5778 K) IR accounts for over half of the radiated power. This is a crucial consideration for thermal and astronomical imaging, solar energy harvesting, and thermophotovoltaics. IR radiation excites many molecular vibrational modes, enabling non-destructive compositional analyses. Furthermore, the Earth's atmosphere exhibits low absorption within the ≈3-5 μm and ≈8-14 μm wavebands [1]. Known as IR windows, these wavebands are invaluable to atmospheric studies, remote sensing operations, and missile defense. Figure 1.1 depicts the IR spectrum, highlighting technologically important wavelengths.

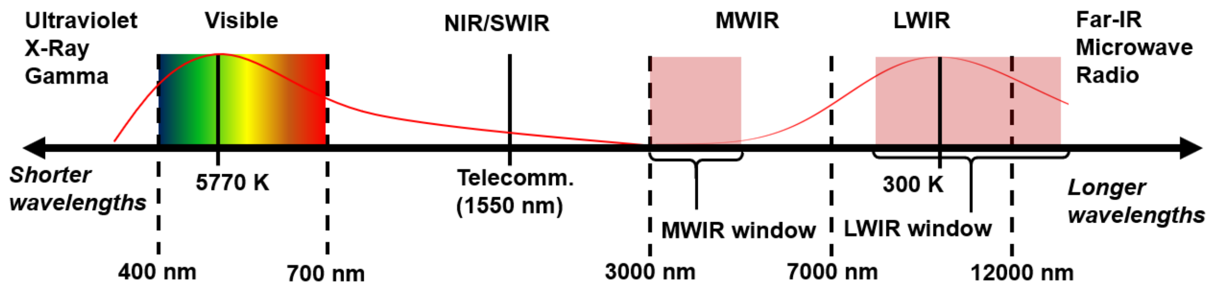

Figure 1.1: IR spectrum and important wavelengths. The two red curves are approximate black-body radiation spectra corresponding to objects at 5770 K and 300 K.

Engineers face many challenges characteristic to the IR. Given their longer wavelength, IR photons are less energetic than their visible counterparts. Consequently, a basic photodetector requires a narrow band gap semiconductor. Thermal carrier generation induces a high noise factor, making room-temperature detection challenging. Many common optical materials that are transparent in the visible regime absorb strongly in the IR. In addition to reduced device efficiencies, this restricts the engineer to a narrower materials list. As with all microscale technologies, further downscaling complicates device fabrication, integration, and operation. Though the challenge is steep, microscale IR devices promise lower power consumption, higher operational speeds, and reduced size. The devices presented in this dissertation share a common goal. They tackle topical questions by harnessing the dual prospects of IR technology and microscale device scaling. State-of-the-art microscale IR technologies, such as hyperspectral imagers, biomedical implantables, and optical computers, require a complete toolbox of optical components. This includes passive structures (lenses, mirrors, filters, etc.) and active devices (sources, detectors, modulators, etc.), as well as advanced measurement and fabrication techniques. This dissertation presents developments in subwavelength gratings (SWG) for IR spectral filtering and innovations in IR-powered neural implantables.

1.2 Dielectric Subwavelength Gratings

It is useful to examine two attributes when judging a technology: function and feasibility. The excitement of novel functionalities is tempered by practical concerns, such as cost, ease of fabrication, durability, scalability, lifetime, etc. By this metric, dielectric SWG filters are exceptional, embodying both facile construction and complex physical interaction. Figure 1.2 illustrates the simplicity of the prototypical SWG. Three layers make up the SWG structure. Layer 1 is the low-index cover (often simply air), while Layer 3 is a low-index substrate. Layer 2 contains the grating, defined by a periodic alternation between low-index and high-index materials. SWGs require no moving parts, possess subwavelength thicknesses, and are fabricated using routine microfabrication techniques. This contrasts with other IR filtering strategies, such as prisms, tunable Fabry-Pérot microcavities [2], and classical diffraction gratings. Some common dielectrics are nearly transparent at IR wavelengths, thereby avoiding the Ohmic loss endemic to metallic structures. Despite their apparent simplicity, or perhaps because of it, SWGs can service an impressive set of societal functions.

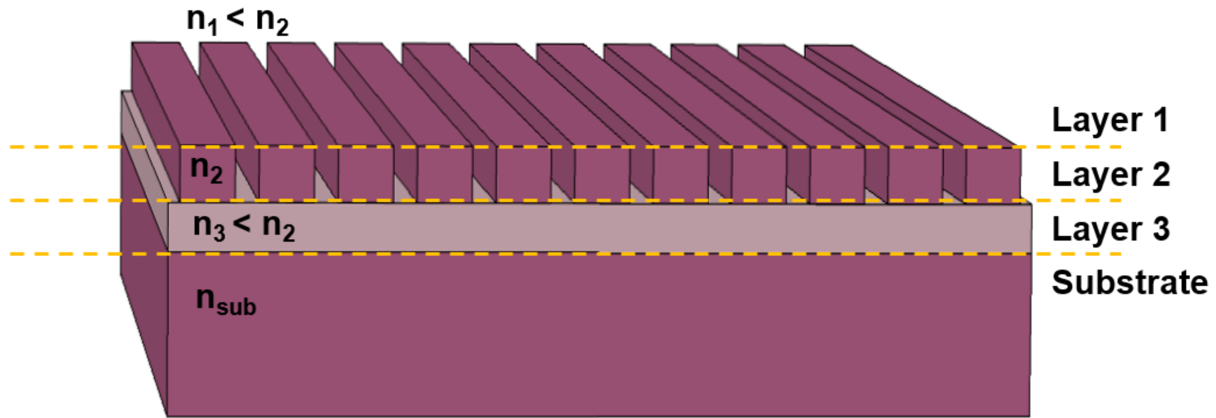

Figure 1.2: Schematic of a conventional dielectric subwavelength grating.

The field of SWGs began in earnest in 1965 when Hessel and Oliner proposed a new interpretation of the well-known Wood's anomaly in optical diffraction gratings [3]. Their seminal work highlights the key difference between classical diffraction gratings and the then mysterious SWG behavior:

"It is shown that two distinct types of anomalies may exist: a Rayleigh wavelength type due to the emergence of a new spectral order at grazing angle, and a resonance type which is related to the guided complex waves supportable by the grating."

These "guided complex waves" induce "standing waves in the grating grooves", a near field effect distinct from far field diffraction. Twenty years later, Mashev and Popov provided early experimental evidence of anomalous narrow spectral resonances in three-layer dielectric gratings [4]. In 1990, Wang et al. clarified this guided wave behavior in a numerical study, observing sharp spectral features in periodic dielectric media [5]. Although SWGs rested on a solid theoretical foundation, realization of their full potential required computational and fabrication advancements. Experimental studies flourished by the mid-1990s, with a focus on guided mode resonant (GMR) gratings like the one shown in Figure 1.3. Early resonant SWG work demonstrated several near-infrared (NIR, 800 nm – 3 µm) reflection-mode (notch) filters [6–9], though transmission-mode (bandpass) filters were equally plausible [10, 11].

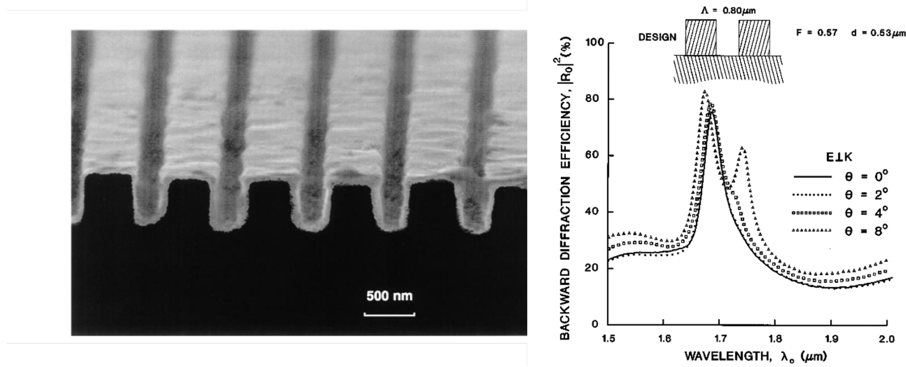

Figure 1.3: (left) SEM micrograph of cross-sectioned silicon-on-sapphire GMR grating. (right) Angular-dependent reflectance spectra. Figures are published in [9].

The advantages of resonant gratings quickly materialized, vastly outperforming homogeneous three-film dielectric stacks such as Fabry-Pérot interferometers and distributed Bragg reflectors [11]. Proposed applications for SWG filters include, but are not limited to, mirrors for tunable laser facets [11, 12], wavelength-division multiplexing [13], energy efficient "smart window" films [14], and IR hyperspectral imaging [15]. A particularly fruitful application is in vertical cavity surface emitting lasers, where a SWG mirror acts as a partially transmitting edge facet [16, 17]. Since the resonant wavelength is dependent on the local index, SWG filters are useful refractive index sensors, with applications in the biological and medical sciences [18, 19]. Numerous experimental SWG filters exhibit high-Q resonances with low sideband power in the NIR [9, 20–38]. SWG filters are, however, less proven within the mid-wave infrared (MWIR, 3-7 μm) and long-wave infrared (LWIR, 7-12 μm) regimes. [15, 39–46] These longer wavelengths contain many molecular vibrational modes (as shown in Figure 1.4 for common atmospheric gases) and a high flux of low temperature blackbody radiation.

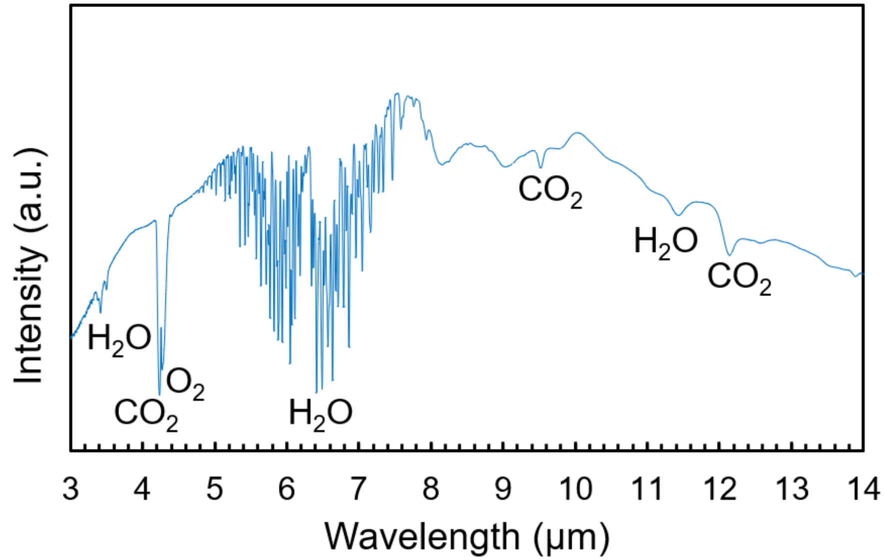

Figure 1.4: Transmittance spectrum of the Earth's atmosphere showing the resonant absorption wavelengths for common gaseous molecules.

Many other SWG applications are proposed in addition to spectral filtering. GMR-based SWGs produce wide spectral features with near-unity transmittance or reflectance, enabling thin, broadband mirrors [47, 48] and anti-reflection coatings respectively [49]. Strong polarization-dependence makes SWGs useful for polarizing applications [50]. Due to local electromagnetic field enhancement, resonant SWGs are intriguing surfaces for perfect absorbers and photovoltaics [51, 52]. Recently, SWG filters are proposed as high-pass filters for boosting thermophotovoltaic efficiency [53]. Many other applications for periodic subwavelength dielectric structures have been demonstrated, many of which do not use the GMR principle. These include deeply subwavelength metasurfaces, flat lenses, SWG waveguides, and sensors based on local Mie resonances. This review of SWGs is not comprehensive and the interested reader is directed to References [12, 54]. Though this dissertation focuses on bandpass filters, the reported advancements benefit many SWG applications.

Hyperspectral imaging (HSI) is a particularly alluring application for IR SWGs and is a major motivation for the work presented in this dissertation. HSIs represent the most ambitious digital imaging system, aiming for high-spatial *and* -spectral resolutions. This contrasts with RGB cameras, for example, which have high pixel density but only detect three wavebands, or a spectrometer which possesses extremely high-spectral resolution but gathers limited spatial information. The applicability of IR HSI is virtually limitless. Accessing each pixel's full spectrum unlocks profound compositional insight, as most objects scatter, absorb, reflect, or emit IR radiation with strong wavelength dependence. For decades these systems saw use in remote sensing operations,

including astronomy [55], atmospheric studies [56, 57], and resource management [58, 59]. More recently, IR HSIs are turned toward rapid, non-destructive analyses of nearby objects. Examples include art conservation [60], food quality monitoring [61, 62], crime scene forensics [63], mineralogy [64], and medical diagnostics [65–67]. This list is not exhaustive, as HSIs are well-equipped for creative problem solving. However, for HSIs to meet our many needs, compact and narrowband IR filters are indispensable. As shown in Figure 1.5, a HSI is only as powerful as its filters since the filter size and linewidth limit the achievable spatial and spectral resolutions, respectively.

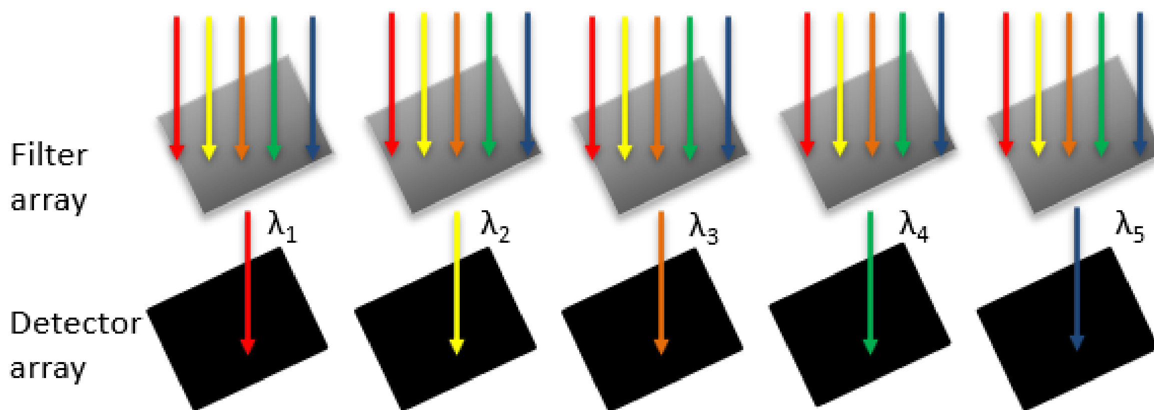

Figure 1.5: Schematic of a hyperspectral imaging pixel.

With no unified roadmap for SWG filter development, one may consider the requirements of a HSI pixel. These include high-Q resonance, small footprint, bandpass response, normal incidence operation, and polarization-independence. The studies in this dissertation each address at least one of these considerations. Refinement of experimental methods boosts quality factors in the MWIR and LWIR [43, 68]. Another study characterizes the effects of grating size on filter performance [69]. To obtain narrowband filtering at normal incidence, geometrically asymmetric SWGs access symmetry-protected modes [15, 43]. Gratings with $\leq \pi/2$ rotational symmetry, such as a square or hexagonal lattice, furnish polarization-independent optical response by coupling to leaky [68] and symmetry-protected [70] modes. Another experiment realizes SWG IR transmittance filters on the GaAs material platform.

1.3 Wireless Neural Motes

Advancements in neural interfaces portend great leaps in our understanding of neurological processes [71–73] and unveil new possibilities for therapeutic intervention [74–76]. Brain machine interfaces can establish motor prediction, potentially recovering motor control in paralyzed indi-

viduals [77]. These prospects motivate innovative neural recorder technologies. IR power and data transfer poses a solution to many of the roadblocks impeding microscale neural implantables. Traditional wired probe assemblies cause bleeding and infection, are prone to corrosion, and limit the subject's mobility. Wireless power transfer and communication circumvents these issues. Existing neural recorders use wireless telemetry via near field RF [78,79] or ultrasonic power transfer [80], though these techniques suffer from dangerously high exposure requirements and bulky dimensions, respectively. Moreover, it is imperative to preserve the dura mater during chronic implantation. This motivates subdural devices, and subsequently, NIR transmission through the dura. Conveniently, most biological tissues are highly transparent to NIR radiation [81]. Cortese et al. demonstrated a 100 μm-scale wireless sensor containing a NIR data uplink and powered by a visible laser source [82]. This design has, however, limited functionality and requires illumination that far exceeds standards for safe tissue heating over cm-scale areas. Developing a safe, wireless, high-channel count, sub-mm neural interface remains an extraordinary task with the potential to profoundly improve the quality of life for those with neurological injuries and conditions. Figure 1.6 depicts the dramatic downscaling of recent neural interfaces, though there is still considerable work to be done. Reference [83] provides an excellent review of the overall problem.

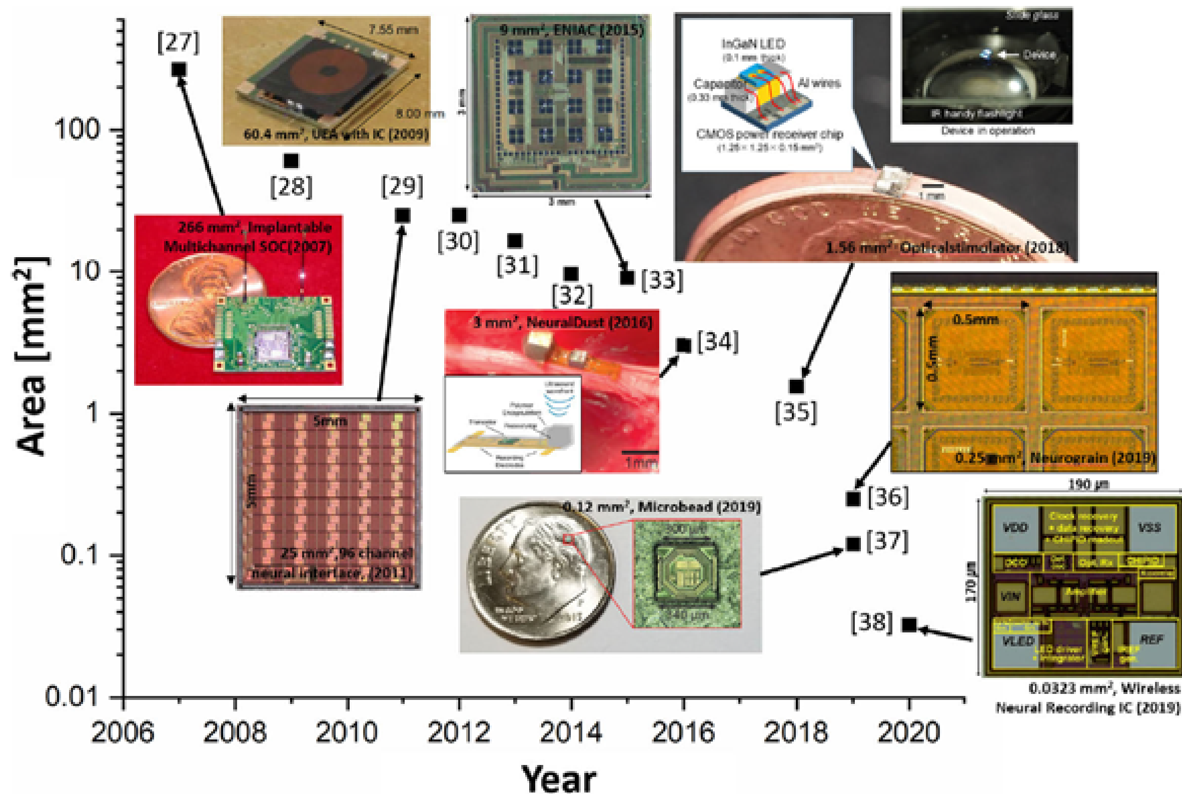

Figure 1.6: Progress in neural interface scaling. The smallest device (labeled [38] in the figure) was published by Lim et al. at the University of Michigan [84]. Figure is adopted from [83]. Reference labels apply to original publication.

To meet the the challenge, a joint team at the University of Michigan and ETH Zurich proposed a novel wireless neural dust system containing a NIR photovoltaic (PV) cell and a NIR light emitting diode (LED) [84]. A narrowband radiation source (centered at ≈850 nm) illuminates a GaAs/AlGaAs PV cell [85,86], wirelessly powering the entire assembly. Neural activity coupled to a carbon fiber probe is processed on-chip and transmitted to an external detector. A µLED furnishes data uplink via a 1000 nm emission wavelength. A subcranial repeater unit receives the emitted LED signals using a single-photon avalanche diode, simultaneously servicing 100s of probes differentiated by on-chip ID and location. Due to its larger size, the repeater uses an inductive link for wireless power transfer and data communication. As depicted in Figure 1.7, the proposed system contains several essential features: simultaneous neural recording of upwards of 1000 motes over a cm^2-scale area, on-chip computing and power functionalities, fully untethered operation, and sub-mm dimensions (≈200x170x150 μm^3). The project is multifaceted, demanding innovations in circuit design (stringent area and power limitations), NIR optoelectronics (demands for small size and high efficiency), and biomedical engineering (challenges in implantation, biocompatibility,

and device lifetime).

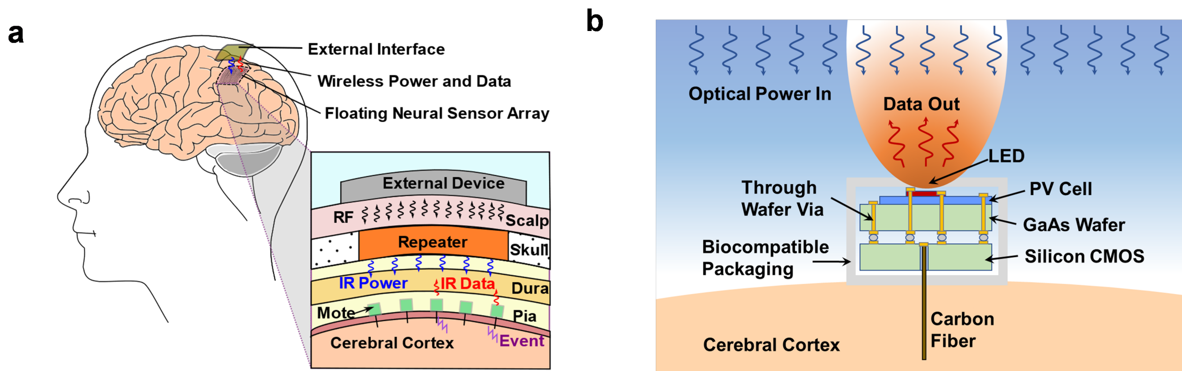

Figure 1.7: Schematic of the wireless neural dust system showing subdural implanted motes, NIR power and data uplink, and subcranial repeater unit. b) Schematic of an implanted wireless neural dust mote. Figure is referenced from [87].

The second half of this dissertation describes contributions to the work presented in [84] and [87], exploring solutions to the unique optical and microfabrication questions it presents. First, an efficient optical setup is crucial for detecting pulses from low-flux implanted LEDs. Data uplink efficiency calculations account for emission and propagation through dura tissue using a turbid material scattering model and Monte Carlo statistics. A dual-wavelength optical setup (PV illumination and LED emission) is optimized for maximal detection sensitivity. As suggested by Figure 1.7b, mote assembly is no trivial task. For the NIR-powered sub-mm implantable sensor described in Reference [82], the circuitry and PV share a single die. This simplifies construction, but intensifies trade-offs between size, functionality, and required illumination intensity. By using fully 3D integration, the system in Figure 1.7 is superior in all of these aspects at the expense of fabrication complexity. Many microfabrication innovations are demanded, including dry etch development, conductive through-wafer GaAs vias, blind silicon vias for carbon fiber probe insertion, thinned wafer processing, and heterogeneous integration of GaAs-based optoelectronics and a silicon CMOS IC.

1.4 Thesis Organization

This dissertation is organized as follows. Chapter II describes IR spectral filtering via geometrically symmetric silicon SWGs. Fundamental concepts of resonant gratings are introduced, followed by experimental studies in dielectric zero-contrast gratings. Chapter III extends the concepts in Chapter II to the GaAs material system, enabling direct integration of SWG filters with active IR devices. Chapter IV explores coupling to symmetry-protected modes using geometrically asym-

metric SWGs. Theoretical analyses elucidate the bases of symmetry-protection and -breaking in SWGs. Analytical Fano resonance theory and experimental studies further support understanding. Chapter V describes modeling of NIR emission and propagation through biological tissue. Efforts to optically characterize wireless neural motes are introduced. Chapter VI outlines the development of fabrication techniques for wireless neural motes, highlighted by the demonstration of through-wafer GaAs vias and GaAs/Si heterogeneous integration. Lastly, Chapter VII proposes additional questions to continue the efforts in Chapters II-VI.

The work in Chapters II-IV and Chapters V, VI represent largely separate projects, though both topics fall within the purview of microscale IR optical devices. One intriguing application relates these topics by using resonant SWGs to boost light extraction efficiency in embedded NIR LEDs. Additionally, several of the microfabrication developments presented in this report are germane to both SWGs and neural mote assembly. The chief example is a reactive ion etch process possessing high selectivity between GaAs and an AlGaAs etch stop while maintaining high quality surface and sidewall profiles. Such a process is relevant to both SWGs and neural motes as both structures require high aspect ratio GaAs structures.

CHAPTER 2

Symmetric Subwavelength Grating Transmittance Filters

2.1 Fundamental Principles

2.1.1 The Resonant Subwavelength Region

Subwavelength gratings (SWG) facilitate narrowband spectral filtering through the phenomenon of guided mode resonance (GMR). In GMR, SWGs hold the dual role of waveguide and coupling element [88]. Figure 2.1 provides an illustration of GMR, wherein incident light couples into quasi-guided (finite lifetime) modes supported by the grating layer, with close analogy to the discrete modes allowed in a slab waveguide. Unlike slab waveguides, which cannot in-couple light from the low-index cladding, SWG periodicity provides the additional momentum to allow free space coupling. By reciprocity, guided modes coupled through GMR re-radiate and interfere with non-resonantly scattered light, lending GMR gratings their unique spectral signatures.

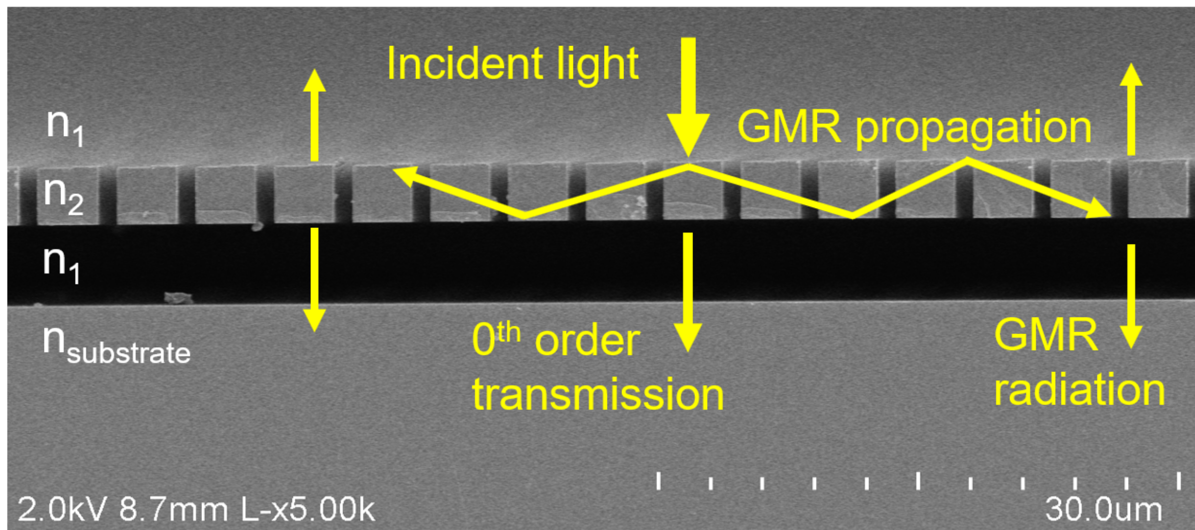

Figure 2.1: Schematic of guided mode resonance, the coupling of incident light into quasi-guided modes. The background image is an SEM cross-section of a SWG filter.

To better understand GMR, it is instructive to clarify what constitutes the subwavelength regime. Two conditions bound this waveband. The first stipulates purely zeroth order diffraction, with complete suppression of all higher orders in the far field. This condition enables efficient spectral features (i.e. near-unity poles and near-zero zeroes) since incident power is solely diffracted through one order [89]. In contrast, achieving total interference with multiple diffraction orders is challenging. For transmission through a classical 1D diffraction grating at normal incidence, the grating equation is given by

$$m\lambda = \Lambda n_{sub} sin(\theta_m) \tag{2.1}$$

where λ is the incident wavelength, Λ is the grating period, n_{sub} is the substrate refractive index, and θ_m is the diffraction angle through diffraction order m. If the substrate is vacuum, the condition for purely zeroth order diffraction reduces to

$$\lambda > \Lambda sin(\theta_m) \tag{2.2}$$

Thus, as their name suggests, SWGs require $\lambda > \Lambda$.

The second condition defines the upper wavelength limit. The subwavelength regime characteristically resists homogeneous effective medium approximation (EMA) [90], as many SWG properties result from Bragg-like reflections (e.g., optical band gaps, sharp spectral features, etc.). Figure 2.2 illustrates the inadequacy of the homogeneous slab approximation. The figure shows simulated transmittance spectra for a SWG and a homogeneous slab waveguide with refractive

index defined by zeroth-order EMA. For transverse-magnetic (TM) polarization (electric field perpendicular to the grating bars), zeroth-order EMA gives

$$n_{eff} = \sqrt{n_{vacuum}^2(1 - FF) + n_{high}^2 FF} \tag{2.3}$$

where *FF* is the grating fill factor [91]. As Figure 2.2 clearly shows, the homogeneous slab approximation fails to capture essential SWG physics. This discrepancy is only partially attributable to numerical error, as higher order approximations better estimate the effective indices of SWG modes [90]. Regardless of the n_{eff} calculation accuracy, treating the SWG as a homogeneous layer misses key features induced by the grating periodicity. In particular, the SWG's narrow spectral features are totally absent in the slab transmittance spectrum. These narrow resonances peculiar to SWGs are GMR signatures [88].

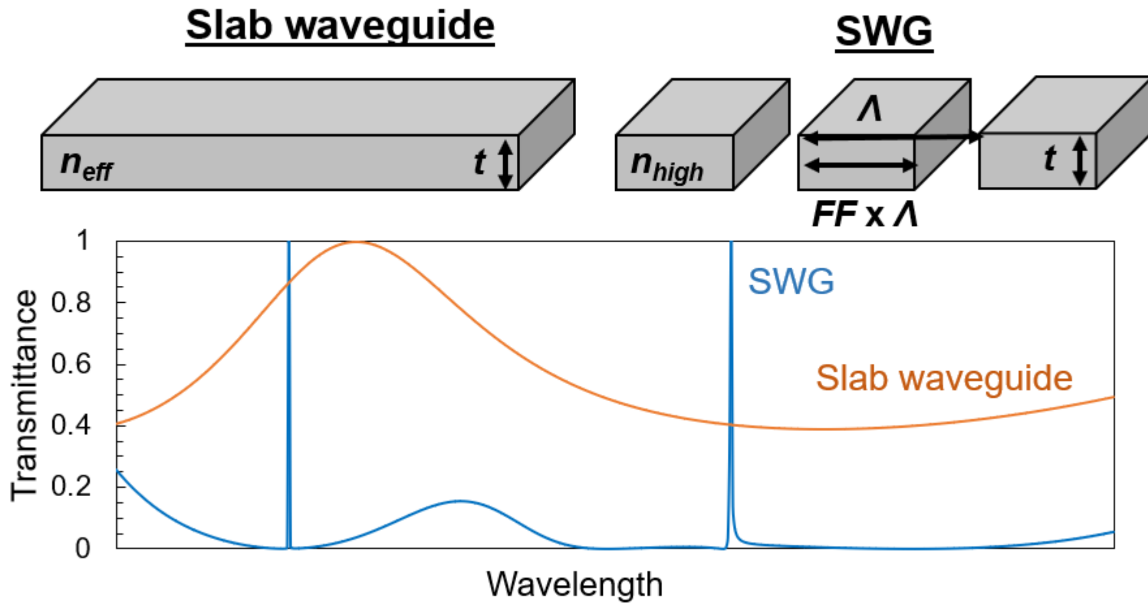

Figure 2.2: Simulated transmittance spectra of a slab waveguide and a SWG. The effective index of the slab waveguide is given by Equation 2.3. The thickness, *t*, is the same in each case.

It is thus necessary to distinguish the ”resonant subwavelength” and ”deep subwavelength” regions [92]. Deep subwavelength structures ($\Lambda/\lambda \rightarrow 0$) are well-approximated by zeroth-order EMA [90, 91]. Though SWGs suppress non-zero diffraction orders in the far field, the grating periodicity supports GMR via near-field evanescent coupling through higher orders. A SWG can only support GMR if it admits at least the first evanescent diffraction order [92]. Recently, this condition was leveraged in Equation 2.4 to analytically distinguish the (guided mode) resonant subwavelength region from the deep subwavelength region.

$$\lambda_c^1 = 2\Lambda FFn_{high} \tag{2.4}$$

In Equation 2.4, λ_c^1 is the cut-off wavelength for the first evanescent diffraction order, while the other parameters are defined in Figure 2.2. Finally, this defines the conditions necessary for GMR filters: $\Lambda < \lambda < 2\,\Lambda FFn_{high}$.

2.1.2 Homogeneous Slab Analysis

While a naive homogeneous slab approximation does not account for GMR, the slab waveguide analogy is still quite useful. In fact, GMR structures are sometimes referred to as "waveguide gratings" [93]. Figure 2.3a shows the basic scheme of a slab waveguide. A dielectric slab sandwiched between two lower index layers guides laterally propagating modes via total internal reflection at the n_1/n_2 interfaces. To avoid destructive interference, the z-component of the wavevector must be a discrete multiple of π/d, noting that the fundamental mode ($k_z = 0$) is always an eigensolution. Guided modes possess either symmetry or anti-symmetry with respect to the xy-plane. Satisfying electromagnetic boundary conditions at the n_1/n_2 interfaces allows derivation of the transcendental dispersion relations in Equations 2.5 and 2.6, where ω is the frequency and μ_0 is the magnetic permeability of free space. Equation 2.5 refers to transverse-electric (TE) eigensolutions and Equation 2.6 to transverse-magnetic (TM).

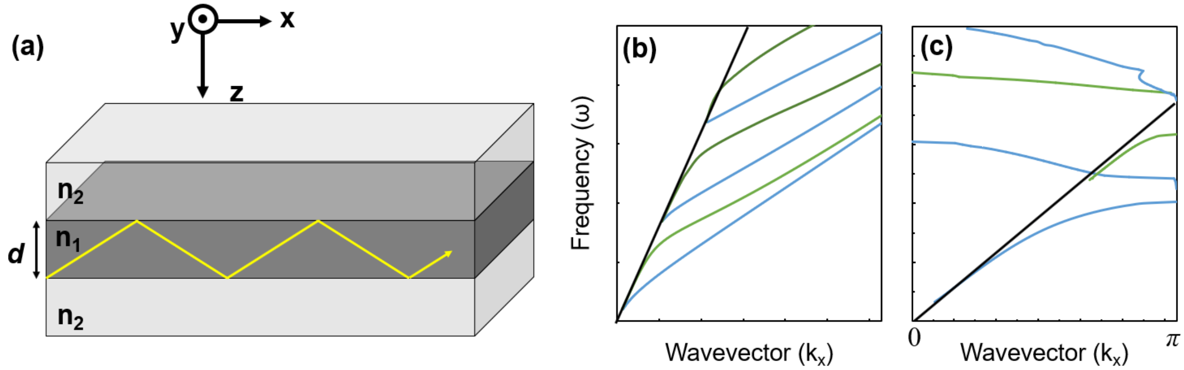

Figure 2.3: a) Schematic of a slab waveguide. (b,c) Dispersion relations of b) a slab waveguide and c) a SWG. Blue(green) curves correspond to TE(TM) modes. The black line is the light line.

$$\left\{ \begin{array}{c} tan(k_z d) \\ -cot(k_z d) \end{array} \right\} = \sqrt{\frac{\omega^2 \mu_0 (n_1^2 - n_2^2)}{k_z^2} - 1} \tag{2.5}$$

$$\left\{ \begin{array}{c} tan(k_z d) \\ -cot(k_z d) \end{array} \right\} = \frac{n_1^2}{n_2^2}\sqrt{\frac{\omega^2\mu_0(n_1^2-n_2^2)}{k_z^2} - 1} \tag{2.6}$$

The dispersion relation in Figure 2.3b shows the discrete guided modes calculated with Equations 2.5 and 2.6. The black line corresponds to the dispersion relation of a plane wave in free space, also known as the light line, and is given by $\omega = ck$, where *c* is the speed of light. Since every mode in the slab waveguide lies beneath the light line, no light may couple in from the lower-index layers.

Extending these concepts to resonant SWGs, Reference [88] considers the same three-layer structure in Figure 2.3a, but allows $n_1(x)$ to become a function of position:

$$n_1(x) = \sqrt{n_g^2 + \Delta n^2 cos(Kx)} \tag{2.7}$$

where n_g is average refractive index, Δn^2 is the modulation amplitude, and $K = 2\pi/\Lambda$. Similarly to the homogeneous waveguide, GMR is supported if the effective index of the guided mode, n_{eff}, allows total internal reflection at the cover and substrate interfaces. That is, $n_2 \leq n_{eff} < n_g$. Letting $\Delta n^2 \to 0$ gives an expression for the effective propagation constant for mode *i*:

$$\beta_i = k(n_g^2 sin\theta - i\lambda/\Lambda) \tag{2.8}$$

where θ is the angle of incidence. The SWG eigenvalue equations take on a form reminiscent of Equations 2.5 and 2.6. For TE polarized light

$$tan(\kappa_i d) = \frac{\kappa_i(\gamma_i+\delta_i)}{\kappa_i^2-\gamma_i\delta_i} \tag{2.9}$$

where $\kappa_i = (n_g^2 k^2 - \beta_i^2)^{1/2}$, $\gamma_i = (\beta_i^2 - n_1^2 k^2)^{1/2}$ and $\delta_i = (\beta_i^2 - n_3^2 k^2)^{1/2}$. This analysis, which stems from homogeneous waveguide physics, provides useful insight into SWGs. With minimal computational expense, one can closely estimate a GMR's effective index and spectral location using Equations 2.8 and 2.9, respectively.

2.1.3 Guided Mode Resonant Gratings

Several features distinguish the slab waveguide from the GMR filter. Foremost, as shown in Figure 2.2, SWG spectra possess sharp GMR features. Bloch's Theorem expresses the modes in a periodic structure by introducing a function $u_{mk}(\boldsymbol{r})$ with periodicity equal to Λ:

$$E_m(\boldsymbol{r}, k_z) = exp(-jk_x x)u_{mk}(\boldsymbol{r})) \tag{2.10}$$

In Equation 2.10, $E_m(\boldsymbol{r}, k_z)$ is the resonant field profile for the m$^{\text{th}}$ modal order and $\boldsymbol{r}$ is the position vector. As shown in Figure 2.3c, the grating vector $K = 2\pi/\Lambda$ folds the reduced Brillouin zone at $k_x = K/2$, bringing resonant modes into the continuum of radiative states above the light line [94]. Incident plane waves (with $k_x = \boldsymbol{k_{inc}} sin(\theta_{inc})$) cannot phase match with the guided modes in an unmodulated waveguide. In SWGs, the grating vector, *K*, endows incident light with the lateral momentum needed to match GMR phase ($k_x = \boldsymbol{k_{inc}} sin(\theta_{inc}) + mK$, where *m* is an integer). Accordingly, the SWG can couple light incident from any angle.

The grating modulation also opens the optical bandgaps observed in Figure 2.3c. Electromagnetic modes concentrated in a high-index material have lower energy than modes in lower-index media [94, 95]. Via the variational principle familiar in quantum mechanics, for both bands to be real eigensolutions of the SWG implies modal orthogonality [94]. Chapter IV gives a thorough treatment of the properties and consequences of modal symmetry.

It is worth noting that EMA can model GMR with an alternate interpretation of the EMA effective index [92]. In standard EMA analysis, the exact formulation for the TE polarization is

$$\sqrt{n_2^2 - (n^E)^2} tan(\tfrac{\pi\Lambda}{\lambda}(1-FF)\sqrt{n_2^2 - (n^E)^2}) = \sqrt{n_1^2 - (n^E)^2} tan(\tfrac{\pi\Lambda}{\lambda} FF \sqrt{n_1^2 - (n^E)^2}) \quad (2.11)$$

Solving Equation 2.11 for n^E gives the effective medium index. The function $tan(x)$ has infinitely many roots, though EMA studies typically discard all but the lowest order. Consequently, the zeroth-order approximation treats the modulated layer as a homogeneous slab with only one refractive index value per wavelength. However, allowing the refractive index to have multiple values per wavelength accounts for evanescent coupling through higher diffraction orders. These additional n^E indices are the higher order roots of the $tan(x)$ functions in Equation 2.11. The cut-off wavelengths for each n_m^E index is given by Equation 2.4, corresponding to the wavelengths supporting GMR through evanescent diffraction order $|m| > 0$. This reinterpretation of EMA yields excellent agreement with known GMR spectra [92], affirming the essential nature of evanescent coupling in GMR gratings.

2.2 Characteristics of Guided Mode Resonances in SWGs

2.2.1 Symmetry-Protected Modes

As alluded in the previous section, understanding filter performance requires knowledge of the symmetries of the GMR field profiles. Symmetry influences many aspects of the filters, including mode selection rules, resonance lifetime, and angular tolerance. Under certain high-symmetry

conditions, a GMR may possess infinite lifetime and be prohibited from external coupling. In the broader physics community, these prohibited states are known as bound states in the continuum (BIC), manifested as discrete bound resonances within the continuum of radiative states [96–98]. Chapter IV provides in-depth analysis of BICs in SWG filters, though for Chapters II and III explanation of a few basic concepts is in order.

Figure 2.4 illustrates one configuration containing a BIC. Consider a planewave impinging on a 1D rectangular HCG at an angle θ. Since the field profiles of GMRs must have the same symmetries as the grating itself [94], each mode is either symmetric (even) or anti-symmetric (odd) across the *yz*-plane. At normal incidence, the planewave possesses even symmetry, preventing coupling to modes with odd field profiles, such as the one depicted in Figure 2.4. Since the overlap between even and odd functions integrates to zero, this mode is a symmetry-protected BIC.

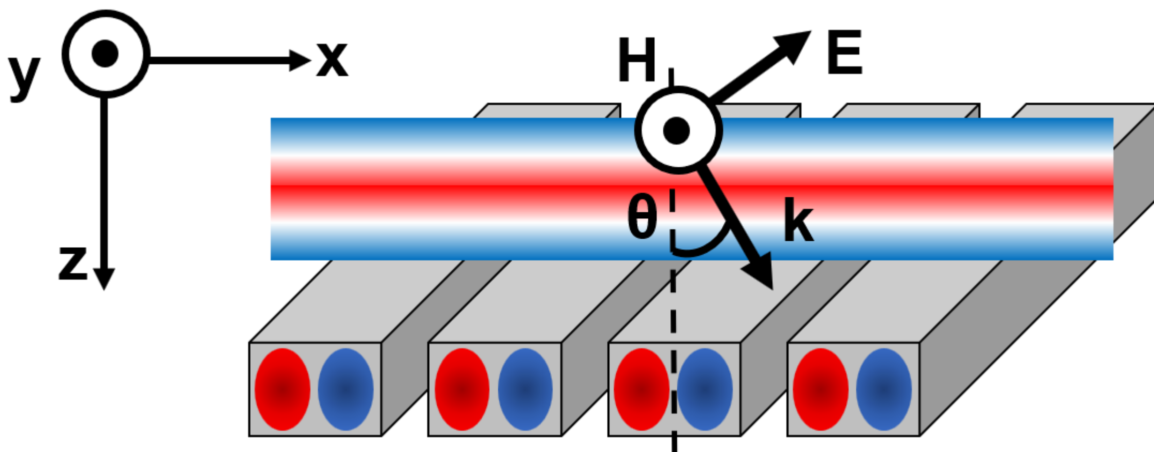

Figure 2.4: Illustration of symmetry mismatch between a normally incident plane wave and a resonant mode with odd field symmetry. Mirror symmetries are referenced to the *yz*-plane, as depicted by the dashed black line. The angle θ is the polar angle of incidence.

Access to symmetry-protected modes is as simple as breaking one of the symmetries by either introducing oblique incidence ($\theta > 0°$) or employing an asymmetric grating geometry [43,99,100]. Figure 2.5a shows simulated transmittance spectra for a symmetric rectangular grating for several angles of incidence. As expected, at normal incidence there is no transmission peak since the targeted mode is symmetry-protected. For the oblique angles of incidence, a sharp transmittance peak appears since the even-symmetry of the planewave is broken. This principle is the basis for the high-Q filters in Chapter II and III, while geometrically asymmetric filters are explored in Chapter IV.

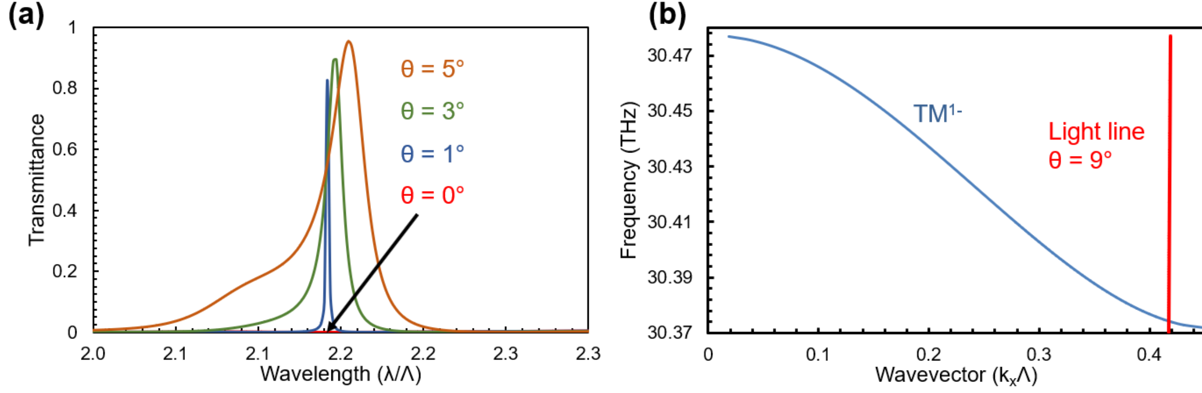

Figure 2.5: a) Simulated transmittance spectra of a rectangular SWG for varying angle of incidence. b) SWG dispersion near zone center (Γ-point). The red line is the light line at $\theta = 9°$.

2.2.2 Resonance Linewidth

In Figure 2.5a the resonance linewidth increases with θ. As the incident light becomes more oblique, the degree of symmetry-breaking increases. The greater field overlap increases the radiative decay rate, γ_{rad}, decreasing the resonance lifetime via $\tau = \gamma_{rad}{}^{-1}$ and broadening the linewidth. Throughout this dissertation, the quality factor (Q) is defined by the ratio between a resonance's central wavelength and its full width at half maximum linewidth. In a general two-port system, temporal coupled mode theory reveals a simple relation between Q and an asymmetry parameter δ [101]. Equation 2.12 gives an expression for small δ.

$$Q \propto \delta^{-2} \tag{2.12}$$

This relationship is reflected in Figure 2.5a. In addition to radiative decay, Q is dependent on energy loss through non-radiative absorption and scattering, giving the relation: $1/Q = 1/Q_{radiative} + 1/Q_{non-radiative}$.

2.2.3 Angular Tolerance

Obliquely incident light reduces Q and redshifts the resonant wavelength. This latter effect stems from the dispersive nature of SWGs. Figure 2.5b shows a close view of a SWG dispersion relation near zone center. As signified by its negative dispersion, the band labeled TM^{1-} is a lower band and is symmetry-protected at $\theta = 0°$ by virtue of its odd field symmetry. Though obliquely incident light may couple to this mode, the coupling condition shifts according to the dispersion relation. In Figure 2.5b the red line depicts the light line for a plane wave incident at $9°$. For this particular HCG geometry, this corresponds to a redshift of $\approx 0.007\Lambda$.

Angular tolerance is of practical importance for narrowband filters. High numerical aperture imaging systems (permitting a wide range of incident angles) cause significant peak broadening due to dispersion. Furthermore, angular tolerance places a scaling limit on finite SWG filters, as angular divergence is inversely proportional to beam spot size. For a Gaussian beam with full waist w_0, angular divergence θ_{div} is given by

$$\theta_{div} = \tfrac{4\lambda}{\pi w_0} \tag{2.13}$$

Thus, as the beam size decreases, so does Q. This is a limiting factor for optical systems like hyperspectral imagers, since increasing pixel density comes at the expense of spectral resolution [102]. Several works improve angular tolerance by flattening the dispersion curves [31, 103, 104].

2.3 Subwavelength Grating Geometries

This section describes the important subclasses of GMR SWGs. To prevent confusion, it is necessary to disentangle the definitions of "high-contrast grating" used in SWG nomenclature. In some instances, the eponymous index contrast refers to the grating modulation strength ($\Delta n = n_1 - n_2(n_3)$ in Figure 2.6(a,b)). As shown in Figure 2.6(a,b), this corresponds to the index contrast between the high index grating bars and the gaps between them. In a high-contrast grating, n_2 is small (typically air), while in low-contrast gratings the gap infill has an index n_3 that is closer to n_1. To study the influence of Δn, the relative permittivity in a SWG may be expanded into a Fourier series as in Equation 2.14, where ϵ_q is the Fourier coefficient for the qth harmonic and $K = 2\pi/\Lambda$ [105].

$$\epsilon(x) = \sum_{q=-\infty}^{\infty} \epsilon_q exp(jqKx) \tag{2.14}$$

Tuning the Δn-dependent harmonics of the grating permittivity has large consequences for the bandwidth and location of spectral features [104–106]. While interesting, this work is not the focus of this dissertation.

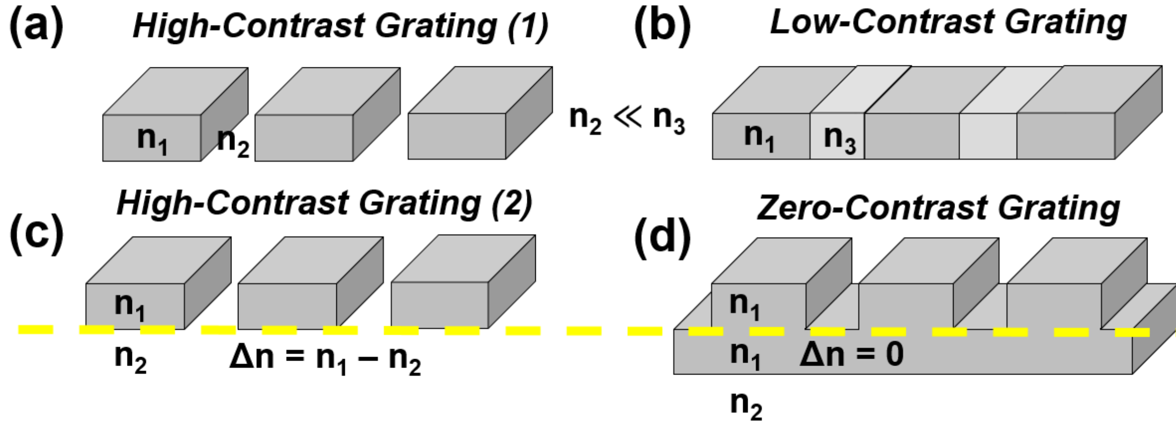

Figure 2.6: a,c) The two "high-contrast grating" definitions. b) A "low-contrast grating". d) A "zero-contrast grating". The dashed yellow line signifies the interface referred to by the high-/zero- contrast distinction.

Instead, the following studies emphasize the grating classes depicted in Figure 2.6(c,d). In this case "index contrast" refers to the contrast between the high index grating bars and the homogeneous layer directly beneath them. In high-contrast gratings (HCG) $\Delta n = n_1 - n_2$, while in zero-contrast gratings (ZCG) $\Delta n = 0$. ZCGs rest above a homogeneous slab of the same refractive index, though not necessarily the same material. In all HCGs and ZCGs described in this work, $n_{eff} > 2n_2$, where n_{eff} is the effective index of the targeted resonance [105]. This condition guarantees that the GMR condition is met. For the remainder of this report, HCG refers to this second definition.

Though there are a few interesting differences, HCG and ZCG filters operate on the same fundamental GMR principle. Neither structure has a clear advantage in performance, though there is evidence that ZCGs may achieve somewhat broader resonances than comparable HCGs [107]. HCGs have the practical advantage of permitting liquid between the grating lines [40, 43]. This allows simple wet etching of an underlying layer, enabling a very large index contrast for gratings suspended in air. ZCGs can suffer from substrates with unfavorable optical properties. On the other hand, ZCGs offer greater design flexibility. Introducing the homogeneous (slab) layer allows greater control of the permittivity Fourier harmonics, enabling filters with greater angular tolerance [104]. By judiciously designing the gratings and slab, TE and TM modes are independently tunable [44]. Lastly, the slab layer supports structures that are physically impossible in suspended HCGs, such as the 2D pillar arrays presented in Reference [68].

2.4 Experimental Methods

The techniques described in this section apply to the SWG studies in Chapters II-IV. These methods are generalized; the specific studies provide additional detail where necessary.

2.4.1 Numerical Modeling

The structures in this dissertation are simulated using two numerical models. Due to its computational efficiency, rigorous coupled-wave analysis (RCWA) calculates SWG transmittance spectra. For problems requiring full wave analysis, such as dispersion relations, field profiles, and SWGs with finite periodicity, finite element methods (FEM) are used.

2.4.1.1 Rigorous Coupled Wave Analysis

RCWA decomposes the dielectric function of each layer in a periodic structure into a set of Fourier harmonics. The boundary conditions between the layers are satisfied for each harmonic using the coupled-wave equation

$$\frac{d^2\hat{S}_i(z)}{dz^2} + k^2\epsilon_g - k^2(\sqrt{\epsilon_g}sin\theta - i\lambda/\Lambda)^2\hat{S}_i(z) + 0.5k^2\Delta\epsilon[\hat{S}_{i+1}(z) + \hat{S}_{i-1}(z)] = 0 \tag{2.15}$$

where $\hat{S}_i(z)$ is the amplitude of the ith harmonic, ϵ_g is the average grating permittivity, $\Delta\epsilon$ is the grating modulation strength, and $k = 2\pi/\lambda$ [108]. Solving the set of coupled equations yields a wavelength-dependent scattering (S)-matrix, from which reflection and transmission spectra are extracted. Since RCWA is not a full wave solver it is computationally efficient, yet has limited functionality as it does not calculate field profiles nor can it simulate non-periodic structures. The SWG transmittance spectra in this dissertation are calculated using an open-source RCWA package (S^4, [109]). A control file accepts the number of layers, the dielectric function and thickness of each layer, the direction and polarization of an incident planewave, and the number of harmonics to compute.

2.4.1.2 Finite Element Methods

Full wave FEM calculations are performed using the COMSOL Multiphysics, Wave Optics package. To model periodic gratings, the computational domain is truncated to a single unit cell. Floquet boundary conditions simulate infinite periodicity, as shown in Figure 2.7. In the case of gratings periodic in multiple dimensions, the model defines two (square lattice) or three (hexagonal lattice) periodic boundary pairs. A port boundary condition at the top of the unit cell defines

the angle of incidence and polarization state of the excited fields. This model calculates S-matrices and electromagnetic field profiles.

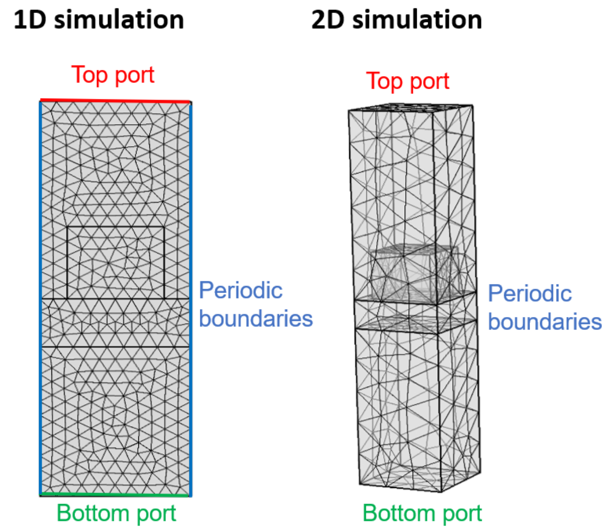

Figure 2.7: Meshed FEM models of 1D and 2D SWG unit cells with labels for the excitation (top) port, listener (bottom) port, and periodic boundary conditions.

2.4.1.3 Genetic Algorithm Optimization

An in-house genetic algorithm (GA) aids SWG design, enabling efficient optimization without sweeping the entire solution space. The ZCG, for example, has four geometric parameters to optimize (Λ, FF, $t_{grating}$ and t_{slab}). A full sweep over the four parameters is impractical on a personal computer. Fortunately, numerical methods such as particle swarm optimization [110] and genetic algorithms [111] can efficiently find a global solution. Figure 2.8a shows the evolution of a HCG bandpass filter designed by the GA. The initial solution is extremely unfit but converges to a high-quality narrowband filter within 80 iterations.

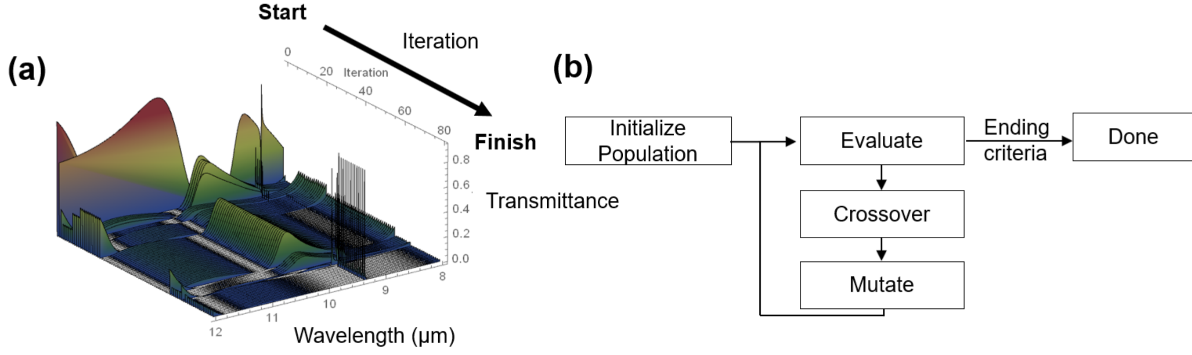

Figure 2.8: SWG geometry optimization via a genetic algorithm. a) Solution convergence as a function of iteration number. b) High-level flow chart of the genetic algorithm.

Figure 2.8b shows a high-level flow chart of the GA. It begins by randomly generating a population of solutions, each consisting of the set of parameters to be optimized (or chromosomes in the biological analogy). The population size is typically 20-30. The initial population is evaluated by computing the transmittance spectrum of each individual using RCWA. The spectra are processed to extract fitness, *f*, given by the function

$$f = \Delta\lambda_{ref} * |\lambda_0 - \lambda_{tar}| \tag{2.16}$$

where Δ_{ref} is the width of the high-reflectivity (T $<$ 5%) window, λ_0 is the central wavelength of the transmittance peak, and λ_{tar} is the target peak wavelength. The fitness function does not consider peak transmittance or linewidth since these parameters are more strongly dependent on other factors, such as geometric asymmetry and angle of incidence. After determining each individual's fitness, the population generates the next generation through the genetic operations of crossover and mutation. In crossover, individuals are randomly chosen to breed the next generation, with fitter functions more likely to be chosen. The selected parent members split their chromosomes to create solution children for the next generation. To ensure genetic diversity, some of the chromosomes undergo random mutation. In the GA employed by the following studies, mutated values are chosen from the Gaussian distribution

$$p_{new}(x) = \frac{1}{\sigma\sqrt{2\pi}} exp(\frac{(x-p_{old})^2}{2\sigma^2}) \tag{2.17}$$

where $p_{new(old)}$ is the new(old) parameter value and $\sigma = 0.1$ is the variance. The new generation is then evaluated and the GA iterates until a specified end point, usually a set number of iterations or a fitness threshold value. For SWGs, the initial values do not need to be accurate. Reasonable values are $\Lambda = \lambda_{tar}/2$, $FF = 0.5$, and $t_{g,s} = \lambda_{tar}/3$. Even with these very rough guesses the GA routinely converges in under 100 iterations, a doable task for modern personal computers.

2.4.2 Subwavelength Grating Fabrication

One of the prime advantages of SWGs over other IR filtering techniques is its straightforward fabrication. SWGs require minimal processing steps and are compatible with most standard microfabrication technologies, as they do not introduce material or thermal restrictions. The basic microfabrication flow is outlined in Fig. 2.9 and is applicable to the silicon SWGs in Chapters II and IV as well as the GaAs SWGs in Chapter III.

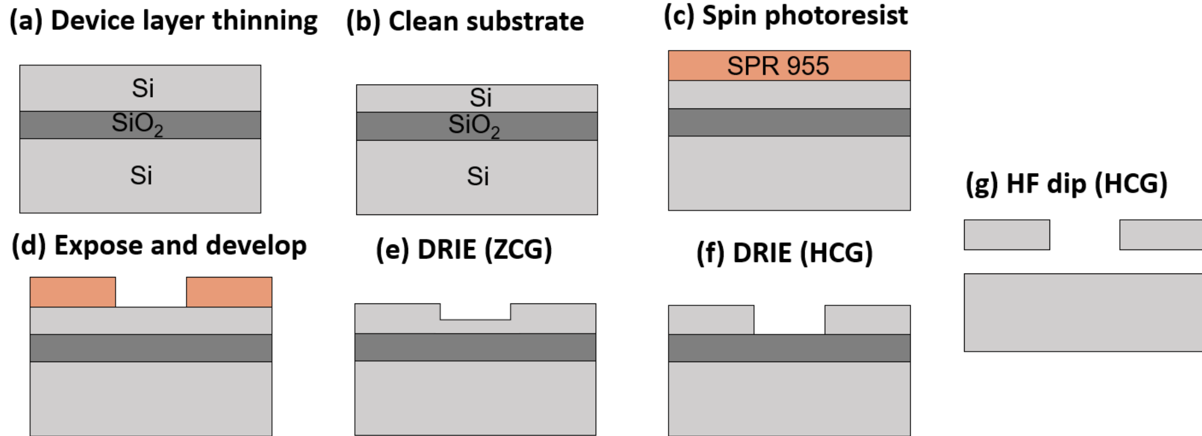

Figure 2.9: Basic SWG microfabrication process flow. a) Thin device layer to target thickness b) Clean substrate with solvents and a plasma descum. c) Apply adhesion promoter and spin photoresist. d) Expose and develop grating pattern. (e,f) Dry etch to define e) ZCGs and f) HCGs. g) Dip in HF to release HCGs from the etch stop.

Si gratings are fabricated on commercial silicon on insulator (SOI) wafers with the specifications given in Table 2.1. Before processing, the wafer is coated in a protective layer of photoresist (PR) and diced into ≈ 2x1 cm^2 pieces. Since the device layer is initially 4 μm thick, it is thinned to the designed thickness with a SF_6 reactive ion etch. After thinning, the substrates are thoroughly cleaned using acetone and isopropyl alcohol (IPA), followed by a rinse in deionized water and dried with compressed N_2. A low-power oxygen plasma removes any organic residue (100 W, 35 sccm O_2). A vapor deposited layer of hexamethyldisilazane (HMDS) promotes PR adhesion by bonding to OH^- groups in silicon's native oxide, creating a hydrophobic surface. Next, a 1 μm layer of PR is spin coated at 3000 rpm (MEGAPOSIT SPR 955), followed by a 90 s dehydration bake at 115°C. The PR is exposed using a projection lithography system (GCA AS200 AutoStep, λ = 365 nm). A 90 s, 115°C post exposure bake promotes diffusion of photo-activated compounds in the PR. Development is performed using a spin developer system (MicroChemicals AZ 726 MIF). The samples are then subject to another low-power oxygen descum and mounted to a 100 mm Si wafer coated with a 2 μm oxide layer. The grating pattern is transferred to the silicon via deep reactive ion etching (DRIE). Deep, vertical features are achieved using the switched Bosch process,

wherein the DRIE process alternates between a SF_6/O_2 etch and a C_4F_8 deposition for sidewall protection. As shown in Figure 2.9(e,f), in ZCGs the DRIE step is timed to achieve the appropriate grating and slab thicknesses, while in HCGs the etch reaches the buried oxide layer. To release HCGs, the samples are placed in 49% hydrofluoric acid (HF) for 4 min, taking advantage of the very high selectivity between Si and SiO_x. Lastly, the PR is stripped using a high power oxygen plasma (800 W, 80 sccm O_2).

Parameter	Specification
Diameter	100 mm
Crystal Orientation	$< 100 > \pm 0.5°$
Polish	Front and back side polished
Device Layer	Undoped, $> 1,000\Omega$-cm FZ silicon
Device Layer Thickness	4 ± 0.5 µm
Buried Oxide	Thermal oxide
Buried Oxide Thickness	4 µm ±5%
Handle Wafer	$>$1,000 Ω-cm FZ silicon
Handle Wafer Thickness	500 ± 15 µm

Table 2.1: Specifications of the commercial SOI wafer.

2.4.3 Optical Characterization

Spectral transmittance is measured using Fourier transform infrared spectroscopy (FTIR). Measurements are carried out on a Perkin-Elmer GX FTIR with AutoIMAGE microscope attachment. To allow for LWIR characterization, the system uses a KBr beam splitter and a liquid nitrogen cooled MCT-B detector. An interferometer creates a time-domain interferogram consisting of a range of frequency components. This signal passes through the grating sample to the detector, after which a digital Fourier transform recovers the spectral transmittance profile. Taking the ratio of this measurement to an air background approximately yields the grating transmittance spectrum. Polarization dependence is determined by placing a gold wire-grid polarizer in the beam path of the incident light. Resolution is set to 4 cm^{-1}, which is small enough to resolve the narrow resonance peaks in the following studies. Figure 2.10 shows a schematic of the optical setup.

A drawback to this technique stems from the Cassegrain objectives in the FTIR optics. The Cassegrain lenses permit light at an angle of incidence between 16° and 36°. To better approximate normally incident collimated light, several adjustments are made to FTIR optical beampath. To achieve normal incidence, the gratings are placed on a sample holder angled at 20° with respect to the stage. The range of incident angles is restricted by placing an iris in the incident beam path.

Iris size is chosen to minimize the numerical aperture while still permitting useful signal power. Most measurements are performed with a $\pm 4°$ range of incident angles.

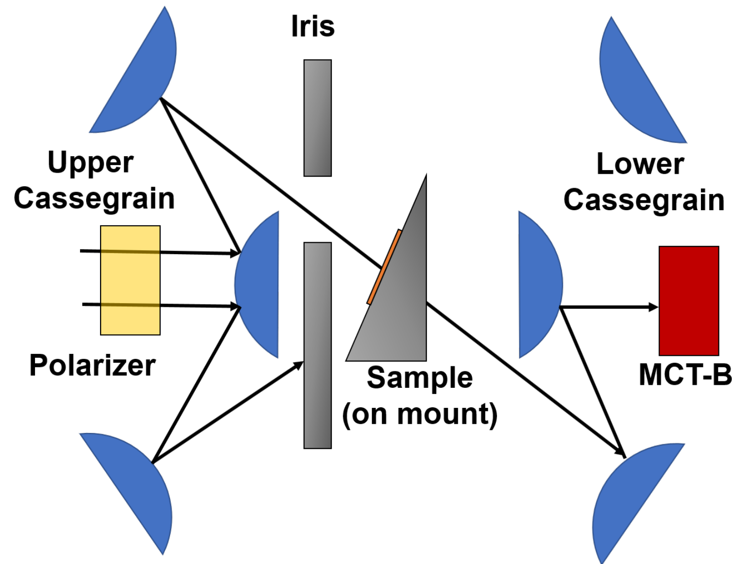

Figure 2.10: Schematic of the FTIR optical setup.

2.5 1D Zero-Contrast Grating MWIR Transmittance Filters

With the principles and methods outlined in the preceding sections, high-Q MWIR transmittance filters are realized by Si/SiO_2 ZCGs. This work fulfills two goals: experimentally demonstrate the viability of ZCG filters and improve the Q achieved by prior MWIR SWG filters. An enhanced Q is achieved using innovative fabrication and optical characterization techniques. The ZCGs presented in this section are periodic along one direction (1D) and are therefore strongly polarizing. This work was presented in Reference [68].

For operation in the MWIR, the ZCG design uses the air/Si/SiO_2 material system. Though the ZCG geometry prevents chemically etching the buried oxide layer, SiO_2 is suitably low index and transparent. The complex refractive indices of Si and SiO_2 at λ = 4 µm are approximately 3.42+0i and 1.39+0.0004i, respectively [112]. The fabrication process follows Figure 2.9 through the DRIE process in step (e). To improve sidewall and surface morphology, a dry oxidation process thermally grows a 50 nm layer of oxide, followed by an HF dip for oxide removal. The gratings are dry-oxidized for 100 min at $1000°$C (the initial temperature is $400°$C with a $13°$C/min ramp rate). The resultant surface is smoother than the initial post-etch surface as a consequence of diffusion-limited oxidation [113], as depicted in Figure 2.11a. Figure 2.11b shows atomic force microscopy (AFM) images of the ZCG surface before and after the oxidation and etch treatment, proving the

gratings are visually and empirically smoother.

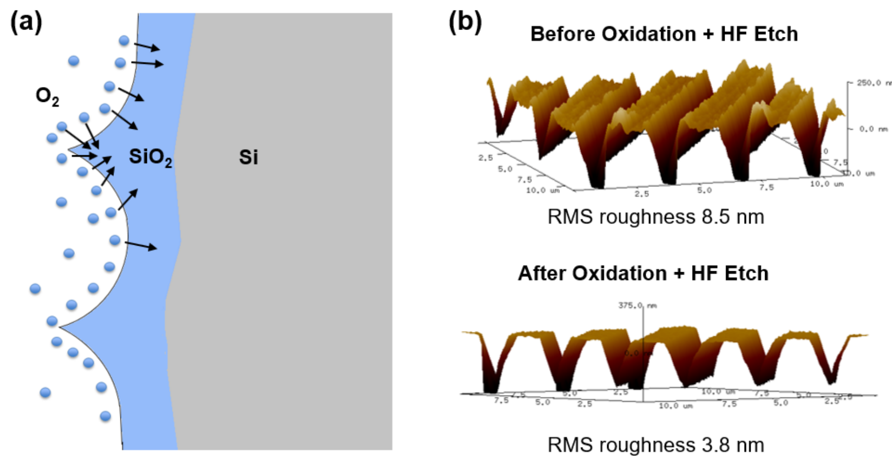

Figure 2.11: a) Schematic of surface smoothing by thermal oxidation and etching. b) AFM images of the ZCG surface before and after the oxidation and etch treatment.

Figure 2.12b shows the experimental transmittance spectrum for the ZCG pictured in the SEM image in Figure 2.12a. The best filter demonstrates high peak transmittance efficiency (T $>$ 40%), broadband high-reflectivity (R $<$ 20% from 3.6-5.5 μm), and a small footprint (40 periods, $\approx$ 100x100 μm^2). The greatest experimental Q is 175. Comparison to simulation shows strong agreement, yet with a less efficient peak, lower Q, and increased side band power. To obtain a better fit, the simulation accounts for material absorption, Fresnel reflection at the lower SiO_2/Si interface (R $\approx$ 30%), and oblique incidence during optical characterization. The remaining discrepancies are attributed to fabrication variability, the finite periodicity nonideality, and non-resonant scattering from residual surface roughness. Compared to an unoxidized control SWG, the oxidation and etch process improved transmission efficiency by 22% and Q by 34%. Measured transmittance spectra comparing unoxidized and smoothed SWGs are shown in Figure 2.13.

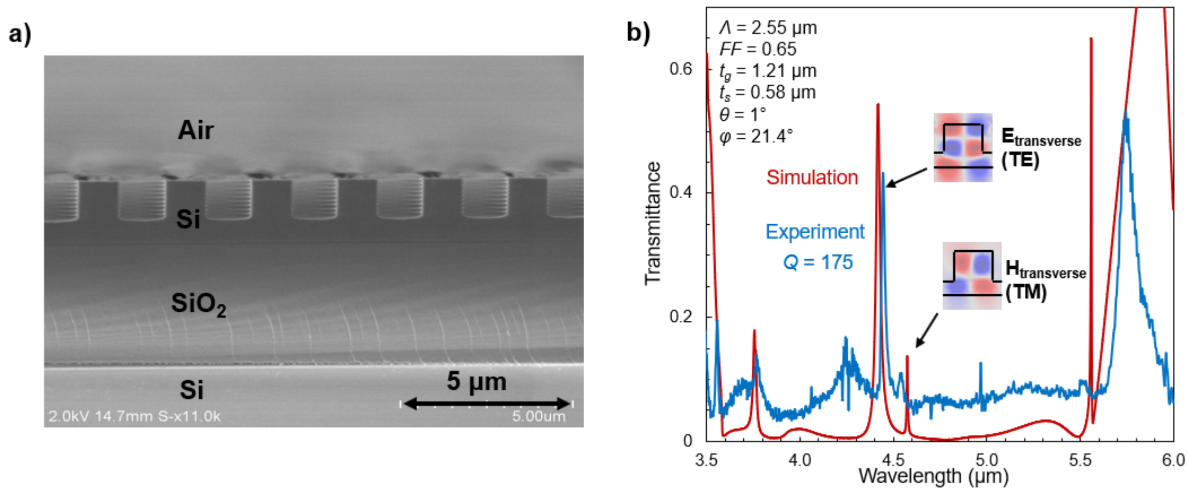

Figure 2.12: a) Scanning electron micrograph of a cross-sectioned air/Si/SiO_2 ZCG MWIR transmittance filter. b) Experimental transmittance spectrum of ZCG in (a). The insets show FEM-calculated field profiles for the resonances at 4.45 µm and 4.6 µm. Figure referenced from [68].

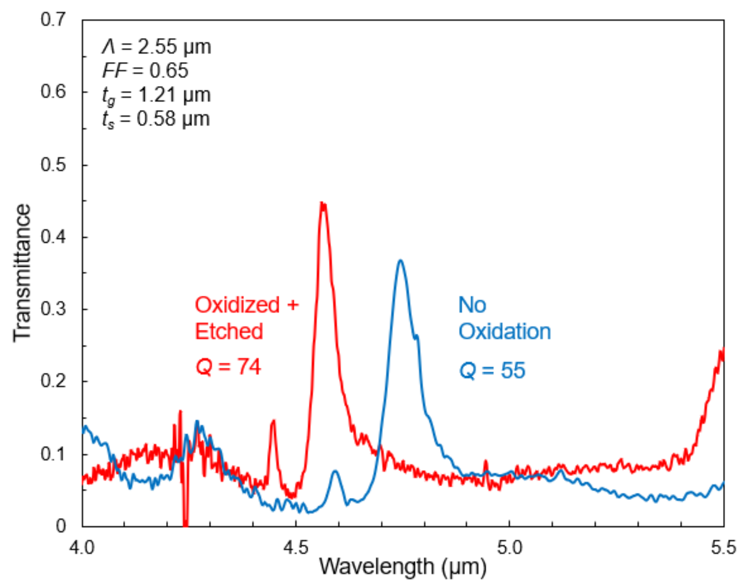

Figure 2.13: Experimental transmittance spectra showing the effects of surface smoothing.

Physical constraints in the FTIR optical setup make it difficult to realize true normal incidence excitation. While often an inadvertent source of frustration, a large azimuthal tilt reveals interesting physics. The experimental optical configuration contains a polarizer to permit only nominally TM-polarized incident light. However, obliquely incident light contains a component of the E-field perpendicular to the gratings, effectively mixing TE- and TM-polarizations. Thus, the total optical response is a linear combination of orthogonal polarization responses, per the Fresnel-

Arago laws. The insets in Figure 2.12b show the out-of-plane modal field profiles for the two resonant peaks near 4.5 μm. Clearly, the transmittance spectrum contains resonances with both TE and TM modal field profiles. In this configuration, the TE mode is very prominent since ϕ is large. The highlighted modes have odd symmetry and are therefore symmetry-protected at normal incidence. TE modes couple more weakly than TM modes, characteristically allowing higher Q factors. This phenomenon is presented in Figure 2.14. For a similar degree of asymmetry ($\theta \approx \phi$), the TE mode has a narrower linewidth, an important practical consideration. An explanation follows from the Maxwell equations. The E-field is continuous when parallel to an interface; when the E-field is perpendicular, the interface condition is

$$\epsilon_{Si} E_{Si} = \epsilon_{air} E_{air} \tag{2.18}$$

Under TE polarization, light can concentrate in the dielectric because the E-field does not cross any interfaces, whereas the continuity condition forces TM-polarized energy into the air gaps [94]. Therefore, TE modes have less overlap with incident radiative states, allowing higher Q.

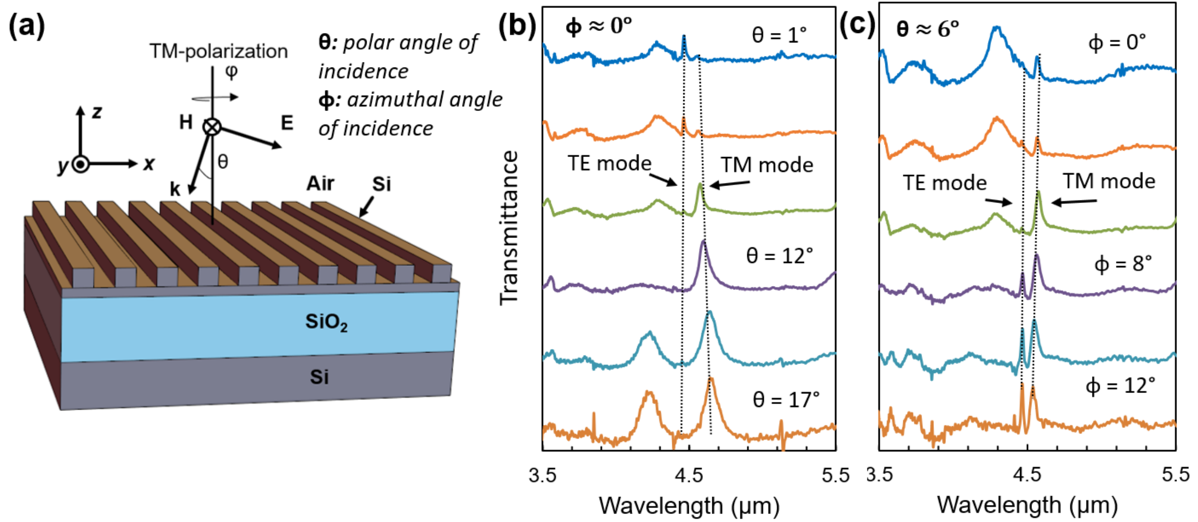

Figure 2.14: a) Schematic of a ZCG, defining polarization states and incidence angles. b) Grating response for varying polar angle θ for fixed $\phi = 0°$. c) Grating response for varying azimuthal angle ϕ for fixed $\theta = 6°$. Figure referenced from [68].

2.6 2D Zero-Contrast Grating MWIR Transmittance Filters

Though the 1D ZCG filters demonstrated promising performance, the bandpass optical response is highly polarization-dependent. As shown in Figure 2.15, quality filter performance occurs for the designed TM-polarization state, while the TE-polarization response is less useful. The polarizing

nature of 1D SWGs is an expected consequence of the boundary conditions imposed by Maxwell's equations. The transverse electric field is continuous across a dielectric boundary but follows Equation 2.18 when the field is normal to the boundary (assuming no surface charge). Intuitively, a 1D SWG's dielectric function changes significantly when rotated $90°$ about the z-axis (see Figure 2.14a). For 1D SWGs, ensuring the filter response matches the designated polarization requires an external polarizer or knowledge of the incident polarization state.

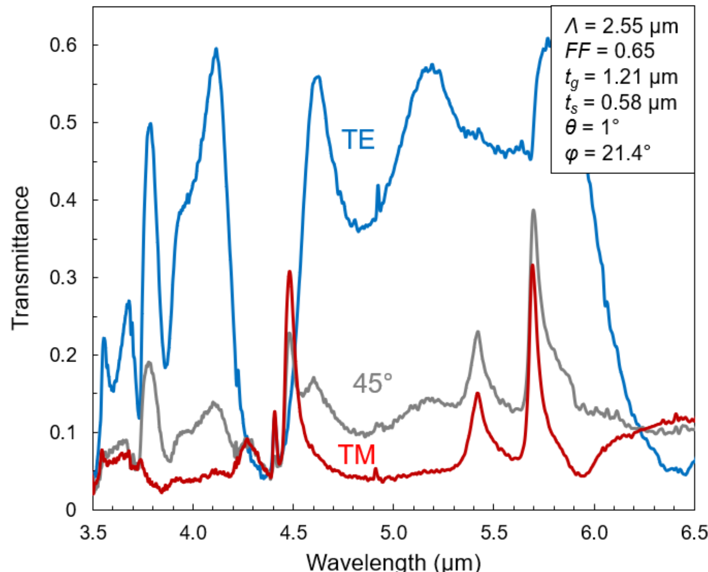

Figure 2.15: Experimental transmittance spectra of the 1D ZCG for TE- and TM-polarization and an intermediate polarization $(45°)$ containing equal TE and TM components.

There are many instances when polarization-independent filtering is desirable. Configuring an external polarizer adds bulk and complexity to the optical setup. Furthermore, a linear polarizer attenuates over 50% of incoherent light, a significant hindrance for low-flux IR optics. Fortunately, structures with a $\leq \pi/2$ rotational symmetry are inherently polarization-independent [114], such as grating elements arrayed in square or hexagonal lattices (2D gratings) [20, 22, 32, 38, 39, 44, 115, 116]. Though Reference [114] rigorously proves polarization independence in square and hexagonal SWGs, one may intuitively see that the dielectric function is the same in orthogonal directions.

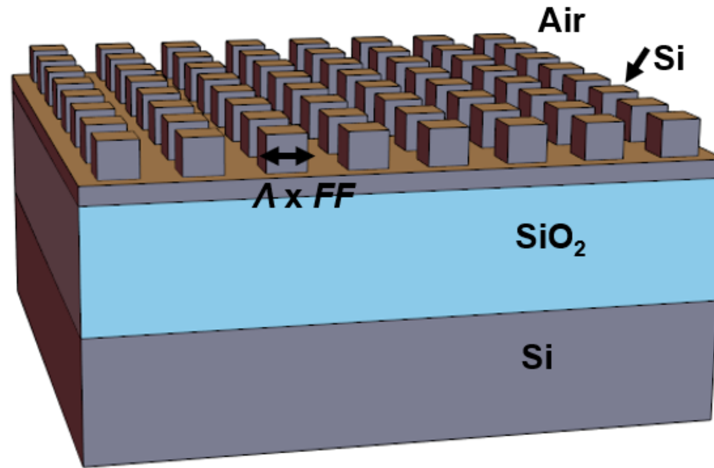

Figure 2.16: Schematic of a polarization-independent MWIR transmittance filter via a square lattice ZCG.

A schematic of a 2D air/Si/SiO_2 square lattice ZCG is shown in Figure 2.16. Save for the transition from 1D to 2D, the optimization, fabrication, and characterization techniques are identical to the 1D experiment. Figure 2.17a presents a tilted SEM image of the fabricated square gratings, revealing high morphological quality. The transmittance spectra in Figure 2.17b give an experimental(simulated) Q of 101(327). Allowing for the nonidealities enumerated in Section 2.5, the square lattice ZCGs respond reasonably closely to the simulated curves. Measuring the structures at two orthogonal polarizations demonstrates a high degree of polarization-independence. Similar results are obtained for hexagonal lattice ZCGs, with an experimental(simulated) Q of 93(145) and convincing polarization-independence (not shown).

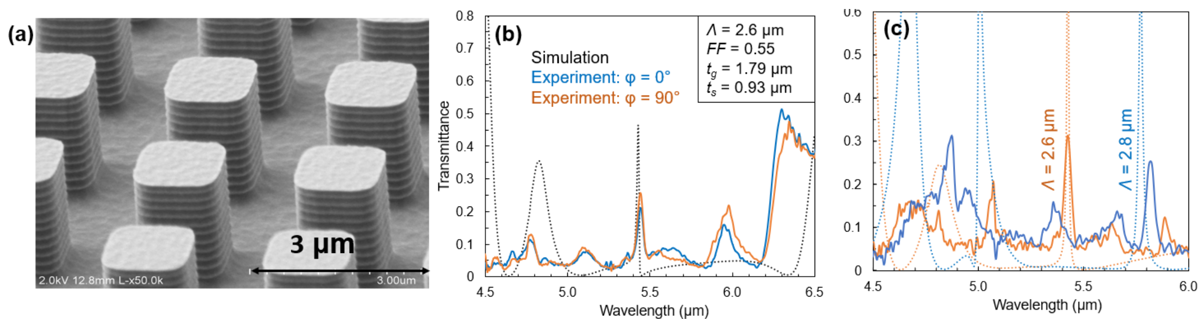

Figure 2.17: a) Tilted SEM image of a square array 2D air/Si/SiO_2 ZCG. b) Simulated transmittance spectrum (dotted curve) and experimental transmittance spectra (solid curves) for orthogonal incident polarization states. c) Experimental transmittance spectra for ZCG with two different periods. Figure referenced from [68].

2.7 Effects of Finite Periodicity

Up to this point each simulated SWG was assumed to have an infinite number of infinitely long grating bars. Of course this does not describe any physical structure. It is therefore worth studying the effects of finite periodicity in SWG filters. Recall from Section II.1 that once excited through an evanescent diffraction order, resonant guided modes laterally propagate a distance, *L*, before radiating back into space. The nature of a GMR is dependent on its interference with non-resonantly scattered light [117] as well as the interference between counter-propagating quasi-guided waves [118]. The simulation in Figure 2.18 displays the resonant field profile for a HCG with only 40 periods. Modeling a finite structure requires the use of scattering boundary conditions in place of the periodic Floquet boundaries. Though the resonance is strong near the center of the SWG, it is nearly lost at the edges. Light that propagates to a SWG edge is lost as lateral radiation, a nonideality that degrades filter efficiency and contributes to spectral linewidth broadening [69, 102, 119, 120].

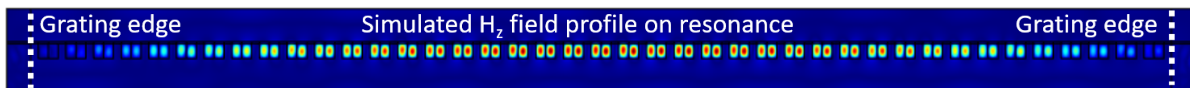

Figure 2.18: Resonant H-field profile for a HCG with 40 periods.

The effect of finite periodicity is closely tied to the lifetime of the GMR. Figure 2.19 compares the two cases, one with near-normal incidence and one with a large oblique angle. In Section II.2, it was shown that symmetry-protected modes in SWGs with rectangular symmetry are accessible by introducing an oblique angle of incidence. A larger angle of incidence allows for stronger coupling and consequently a shorter radiative lifetime. Laterally propagating GMRs travel a characteristic distance

$$L = c/\gamma n_{eff} \tag{2.19}$$

where c is the speed of light, γ is the total resonance decay rate, and n_{eff} is the mode's effective index. More strongly coupled modes have larger γ with proportionally lower *L*. Therefore, weakly coupled modes are more strongly affected by finite periodicity effects and require a larger number of periods to approach the optical response of infinitely periodic gratings. For the small θ in Figure 2.19a, the 25 period grating shows severe degradation, while for the larger θ, 20 periods results in only a $\approx$25% drop in efficiency. This illustrates an important trade-off between filter size and resolution: a narrower linewidth requires a greater number of periods.

Another interesting feature is the resonance shift with the varying numbers of periods. Upon first inspection this may seem unexpected, but consider again Figure 2.18. In finite SWGs with a

large number of gratings, the guided modes mostly exist at a large distance from the edges and are minimally perturbed from infinite gratings. By contrast, in gratings with few periods, the guided modes are always in the vicinity of an edge, causing a perturbation in the modal effective index with attendant dispersion.

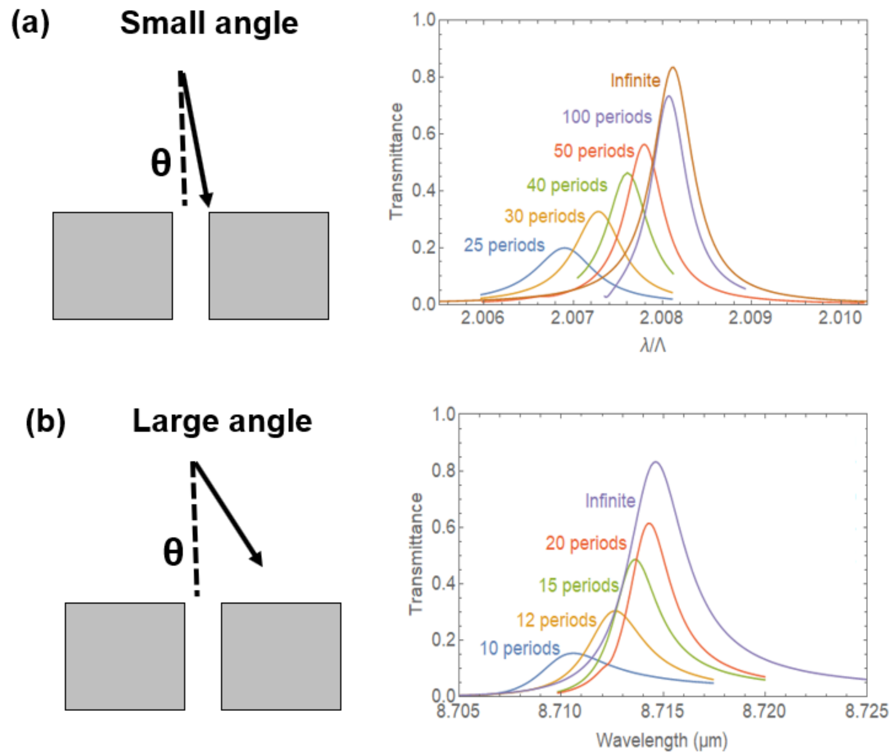

Figure 2.19: Simulated transmittance spectra for finite HCGs under a) near-normal and b) highly oblique incidence conditions. The spectra include HCGs with varying numbers of periods (simulated in a finite domain) compared to one of indefinite periodicity. Figure referenced from [69].

To verify the impact of finite periodicity, an array of Si HCG LWIR filters with varying number of periods was fabricated [69]. The experimental results clearly follow the trends predicted by theory. In Figure 2.20, Q and peak transmittance, T_{peak}, both monotonically increase with the number of periods. For this optical setup, approximately 25 periods are required before a significant performance drop-off is observed. Incrementally reducing the grating size then results in an outsize reduction in resolution. Gratings with more than 25 periods behave comparably, with the 200 period gratings showing only modest superiority.

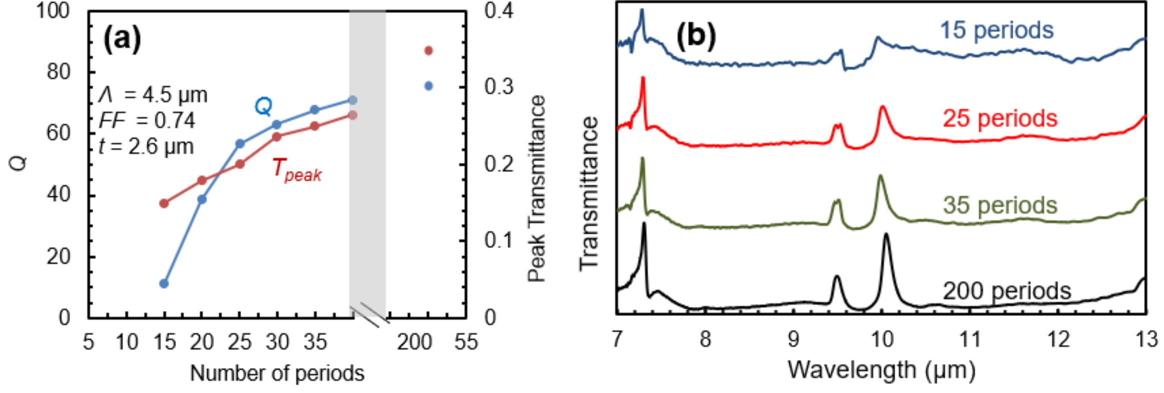

Figure 2.20: a) Quality factor (Q) and peak transmittance (T_{peak}) as a function of number of periods. b) Experimental transmittance spectra for varying number of periods. Each grating is 180 μm long. The angle of incidence is $\theta =\approx \pm 3°$ and $\phi =\approx 14 - 20°$.

In addition to having a definite number of periods, physical gratings also have finite length. Since 1D SWGs are only periodic in one direction, it is less clear what the importance of the length of the grating bars is. The phase matching condition is given by

$$[k_x sin(\theta) + 2\pi/\Lambda_x]\hat{\boldsymbol{x}} + k_y sin(\phi)\hat{\boldsymbol{y}} = \boldsymbol{k_{GMR}} \tag{2.20}$$

where θ and ϕ are respectively the polar and azimuthal angles of incidence as defined in Figure 2.14a. Incident light only diffracts in the directions of the grating modulation, that is, the *x*-direction. However, if the incident k-vector has a *y*-component (i.e. $\phi \neq 0$), the excited GMR may also propagate along the unmodulated direction. In this case, lateral loss also occurs at the grating anchors (the top and bottom edges in 1D SWGs). Measurements on gratings with varying line lengths support this theory. As shown in Figure 2.21, Q and T_{peak} monotonically increase with grating line length and begin to saturate around 90 μm. This study on finite gratings provides useful information about pixel size and resolution, such as would be needed in a hyperspectral imaging system. Figures 2.20 and 2.21 give clues about the minimum grating size needed to achieve reasonable filter performance. For the presented LWIR filters at the specified incidence angles, a filter size of 135 μm x 90 μm (1.22x10μm^2) gives a spectral resolution of 159 nm.

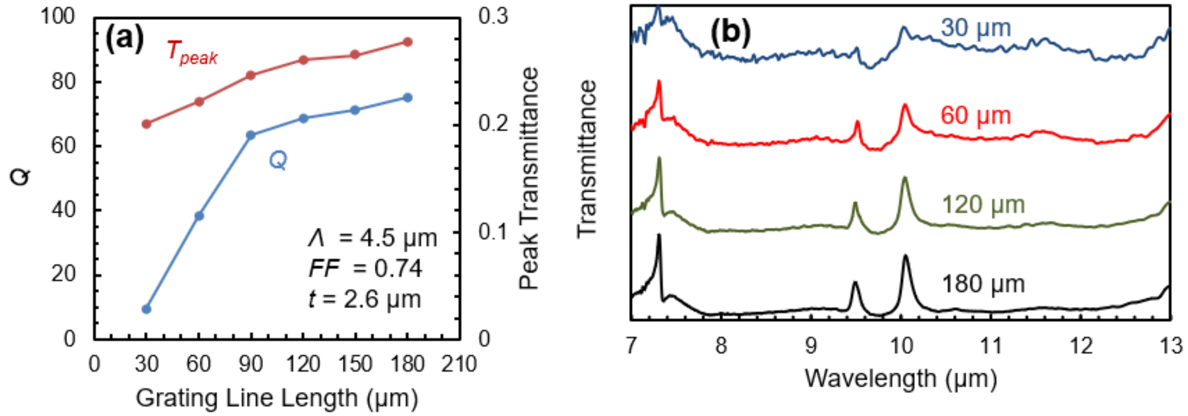

Figure 2.21: Quality factor (Q) and peak transmittance (T_{peak}) as a function of grating length. b) Experimental transmittance spectra as a function of grating length. Each grating is 40 periods. The angle of incidence is $\theta = \approx \pm 3°$ and $\phi = \approx 14 - 20°$.

Introducing reflectors at the grating edges can ameliorate the negative effects of the finite grating nonideality. Judiciously positioned reflectors create self-images of the guided resonances, effectively mimicking a periodic boundary condition. This class of grating, known as a cavity-resonator integrated guided-mode resonance (CRIGF) filter, has been demonstrated with dielectric distributed Bragg reflectors [121]. A CRIGF with metallic gold mirrors is illustrated in Figure 2.22a. Instead of being lost to lateral radiation, light reflects at the grating edge. Fig 2.22b shows transmittance spectra for two gold mirror CRIGFs, a finite grating, and an infinite grating. The distance between the SWG and reflectors, g, is optimized so that the incident and reflected waves interfere constructively. Two instances are given for the CRIGF. In the first, labeled "Gold reflectors: 4.48 μm" in Figure 2.22b, the gold mirrors are the same thickness as the gratings so that the structure is fully planar. In the other, the mirrors are infinitely tall and are able to reflect the evanescent fields that extend around the edges of the finite thickness mirrors. As expected, the CRIGFs offer superior filter performance than the finite grating without reflectors. Calculations were performed to determine the number of periods required to restore the transmittance peak to at least 70$\%$ of its ideal (infinitely periodic) value. With no reflectors, 37 periods are required. The infinite and finite CRIGFs required 16 and 21 periods, respectively.

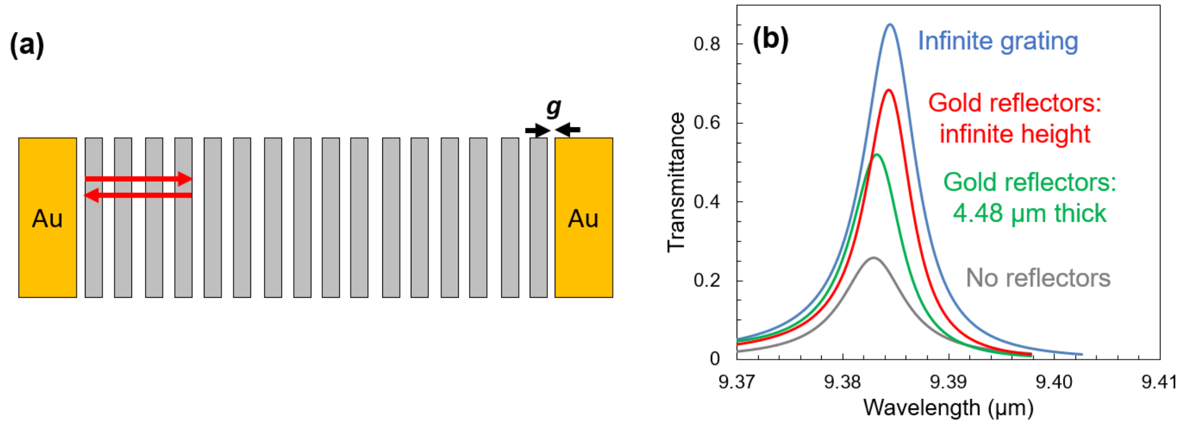

Figure 2.22: a) Schematic of a CRIGF employing gold metallic reflectors. b) Simulated transmittance spectra comparing the CRIGF to finite and infinitely periodic HCG filters. The SWG parameters are Λ = 4.68 μm, FF = 0.65, t_g = 2.82 μm, and t_s = 1.66 μm. The finite grating and CRIGFs have 15 periods.

CHAPTER 3

GaAs High-Contrast Grating Transmission Filters

3.1 Introduction

The silicon on insulator (SOI) platform has many advantages for MWIR/LWIR SWGs and silicon photonics generally. Si has a large index contrast with its oxides throughout the IR. For instance, at λ = 5 µm, $n_{Si} = 3.42$ and $n_{SiO_2} = 1.33$ [112]. Si is highly transparent throughout the NIR to LWIR waverange while SiO_2 weakly absorbs below λ = 7 µm. Microfabrication processes are well-established for Si, SiO_x, and Si_xN_y, making these the primary materials in photonic integrated circuits. Furthermore, hydrofluoric acid (HF) is highly selective to SiO_x over Si, allowing easy release of Si structures. These characteristics make SOI an excellent platform for passive optical structures, yet silicon's indirect band gap makes it a poor candidate for active devices such as lasers and photodetectors. Direct band gap III-V semiconductors enable much higher device efficiency as electronic transitions may occur without thermal phonon assistance. Additionally, the SOI platform suffers from poor wafer uniformity associated with the wafer bonding and thinning processes used to fabricate SOI wafers. In commercial SOI wafers, the quoted device layer tolerance is often as high as $\pm$0.5 µm, a major limitation considering IR SWGs are typically under 2 µm thick. Epitaxially grown III-V layers, on the other hand, are routinely grown to nanometer tolerances.

Gallium arsenide (GaAs) presents an intriguing alternative to the SOI SWGs described in Chapter II. With a large index (n_{GaAs} = 3.3 at λ = 5 µm) and low absorption ($\kappa < 1x10^{-3}$) [122], GaAs offers similar optical performance to Si. Epitaxial growth techniques allow precise control of SWG thickness. A high-quality GaAs layer may be grown on its aluminum alloy (AlGaAs), though the index contrast is slight. Fortunately, HF is highly selective to AlGaAs with Al content $>\approx 70\%$, yielding suspended GaAs structures after removing the underlying AlGaAs layer as depicted in Figure 3.1.

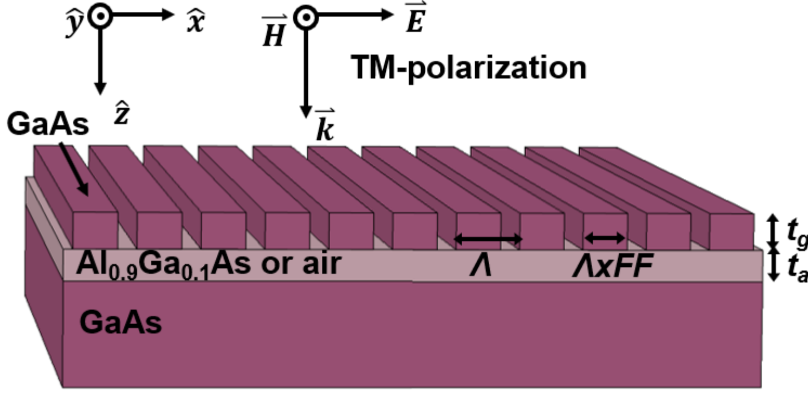

Figure 3.1: Schematic of a suspended GaAs/AlGaAs HCG. The etch stop layer is $Al_{0.9}Ga_{0.1}As$ before an HF dip, and air after.

Two considerations motivate the development of suspended GaAs/AlGaAs HCG filters: improved filter performance via precise device thickness control and direct integration with III-V optoelectronic devices. III-V HCG mirrors are already heavily utilized as top p-side mirrors in vertical cavity surface emitting lasers [123–125]. The narrow bandpass filters presented in Chapter II are another potential application. GaAs HCGs may be monolithically fabricated above a photodetector array since the gratings and diodes belong to the same material system, an important consideration for hyperspectral imaging systems. Transmittance filters are not the only application for high-Q resonant SWGs. Harnessing GMR opens possibilities for refractive index sensing [126, 127] and optical phase arrays [128]. Since optical structures do not require electronics-grade material quality, the suspended GaAs platform is potentially integrable with silicon via GaAs-on-silicon epitaxy.

3.2 HCG Design

HCG transmittance filters are designed for MWIR optical response. In high quality material there are no absorption lines below the band gap (1.441 eV at 300 K, λ_{cutoff} = 860 nm), giving characteristically low dispersion and absorption across the telecommunications wavelengths through the LWIR [122]. GaAs HCGs are therefore highly scalable. The MWIR is chosen as a compromise between patterning demands at shorter wavelengths and large layer thicknesses at longer wavelengths. The genetic algorithm from Section II.4 optimizes the grating geometry. An array of HCGs are patterned with nominal dimensions consisting of each combination of Λ = [2.65, 2.75, 2.85, 2.95, 3.05, 3.15] µm, FF= [0.68, 0.7, 0.72, 0.74, 0.76], and grating length = [30, 50, 70, 90, 115] µm. Each grating contains 40 periods. Given the strong polarization-dependence of 1D HCGs, the gratings are designed to operate under TM polarization, as defined in Figure 3.1.

Often overlooked in SWG studies, the air gap thickness (t_a in Figure 3.1) is another crucial design parameter. HCGs are well-modeled as lossy two-port systems consisting of a grating mode and ports at the cover and substrate high-contrast interfaces [117]. If the air gap is short, the grating mode evanescently couples to the substrate, effectively introducing a third radiation port. This is distinct from the two-port system, wherein resonant guided modes radiate into space and interfere with non-resonantly transmitted light and then propagate to the substrate. Instead, light coupled to the third port reaches the substrate without interfering with the background radiation. Consequently, this increases the radiative decay rate, leading to the linewidth broadening observed in the $t_a = 0.2$ µm curve in Figure 3.2a. The high-reflectivity background is also impacted by the air gap thickness, though the non-resonant optical response is determined by Fabry-Pérot interference rather than GMR. HCGs furnish broad high-reflectivity bands via interference between vertical waveguide modes in the grating bars and the grating gaps [129], a mechanism that is perturbed by the substrate proximity.

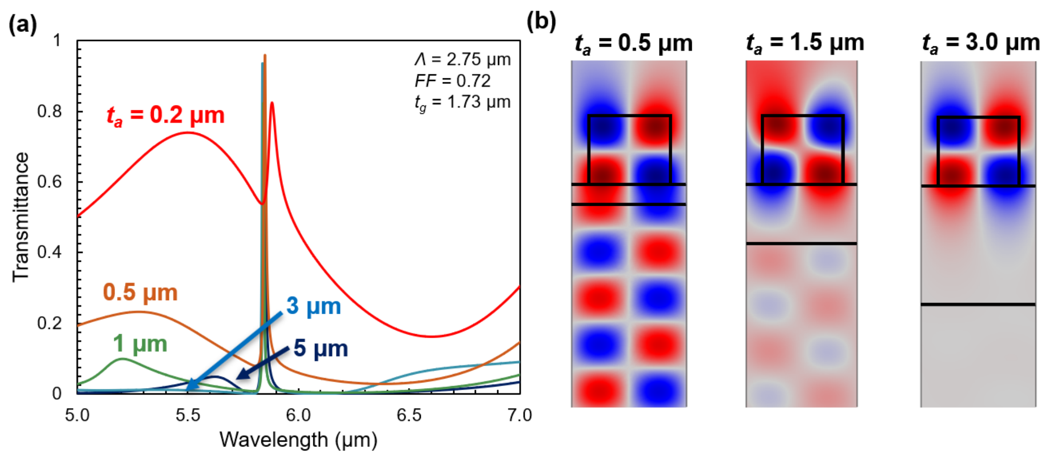

Figure 3.2: a) Simulated transmittance spectra for varying air gap heights, t_a. b) Normalized E-field for three representative air gaps on resonance ($\lambda = 5.85$ µm).

The simulation results in Figure 3.2a indicate that a 1.5 µm air gap is sufficient for HCG filters operating near 6 µm, even though this is only 25% of the resonant wavelength. Figure 3.2b shows resonant E-field profiles for three representative air gap distances. It is apparent that substrate coupling increases with shorter air gaps, such that the coupling is very strong for t_a = 0.5 µm and negligible for t_a = 3 µm. The choice of t_a = 1.5 µm is therefore an appropriate compromise between optical response and fabrication constraints. While wider air gaps theoretically improve filter performance, a thick AlGaAs layer increases fabrication cost/time and aggravates film strain.

3.3 Grating Fabrication

Suspended GaAs HCG fabrication follows the same high-level process flow in Figure 2.9, though the specific process details require modification to accommodate the different materials. The SOI and GaAs fabrication process flows diverge in two important ways. First, since anisotropic dry etch processes are less standardized for GaAs compared to Si, extensive etch development is required. Second, extra care must be taken to avoid damaging the brittle GaAs grating bars. This section describes developments for these process steps and summarizes the suspended GaAs/AlGaAs HCG fabrication results.

3.3.1 GaAs Dry Etch

The GaAs etch process defines the morphology of the grating sidewalls and is hence a critical determiner of filter performance. Excessive sidewall roughness can degrade high-Q spectral resonances [130], while undercut and sidewall slope can move the HCGs out of design tolerance by altering the effective filling factor. For high performance GaAs HCGs it is incumbent to obtain a dry etch process that yields smooth, vertical sidewalls for high aspect ratio (AR $>$ 2:1) features. Reactive ion etching (RIE), a directional plasma containing physical and chemical etch components, is the standard technique for fabricating high aspect ratio structures. To obtain satisfactory etch results, several RIE parameters must be optimized, namely etch chemistry, gas flow rates, chamber pressure, and forward bias voltage. Chlorine-based etch chemistries dominate GaAs RIE [131–136]. There is evidence that bromine-based RIE can achieve similar etch rates and sidewall smoothness as chlorine [137, 138], possibly due to Br being less electronegative than Cl.

The fabrication process begins with molecular beam epitaxy (MBE) on a GaAs (100) substrate (V80H MKII MBE system), performed by Yuanchang Zhang (Wright Patterson Air Force Base). After deoxidation, a layer of 200 nm GaAs buffer was grown, followed by a 1500 nm thick layer of undoped $Al_xGa_{1-x}As$ (x = 0.9) grown at 530°C, and lastly a 1730 nm thick layer of undoped GaAs layer grown at 580°C. The nominal growth rate for the full stack was roughly 0.5μm/hr with a beam equivalent pressure ratio BEP (Ga):BEP (As) of $\approx$1:3-5. Cleaning and photolithography precisely follow the processes described in Chapter II. Samples are cleaved to $\approx$1x2 cm^2 pieces and are mounted to a Si carrier wafer for RIE. An HBr-based inductively coupled plasma (ICP) reactive ion etch (LAM 9400 SE, LAM Research Corporation) transfers the HCG pattern into the GaAs layer. In ICP RIE, the energy for plasma ignition is supplied by electromagnetic induction and not the RF field referenced to the platen (electrode holding the sample). This allows a very high density of low energy ions, a useful combination for maximizing etch rate while minimizing surface damage. A 10 s breakthrough etch removes native oxides. The breakthrough process parameters are 5 mtorr chamber pressure, 300 W ICP power, 100 W RF power, and 60 sccm Cl_2

flow. The parameters for the main etch step are 30 mtorr chamber pressure, 600 W ICP power, 100 W RF power, 100 sccm HBr flow, and 100 sccm He flow. Appendix A.1 gives details behind the GaAs etch development. Figure 3.3 shows SEM images of the HCGs after etching the GaAs.

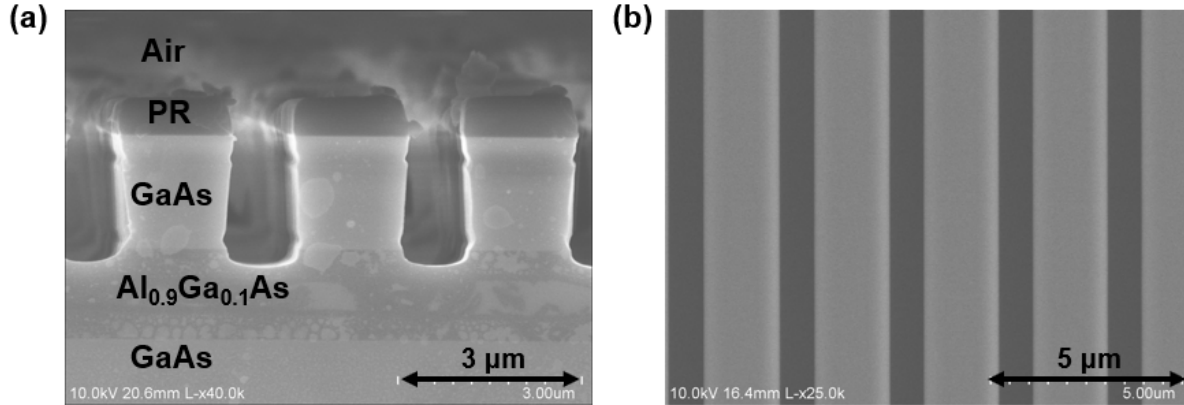

Figure 3.3: a) SEM cross-section of a HCG after the GaAs RIE step. b) Top-down SEM image of grating lines.

The SEM cross-section view in Figure 3.3a shows that the gratings are mostly rectangular, though there are several nonidealities related to the RIE process. Foremost, the grating sidewalls exhibit a -4° sidewall slope. This is a consequence of the formation of a passivation layer during the etch process. As shown in Figure 3.4, a layer clearly forms on the sidewalls during the etch process. Energy-dispersive X-ray spectroscopy (EDS) measurements indicate that this layer contains redeposited Si, a claim corroborated by other studies [133, 138]. Since the etch chemistry does not contain Si, it is highly likely that the Si is sputtered from the carrier wafer or quartz chamber lid. The passivation layer protects the HCG morphology by inhibiting lateral etch. After etching, this layer is removed by HF during the grating release step. Due to transport limitations, the passivation layer grows more slowly as the aspect ratio increases, a likely explanation for the observed sidewall taper. Though tapered, the sidewalls appear relatively smooth, save for a notch near the top of the gratings due to an overlong breakthrough step.

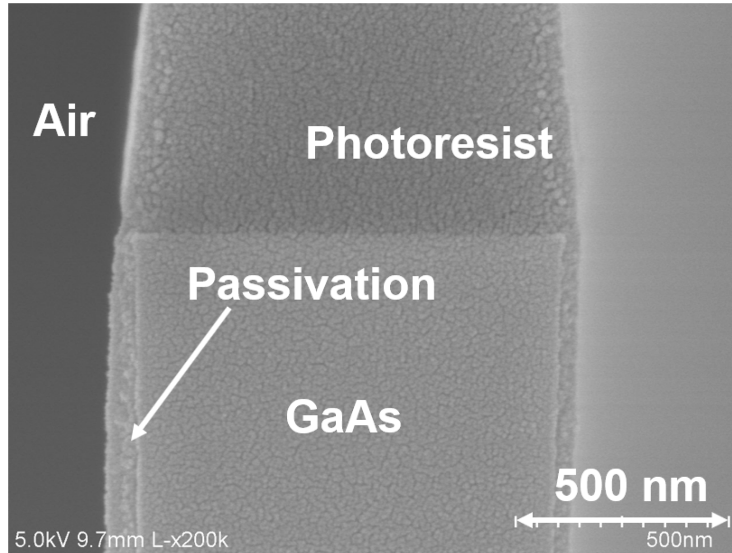

Figure 3.4: SEM image of an isolated grating line showing the Si-rich passivation layer. An isolated line is imaged for visibility, as the passivation thickness decreases with aspect ratio.

3.3.2 Gratings Release

After etching, the next step is to release the gratings from the AlGaAs layer. This step requires extreme care since III-V semiconductors are brittle compared to Si [139]. It is imperative to minimize mechanical stress during release, otherwise the gratings may suffer from stiction and mechanical failure. Before release, the photoresist etch mask is removed in a high power oxygen plasma (180 s, 150°C chuck temperature, 80 sccm O_2 flow, 8 sccm NF_3 flow, and 800 W RF power). HF very weakly attacks AlGaAs for Al concentration under $< 70\%$. In one study using a 7:1 DI H_2O:buffered oxide etch solution, $Al_{0.86}Ga_{0.14}As$ was etched at $\approx$15 nm/s while Al concentrations below $< 70\%$ had negligible etch rate [140]. The HCGs are released by a wet etch in a 1:5 mixture of HF(49%):H_2O for 90 s. Both HF and H_2O have large enough surface tension to destroy the released HCGs if allowed to dry [141, 142]. Thus, a liquid bead is maintained on the sample surface at all times during release, rinse, and transfer between beakers. After a gently cascaded DI H_2O rinse, the sample is placed in IPA. After a few minutes the water is evacuated from the gratings and the sample is placed in air to dry. This simple evaporation technique leverages IPA's low surface tension, giving comparable device yield to critical point drying. SEM images of the released gratings are shown in Figure 3.5.

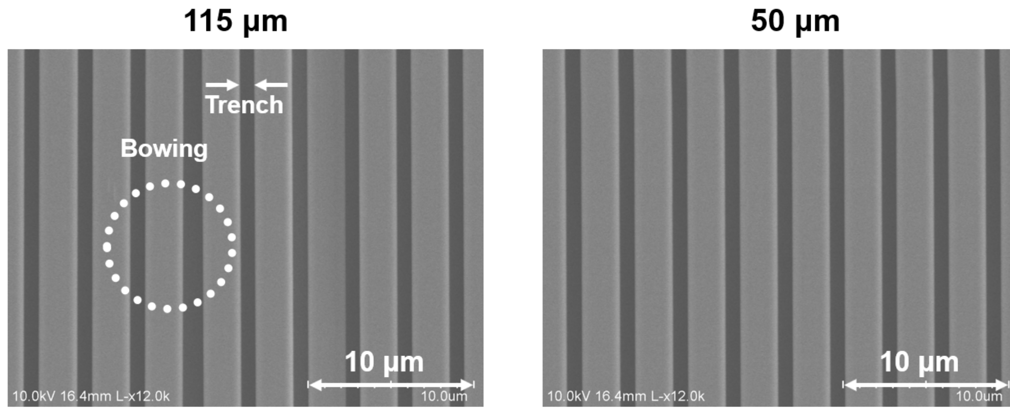

Figure 3.5: Top-down SEM images of 115 μm and 50 μm long HCGs after the release step. Images are taken near the center of the gratings. The white dashed circle draws attention to bowing.

As is apparent in Figure 3.5, the 115 μm long gratings exhibit pronounced bowing. The existence of bowing is further confirmed by post-processing SEM images to extract the distance between grating bars (labeled ”trench” in Figure 3.5). Figure 3.6 shows the distribution of trench widths for HCGs with varying lengths. The 115 μm grating contains a large outlier, denoting adjacent grating bars with opposite bowing inflection. Across the entire sample, bowing was not observed for any gratings shorter than 115 μm. This places an approximate limit on the suspended HCG length.

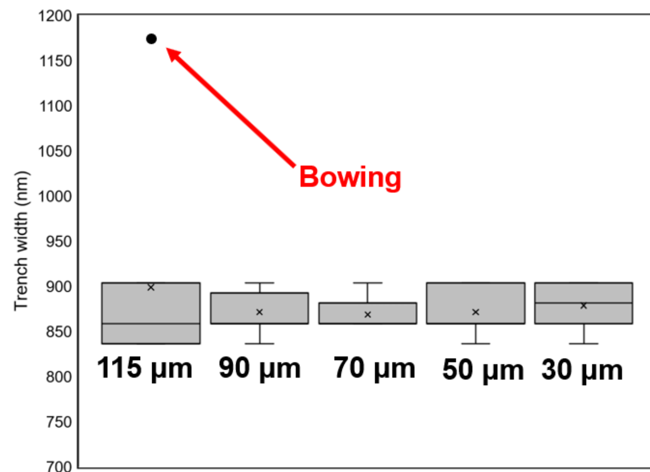

Figure 3.6: Statistical distribution of the measured trench widths for varying HCG lengths. Measurements are extracted from SEM images such as those in Figure 3.5. Images are taken near the center of the gratings and are averaged over 10 measurements.

3.4 Optical Performance

The gratings are characterized using the FTIR setup described in Section II.4. As shown in Fig. 3.8a, the measured transmittance spectra strongly agree with simulated response for TM polarization and $\approx$±3° angle of incidence. Due to the -4° sidewall taper, the actual fill factor is decreased by about 0.05. Although the nominal *FF* of the experimental HCG in Figure 3.8 is 0.72, adjusting *FF* to 0.66 gives much closer agreement to the numerical model. The reduced *FF* correctly predicts the resonant blueshift, since removing dielectric material from the grating cell increases the modal energy, corresponding to higher energy (shorter wavelength) photons. As shown in Figure 3.7, this magnitude of sidewall slope negligibly affects filter performance. The remaining discrepancy between simulation and experiment is attributable to other nonidealities, including sidewall roughness [68, 130], finite periodicity [69, 102], and reflection at the high contrast interfaces of the handle wafer [40]. The latter effect accounts for a nearly 30% transmittance loss. Since the model employs a plane wave at $\theta = 3°$, Q is also degraded due to the optical setup's $\approx$±3° cone of incident light. Figure 3.8b shows measured transmittance spectra for HCGs with varying *FF*, Λ = 3.15 μm, and 90 μm long. Q values $>$50 are experimentally observed. As expected, the resonance wavelength redshifts with *FF* and Λ (not shown).

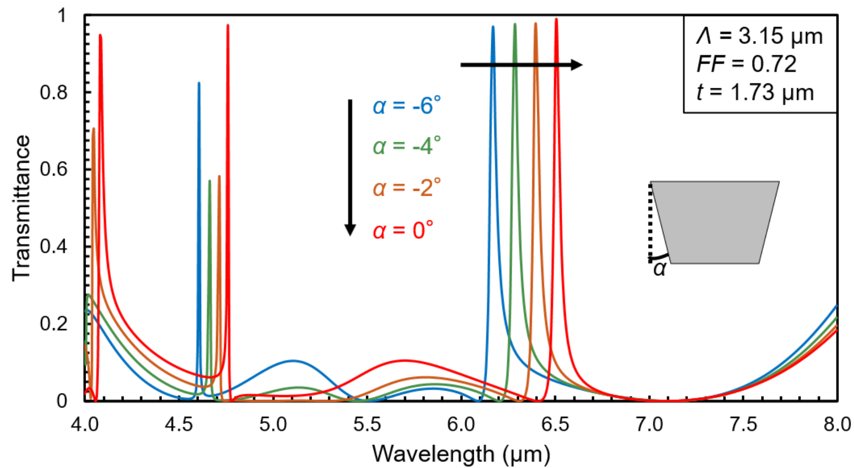

Figure 3.7: Simulated transmittance spectra for GaAs HCGs with varying sidewall slope.

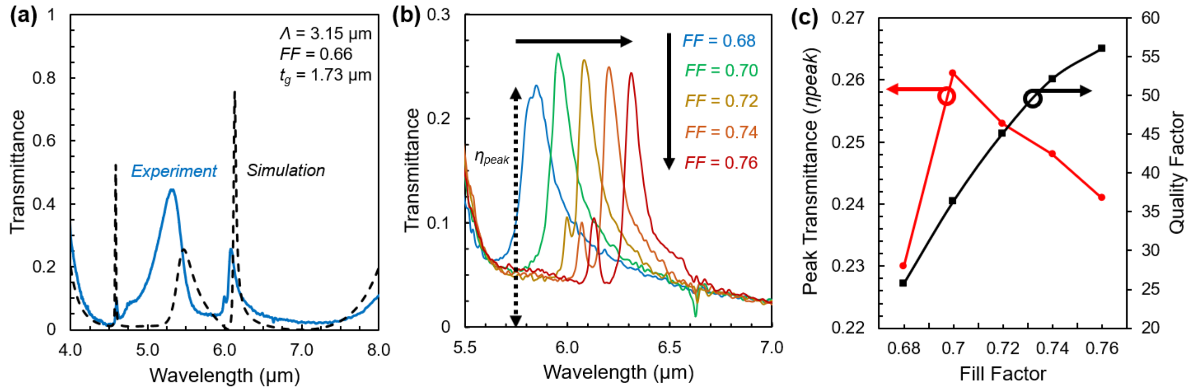

Figure 3.8: a) Experimental and simulated transmittance spectra for a suspended GaAs/AlGaAs HCG. b) Experimental transmittance spectra for HCGs with varying FF. c) Measured Q and peak transmittance for the curves in (b). All measurements refer to HCGs 90 μm long with $\Lambda = 3.15$ μm and are referenced to an air background.

As alluded to in the previous paragraph, reflection at the GaAs handle wafer causes a significant reduction in the measured peak transmittance. To better understand the intrinsic grating performance, transmittance spectra are referenced to the GaAs handle wafer. Figure 3.9 remeasures the structures in Figure 3.8b using the GaAs handle wafer as the reference spectrum. The peak efficiencies are improved by over 30%, proving that absorption and reflection in the handle wafer are partly responsible for the low efficiency observed in Figure 3.8. This result has technological importance. In most optical systems, the gratings would be directly integrated with photodetectors or other surface components, precluding the need to transmit light completely through the handle wafer. While these results are promising, further process development may boost filter performance. Better optimizing the GaAs etching process can reduce sidewall roughness and taper. A larger air gap is also expected to encourage a more ideal optical response.

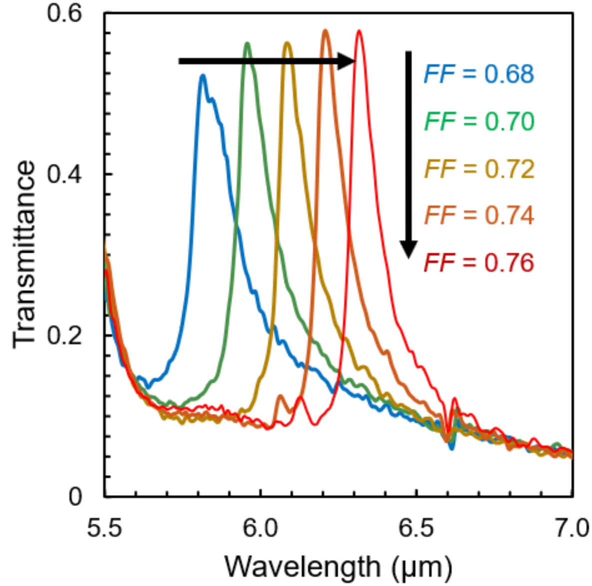

Figure 3.9: Figure 3.8b remeasured with a GaAs handle wafer reference.

Table 3.1 places this work in the context of past MWIR/LWIR SWG filters. Refs. [41, 42, 45] are reflectance (notch) filters, yet still provide insightful comparison. In this section, peak efficiency (η_{peak}) refers to the maximum transmittance(reflectance) of bandpass(notch) filters. The MWIR/LWIR offers minimal options for optical characterization, thus these studies all use a non-collimated FTIR beam. In comparing Q, it is difficult to separate the influence of the optical setup from that of the grating response. Still, the suspended GaAs HCGs are comparable to past works, and especially the other bandpass filters in [68] and [40]. In the MWIR, limited materials are available for achieving favorable index contrast. This leads several groups to use exotic materials like SrF_2, CaF_2, and ZnSe. Though low-index, these materials present many difficulties during device fabrication and are not necessarily compatible with other components. The suspended GaAs/AlGaAs platform, on the other hand, is directly integrable with other III-V devices.

Ref.	Materials	Peak wavelength (µm)	η_{peak} (%)	Q	Transmittance /Reflectance
This work	GaAs/Air	6.31	57	56	Transmittance
[42]	SiN_x/CaF_2	4.13	84	240	Reflectance
[41]	Ge/SrF_2	≈7.5	≈80	≈25	Reflectance
[45]	Ge/ZnSe	9.6	≈100	23	Reflectance
[68]	Si/SiO_2	4.44	43	175	Transmittance
[40]	Si/Air	≈10.9	≈34	44	Transmittance

Table 3.1: Summary of previous work in SWG filters, highlighting the grating materials and key performance metrics. The approximate values are estimated from published figures.

CHAPTER 4

Access to Symmetry-Protected Modes in Asymmetric Subwavelength Gratings

4.1 Background

The description of guided mode resonance in Chapter II suffices as a primer to resonant SWG filters, but is in many ways incomplete. This section provides a fuller view of SWG physics, providing theoretical insight into the uniquely shaped gratings presented in this chapter.

4.1.1 Photonic Bound States in the Continuum

A full appreciation for resonant SWGs calls for an introduction to the extraordinary field of photonic bound states in the continuum (BIC) [143]. BICs are a general wave phenomenon and were first proposed for a hypothetical quantum system containing a bound electronic state with energy above the bounds of a potential well [144]. Irrespective of the medium, a BIC's defining feature is its infinite lifetime despite existing in an open system with leakage channels into the continuum. This is an incredible result. The electron in a BIC state, for example, remains localized despite having a higher energy than the bounding potential well! A true BIC has infinite lifetime and is therefore inaccessible. Additionally, even if external leakage channels are prohibited, internal damping induces finite lifetime. Thus, technologically useful BICs are in actuality quasi-BICs, since a non-zero decay rate is necessary to excite the bound state. Going forward, use of "BIC" refers to finite lifetime quasi-BICs unless explicitly stated otherwise.

Electromagnetic BICs are of growing importance in photonic device research. Two characteristics of BICs make them exceptionally useful in photonic technologies. As observed in the HCG filters in the previous chapters, high-Q modes manifest narrow spectral features. Naturally, this is useful for bandpass/notch filters as well as all-pass filters, where the sharp resonances can produce a full 2π phase shift over a short modulation waverange. This latter purpose has been put to good use in beam steering applications [145]. Perhaps more importantly, the enhancement of a mode's

electromagnetic fields is proportional to the mode's lifetime. In this respect, the applicability of photonic BICs is quite broad. Applications include second harmonic generation (and enhancement of nonlinear effects, generally) [146], lasing [147], light guiding [148], perfect absorption [51], and refractive index sensing [18, 126]. Figure 4.1a depicts a schematic of a BIC in a SWG. At normal incidence and in the absence of material absorption, the symmetry-protected guided mode resonances possess infinite lifetime. As shown in the dispersion relation in Figure 4.1b, guided mode resonances (GMR) overlap with the radiative states, indicating that phase matching and energy conservation conditions are met. However, energy does not leak from the gratings due to the mode's symmetry-protection at normal incidence. In periodic photonic surfaces, a pair of bands split at the highly-symmetric band edge ($k_x = 0$). The symmetry-protected BIC comprises the lower branch and is often referred to as the dark mode due to its inaccessibility.

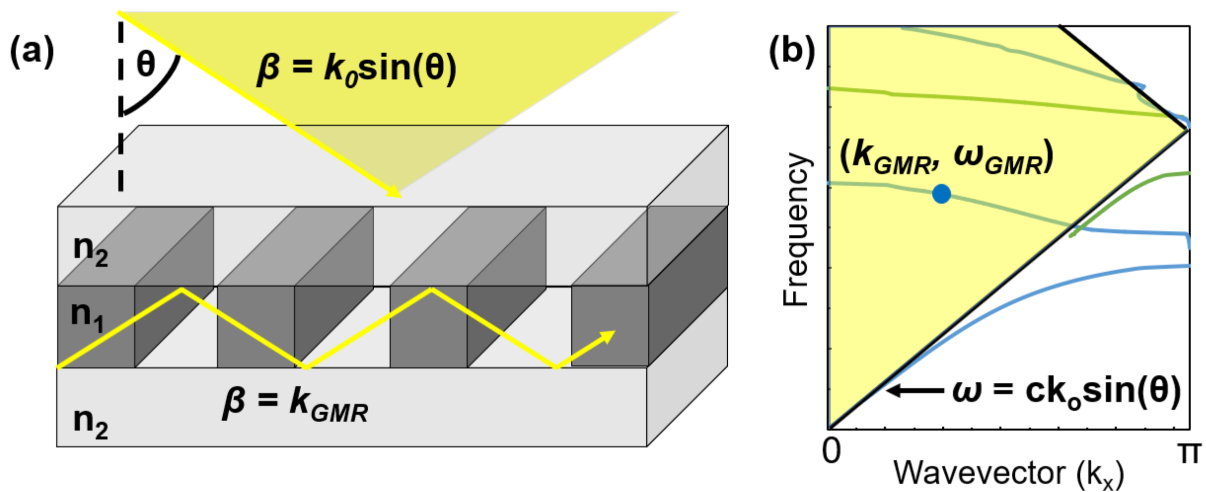

Figure 4.1: a) Illustration of a SWG showing a guided mode resonance and the continuum of radiative states. Incident light has a continuous distribution for incident angle, θ, and wavenumber, $k_0 = 2\pi/\lambda$. b) SWG dispersion relation showing discrete, bound states within the radiative continuum (yellow region).

A distinction should be made between two classes of BICs. Symmetry-protected BICs will be referred to as "stable BICs", since the BIC is totally insensitive to the grating geometry so long as the symmetry operations are preserved. Rectangular gratings at normal incidence are an example. One sees that the symmetry mismatch persists for every combination of grating period, fill factor, thickness, and (isotropic) refractive index. "Accidental BICs", on the other hand, exist for specific grating geometries where complete destructive interference between grating modes blocks radiation channels. This phenomenon finds some analogy with electromagnetically induced transparency [149]. Accidental BICs can be found via parameter sweeps and are highly sensitive to geometry [150].

4.1.2 Group Theoretical Analysis

Now that the symmetry-protected modes are identified as stable BICs, it is incumbent to define selection rules for accessing these high-Q states. Group theory provides a complete picture of the situation. Stated briefly, a grating mode is only accessible if it belongs to the same irreducible representation as the incident plane wave [151]. That is, for every symmetry operation the mode field profile must transform in the same way as the plane wave. A depiction of the symmetry operations are shown in Figure 4.2. The symmetry operations include mirror symmetry (e.g. σ_x is a reflection across the yz-plane), rotational symmetry (e.g. C_{2x} corresponds to a 180° rotation about the x-axis), inversion symmetry, i (inverting all points through a central point), and the identity operation, E. At the Γ-point, rectangular 1D gratings belong to the D_{2h} point group. The character table in Table 4.1 lists the symmetry operations for each irreducible representation of the D_{2h} point group. A value of 1(-1) indicates a symmetry(antisymmetry) after the given symmetry operation. Since the magnetic field is a pseudovector, mirror operations are improper rotations and therefore have inverted sign.

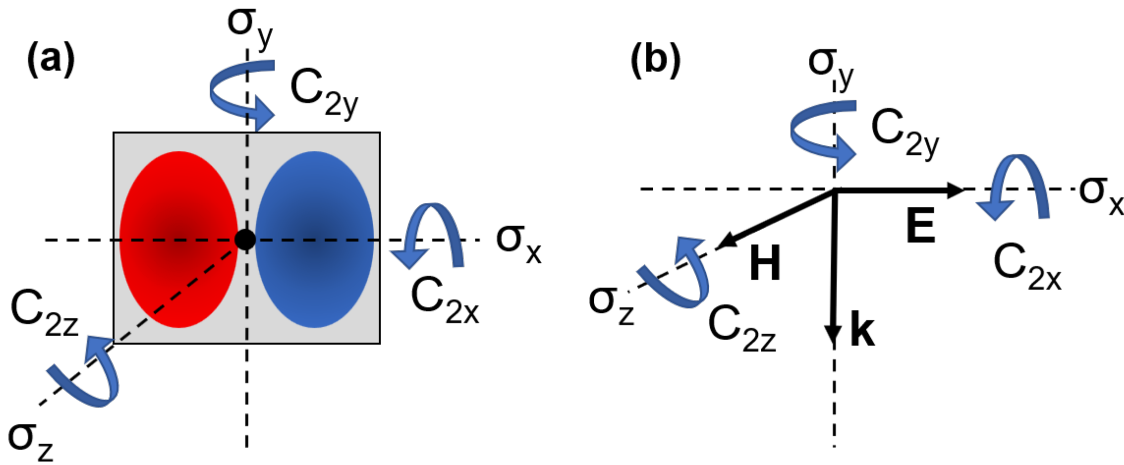

Figure 4.2: a) Illustration of the transverse component of the magnetic field of the first-order stable BIC (for TM-polarization) in a rectangular SWG. b) Components of a normally incident TM-polarized plane wave. Both (a) and (b) define reflection symmetry planes (σ_j) and 180° rotational symmetry axes (C_{2j}), where j is one of the Cartesian directions.

For a grating mode to be an eigensolution of Maxwell's equations (ensuring that the symmetry operations are Hermitian), it must match an irreducible representation of the grating point group [94]. The magnetic field profile shown in Figure 4.2a transforms like B_{2u} in the D_{2h} point group [152]. Figure 4.2b shows a normally incident TM-polarized incident plane wave with the same symmetry as the B_1 irreducible representation of the C_{2v}^y point group, where y corresponds to the

D_{2h}	E	C_{2z}	C_{2y}	C_{2x}	i	σ_z	σ_y	σ_x
A_g	1	1	1	1	1	1	1	1
B_{1g}	1	1	-1	-1	1	1	-1	-1
B_{2g}	1	-1	1	-1	1	-1	1	-1
B_{3g}	1	-1	-1	1	1	-1	-1	1
A_u	1	1	1	1	-1	-1	-1	-1
B_{1u}	1	1	-1	-1	-1	-1	1	1
B_{2u}	1	-1	1	-1	-1	1	-1	1
B_{3u}	1	-1	-1	1	-1	1	1	-1

Table 4.1: Character table for the D_{2h} point group at the Γ point.

sole axis with C_2 rotational symmetry. That is, its symmetries are *E* = 1, C_{2y} = -1, σ_z = 1, and σ_x = -1. As described in Reference [152], the B_1 representation of C_{2v}^y maps to B_{1g} and B_{3u} of D_{2h}. Thus, since the first-order mode in Figure 4.2a matches B_{2u}, group theory accurately predicts that this mode is symmetry-protected at normal incidence. By contrast, an obliquely incident TM-polarized plane wave under classical mounting (i.e. $|\theta| > 0$) has only two symmetries: *E* = 1 and σ_z = 1. Consulting Table 4.1 shows that B_{2u} also transforms according to *E* = 1 and σ_z = 1. Thus, relaxing the symmetry condition via oblique incidence allows access to the symmetry-protected BIC.

Similar arguments apply to 2D SWGs, though the larger degree of freedom introduces significantly more symmetries to consider [153]. In both the 1D and 2D cases, the question amounts to whether symmetry-protection causes the coupling coefficient, γ, to vanish.

$$\gamma = \iint_A [E_{inc}^* \times H_{mode} + E_{mode} \times H_{inc}^*] dA \tag{4.1}$$

In Equation 4.1, *inc* and *mode* refer to the incident field and mode field profile, respectively. Rigorous analysis and complete enumeration of selection rules are given in References [152] and [153].

4.2 Two-Step Asymmetric Gratings

4.2.1 Design

Now consider the two-step HCG depicted in Figure 4.3. As before, when the step height, t_{step}, is zero, the grating is rectangular and belongs to the D_{2h} point group. Introducing a nonzero t_{step} reduces the geometry to the C_s^z point group possessing only *E* and σ_z symmetries. Though the modes in the two-step and rectangular HCG are not strictly speaking the same, for small perturbations the modal energy and field profile are minimally affected. For instance, the first order TM

mode in Figure 4.2a qualitatively maintains its two lobe profile for small t_{step} values. However, the two lobes in the two-step HCG are asymmetric, whereas they are antisymmetric in the stable BIC configuration. This particular mode transforms as the A' irreducible representation of C_s^z (*E* = 1 and σ_z = -1), which is the same representation as a TM-polarized normally incident plane wave. Therefore, the two-step HCG enables quasi-BIC coupling at normal incidence. This argument is numerically confirmed in Figure 4.4b, where coupling to the high-Q modes near 8 and 11 µm only occurs for nonzero step heights. Though the two-step geometry in Figure 4.3 is not the only possibility fulfilling these symmetry requirements, it is perhaps the most practical. The binary geometry introduces only one additional patterning step, presenting reasonable lithographic and etching demands.

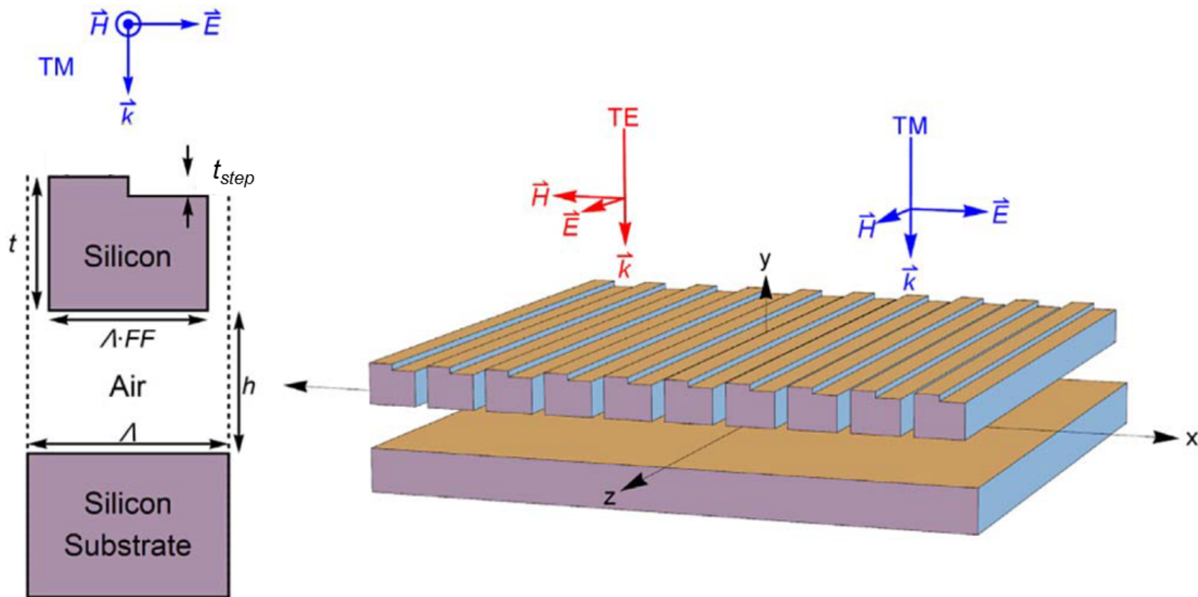

Figure 4.3: Schematic of the two-step asymmetric HCG. Figure referenced from [43].

As expected, the transmittance passbands in Figure 4.4b broaden with increasing step height. This is a predictable consequence of increased radiative decay for more strongly coupled modes. The resonance wavelength also blueshifts with t_s since a reduction in dielectric material raises the modal energy. Figure 4.4c shows the influence of the trench width, w_{step}. The coupling is strongest at $w_{step} = 0.5FF \times \Lambda$. Detuning in either direction heuristically makes the geometry more symmetric since the grating is rectangular at the extrema (w_{step} = 0 and $FF \times \mathit{\Lambda}$).

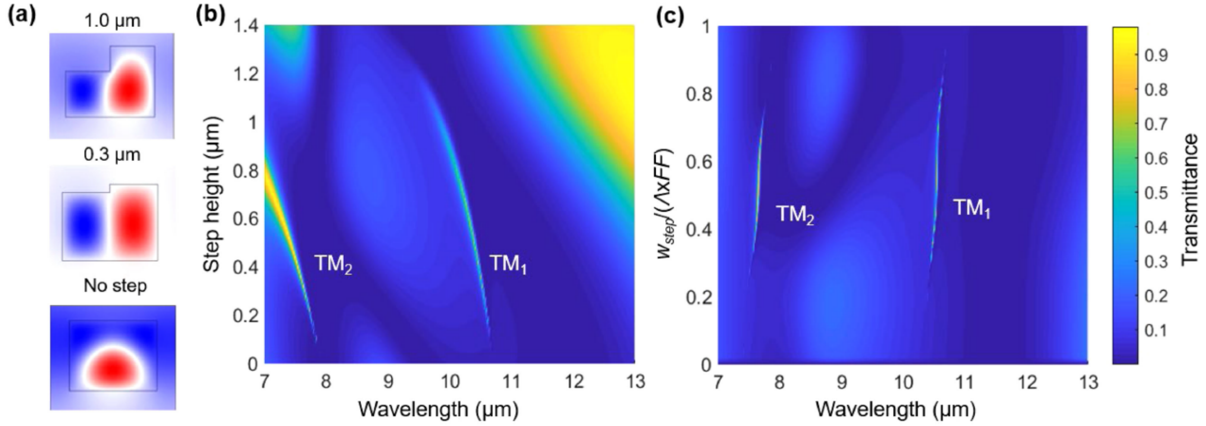

Figure 4.4: a) H-field profiles for a two-step HCG at three representative step heights. (b, c) Simulated transmittance spectra for varying step b) height and c) width. Figure referenced from [15].

4.2.2 Diffraction Efficiency Symmetry

Analysis of diffraction efficiency symmetries provides another, perhaps more intuitive, perspective of stable BICs in SWGs. Figure 4.5a depicts the basic situation, where light diffracted through the ± 1 evanescent diffraction orders excites laterally-propagating guided mode resonances. The magnitude of the E-field contributed by modes excited through the $T_{\pm 1}$ diffraction orders, $E_{T\pm 1}$, is proportional to the coherent interference of the counter-propagating modes

$$E_{T\pm 1} \propto Ae^{-j(\omega t+\beta_1 x)} + Be^{-j(\omega t+\beta_{-1} x)} \tag{4.2}$$

where β_m is the propagation constant for the mode diffracted through order m (m = 1 or -1), and A and B are the diffraction efficiency coefficients of orders 1 and -1, respectively.

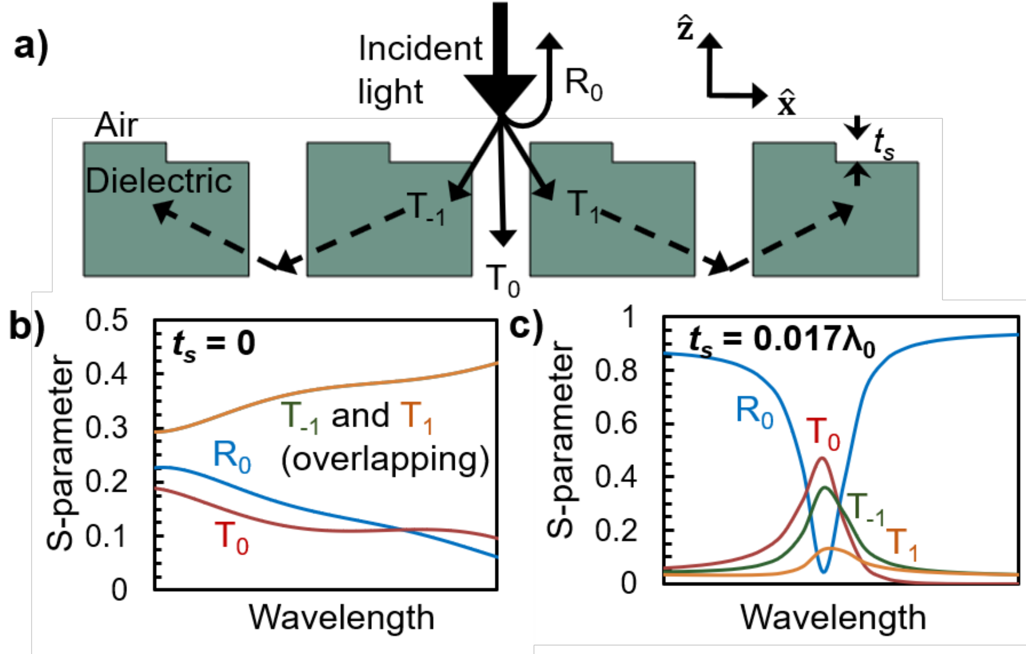

Figure 4.5: a) Diffraction in a two-step HCG. (b, c) Scattering parameters for b) symmetric (t_s = 0) and c) asymmetric (t_s = 0.017λ_0) HCGs at normal incidence. Figure referenced from [70].

For the case of t_s = 0 at normal incidence, *A* = *B* and $|\beta_{-1}| = |\beta_1|$ by inspection. That is, the σ_x symmetry implies that the counter-propagating modes are degenerate. This is reflected by the complete overlap of the T_{-1} and T_1 scattering parameters in Figure 4.5b. Since the two modes propagate in opposite direction, $\beta_{-1} = -\beta_1$, corresponding to a π-phase shift. Thus, Equation 4.2 evaluates to 0 and coupling is prohibited, as indicated by the lack of narrow resonances in Figure 4.5b. With the introduction of a nonzero step height the diffraction efficiency becomes asymmetric and $A \neq B$. In this configuration complete destructive interference cannot be assumed, implying $|E_{T\pm1}|^2 > 0$. Accordingly, the T_{-1} and T_1 scattering parameters in Figure 4.5c are no longer equal, allowing access to the high-Q BIC manifested by the narrow transmittance peak. The preceding analysis does not lead to any conclusions in disagreement with group theory. Rather, it offers an alternative model to understand quasi-BIC coupling in SWGs, later proving useful for achieving polarization-independent access to quasi-BICs.

4.2.3 Fano Analysis

In guided mode resonant SWGs, radiation leaving a quasi-bound mode interferes with non-resonantly scattered light. This interference between two scattering channels, a resonant discrete state and the continuum of non-resonant background states, suggests that the asymmetric features in SWG scattering spectra are Fano resonances [154–156]. Like BICs, Fano resonance is a general wave

phenomenon and was originally formulated to describe certain quantum systems [157]. Reference [156] provides a great introduction to Fano resonance in photonic devices, whereas this section focuses on insight germane to practical SWG filters.

Equation 4.3 describes the general transmittance lineshape for a Fano resonance (T_{Fano}) at the resonant frequency ω_0

$$T_{Fano} = |t_D|^2 \tfrac{(q+\delta)^2}{1+\delta^2} \tag{4.3}$$

where t_D is the non-resonant transmission coefficient ($S_{12} = S_{21}$ of the scattering matrix), q is the asymmetry factor, $\delta = (\omega - \omega_0)/\gamma$ is the reduced frequency, and γ is the total decay rate. In the absence of loss the asymmetry factor is given by

$$q = p\sqrt{4\eta_1\eta_2/|t_D|^2 - 1} \tag{4.4}$$

where η_m is the partial decay probability of the quasi-bound state into port *m* (e.g. resonant transmission or reflection) and *p* is the parity of the mode (1 for even-like and -1 for odd-like) [154]. Figure 4.6 shows the Fano lineshape for three characteristic values of *q*. When *q* approaches infinity the lineshape becomes purely Lorentzian. From Equation 4.4 this occurs when $t_D = 0$, proving that the asymmetry is due to interference with the non-resonant background radiation. When *q* = 0 the spectrum exhibits a symmetric extinction dip. Intermediate values of *q* display the spectral asymmetry characteristic of Fano resonance. The basic Fano lineshape in Equation 4.3 does not account for optical absorption. Using temporal coupled mode theory, Yoon and Magnusson formulated an expression for the lossy Fano resonance ($T(\delta)$),

$$T(\delta) = \eta_{rad} T_{Fano}(\delta) - \beta \tfrac{\eta_{rad}\eta_{abs}}{1+\delta^2} + \eta_{abs}|t_D|^2 \tag{4.5}$$

where η_{rad} is the total radiative probability, η_{abs} is the absorption probability, $\beta = 4\eta_1\eta_2/(\eta_1 + \eta_2)^2$, and $T_{Fano}(\delta)$ is defined in Equation 4.3 [117]. Equation 4.5 may be used to fit empirical or numerical transmittance spectra, yielding useful information about the resonance in the form of the fitting parameters: $\omega_0, \gamma, \eta_1, \eta_2, \eta_{abs}$ and t_D.

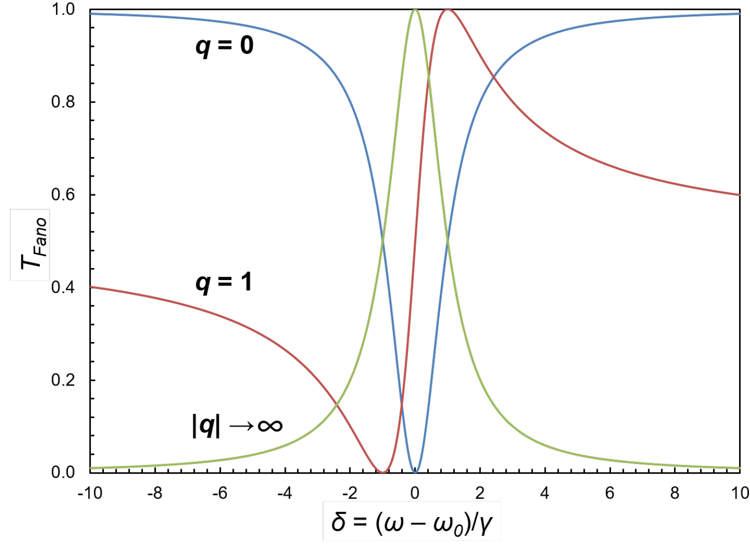

Figure 4.6: Fano lineshape for three values of the asymmetry factor, q.

Fitting Equation 4.5 to numerically calculated transmittance spectra reveals interesting relations between the fitting parameters and the step height of the two-step HCG. Figure 4.7 plots extracted Q and peak transmittance values for two-step HCGs with varying step height. Previously, Q was defined by $\omega_0/\Delta\omega$, where $\Delta\omega$ is the resonance's full width at half maximum linewidth. Figure 4.7, on the other hand, uses the definition $Q = \omega_0/2\gamma$, enabling direct extraction of Q from the fitted curve. The Q-dependence on step height is unsurprising, as it is already established that step height, symmetry breaking, coupling strength, and radiative decay rate are all directly related in stable BICs. The peak transmittance has the opposite relationship to step height and monotonically increases.

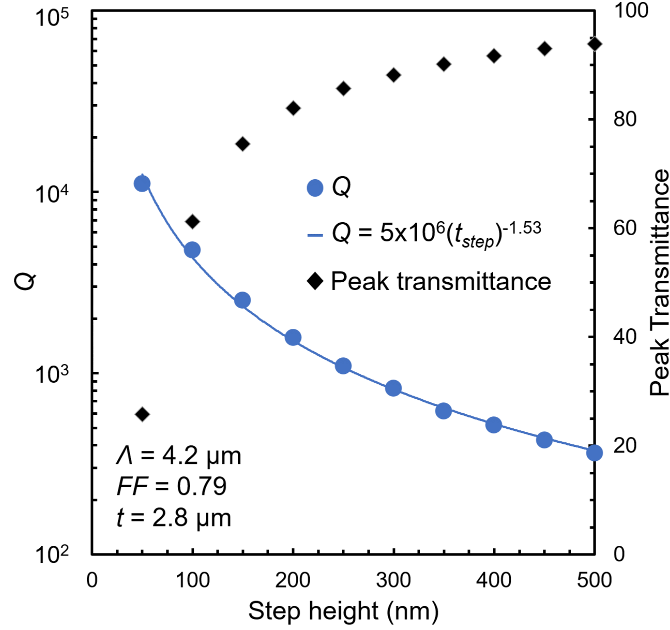

Figure 4.7: Extracted Q and peak transmittance as a function of step height. Equation 4.5 is fit to a numerical transmittance spectra at normal incidence with $\kappa_{Si} = 1 \times 10^{-4}$. Figure referenced from [15].

Figure 4.7 is better understood by considering the total decay rate, γ, and absorption probability, η_{abs}. The step height dependencies in Figure 4.8a are reminiscent of the curves in Figure 4.7. Of course, Q and γ are related by $Q = \omega_0/2\gamma$. It may be less clear to the reader why η_{abs} is strongly dependent on step height. Across the MWIR and LWIR, silicon is highly transparent and minimally dispersive [112]. The extinction coefficient, κ, is the imaginary component of the complex refractive index, $n(\lambda)^* = n(\lambda) + i\kappa(\lambda)$. At λ = 10 μm, κ_{Si} ≈1 $\times 10^{-4}$. The intensity of radiation propagating through a lossy homogeneous medium may be calculated with $I(x) = I_0 exp(-\alpha x)$, where x is the penetration depth and $\alpha = 4\pi\kappa/\lambda$ is the absorption coefficient. For a 2 μm thick slab of silicon at = 10 μm, I(2 μm) = 0.9998I_0, a negligible attenuation. This is clearly not the case in Figure 4.8a where η_{abs} converges to 1 at small step heights. To explain this discrepancy, γ and η_{abs} cannot be assumed to be independent. Larger γ corresponds to faster radiative decay, giving the resonant guided modes less time to laterally propagate within the gratings. At shorter step heights light remains in the gratings longer, giving more opportunity for absorption. Thus, the absorption spectra are also resonantly enhanced. The peak transmittance and η_{abs} are directly related by energy conservation: $T_{peak} = 1 - R_{peak} - \eta_{abs}$, where R_{peak} is 0 at a true pole in the transmittance spectrum.

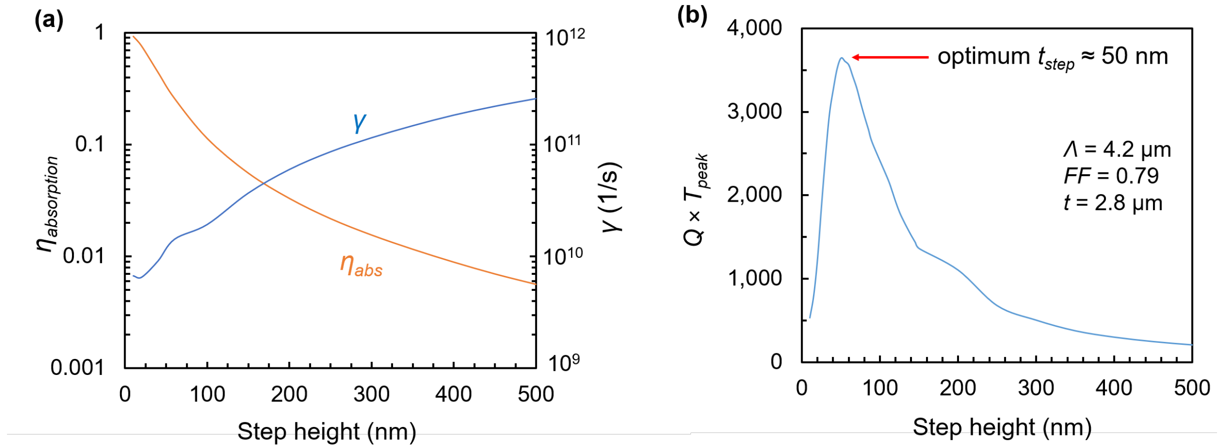

Figure 4.8: a) Relationship between the total decay rate, γ, and the absorption probability, η_{abs} as a function of step height. b) Step height optimization via an ad hoc figure of merit, $Q \times T_{peak}$. Figure referenced from [15].

The relationship between γ and η_{abs} presents a practical trade-off between Q and T_{peak}. In the absence of loss, arbitrarily small step heights lead to indefinitely large Q factors. Prior studies on symmetry-protected modes in SWGs only consider the influence of the non-radiative decay rate, γ_{nr}, on Q [99, 100]. Non-radiative losses place an upper bound on the total achievable Q via $1/Q_{tot} = 1/Q_{rad} + 1/Q_{nr}$. However, as was shown in Figures 4.7 and 4.8a, the transmittance peak rapidly diminishes as t_{step} approaches zero. A clear trade-off emerges. The peak linewidth cannot be made arbitrarily narrow without adversely impacting the filter transmission efficiency. In Figure 4.8b an ad hoc figure of merit (FOM = $Q \times T_{peak}$) optimizes the step height. For this particular geometry, the optimum step height is $\approx$ 50 nm, which is $\approx$2% of the total grating thickness. Interestingly, t_{step} = 50 nm corresponds to η_{abs} = 0.35, which is not too far from the critical coupling point ($\eta_{rad} = \eta_{abs}$) occurring at t_{step} = 36 nm. The critical coupling condition is a central principle in the design of perfect absorbers using low-loss materials [158, 159]. Highly symmetric structures like HCGs are fundamentally limited to 50% absorbance even when $\eta_{abs} >$ 0.5.

As shown in Figure 4.9, Fano resonance analysis also reveals the emergence of nonreciprocity in resonant, lossy gratings. The y-axis gives the ratio between the radiation probabilities for ports 1 and 2. Asymmetry across the *xy*-plane leads to $\eta_1 \neq \eta_2$. As shown in the inset, the absorption (and reflection, not shown) spectra become non-reciprocal. The peak absorbance is expressed by Equation 4.6 [154]. Though transmittance is still reciprocal, absorbance and reflectance are dependent on which port is illuminated in an asymmetric structure. This is an important consideration for absorbance and reflectance mode resonant SWGs. In the presence of loss, Figure 4.9 shows that the two-step grating perturbation can induce large nonreciprocity.

$$A_n(\delta) = \frac{4\eta_{nr}\eta n}{1+\delta^2} \tag{4.6}$$

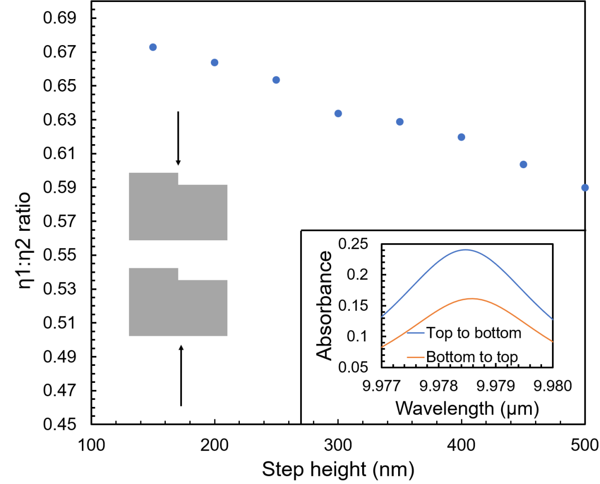

Figure 4.9: Ratio of the radiation probabilities for ports 1 and 2 for varying step heights. (inset) Absorbance spectra near resonance for light incident from above and below the gratings.

4.2.4 Experimental Two-Step HCGs

Reference [43] presents an early experimental demonstration of BIC access in geometrically asymmetric SWGs. Two-step HCGs are optimized for LWIR transmittance filtering, with thickness, t = 2.8 μm and consisting of an array of periods, Λ = [4-5] μm and fill factors, FF = [0.70-0.86]. The filters are designed to operate under TM-polarization. Employing the Si/air material system, the experimental methods closely follow the outline in Section II.4 with an additional patterning and dry etch step to define the two-step structure. Figure 4.10 shows an SEM image of a cross-sectioned Si two-step HCG. Though the designed step width is $\Lambda \times FF/2$, the actual value is somewhat lower.

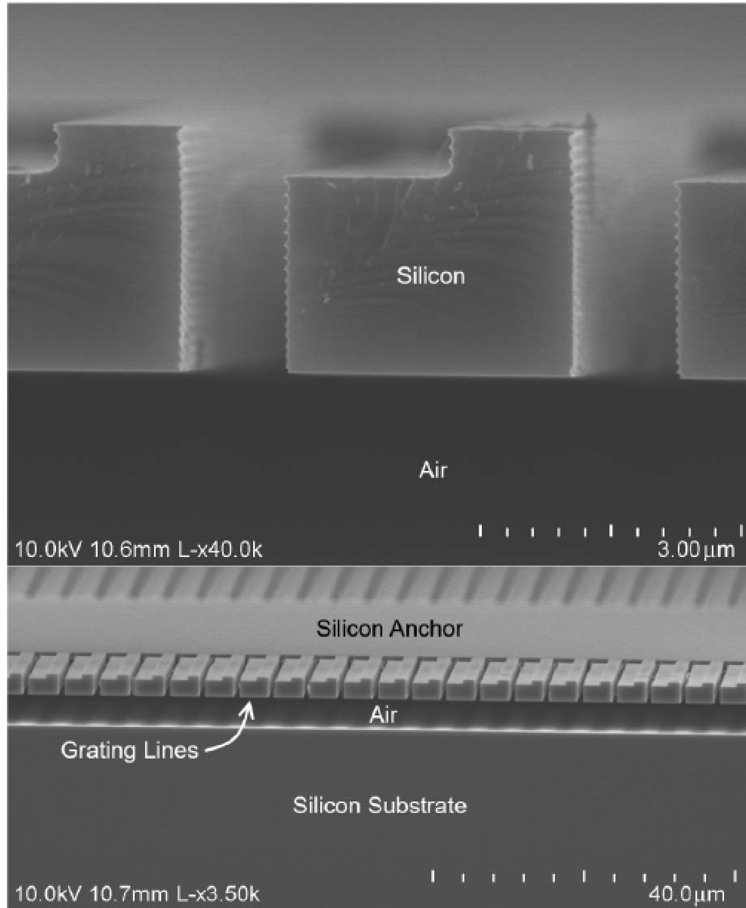

Figure 4.10: SEM images of a cross-sectioned silicon two-step HCG. Figure referenced from [43].

Figure 4.11a compares measured and simulated transmittance spectra and Figure 4.11b confirms the ease of tuning the filter by adjusting the grating period. Though there is reasonable agreement to simulation, the experimental peaks have significantly lower transmittance and broader linewidth. Several non-idealities are responsible for this disagreement, including fabrication process variations, sidewall scalloping, SOI device layer thickness variation, and finite periodicity effects. Due to the non-ideal range of angles in the FTIR setup, the apparent filter performance is closely tied to the optical setup. If the measurements permit a large numerical aperture (NA) then a large range of incident angles impinge on the filters (NA = $n \cdot \sin(\theta)$, where n is the refractive index of the incident medium and θ is the maximal half angle of the cone of light incident on the gratings). Large NA excitation lowers Q via increased BIC coupling and mode dispersion. For the measured transmittance spectrum in Figure 4.12, light is incident from an approximately 0-5° cone of incident angles, corresponding to NA = 0.087 in air. Temporarily discounting other non-idealities, numerically calculated transmittance spectra indicate a maximum Q of $\approx$500. Due to strong leaky mode coupling at oblique angles of incidence, this value is mostly due to strong

radiative coupling. The grating with the smallest step height in Figure 4.12 (t_{step} = 16 nm) has a measured Q of 70. Thus, experimental non-idealities restrict the achievable Q to $\approx$81.

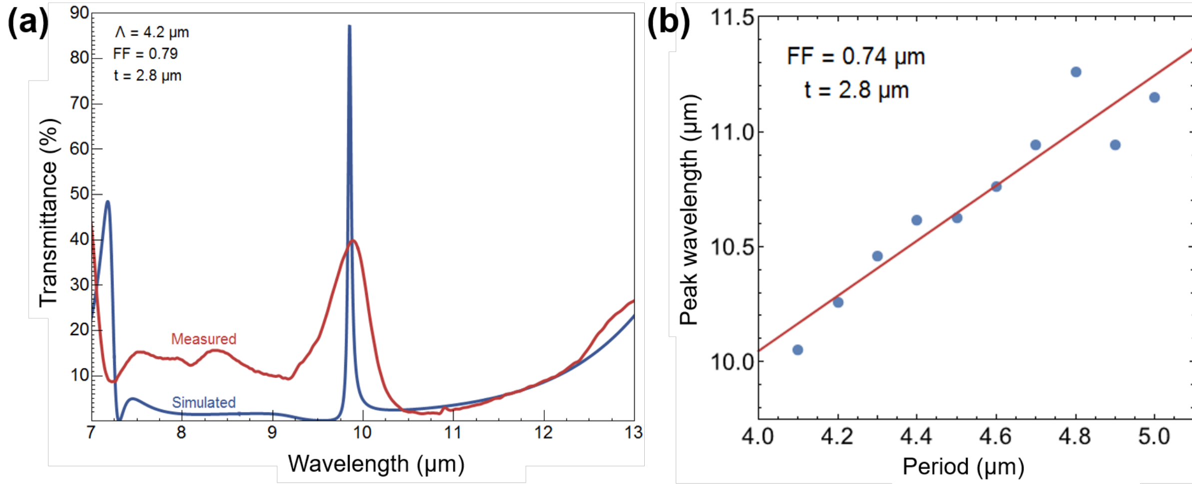

Figure 4.11: a) Comparison of measured and simulated transmittance spectra. b) Peak wavelength tuning by lithographically varying the grating period. Figure referenced from [43].

To determine the influence of step height on filter performance, four sets of two-step HCGs were fabricated with t_{step} values of 16, 60, 140, 500 nm. Though the large NA of the FTIR characterization precludes definitive proof of normal incidence BIC coupling, the experimental structures demonstrate the expected relationship between Q and t_{step}, showing that coupling strength increases with step height. The Q of the 500 nm filter is significantly lower than the filter with a 140 nm step height. This is consistent with increased radiative decay in highly asymmetric HCGs. The experimental dependence of Q on t_{step} is much lower for the three shorter step heights. This is primarily a consequence of the FTIR setup's large NA, since strong radiative coupling due to symmetry-breaking at oblique-incidence sets an upper bound on the purely radiative Q. While the cone of incident angles obscures the signal for low values of t_{step}, this study demonstrates symmetry-relaxation for BICs in an asymmetric two-step HCG.

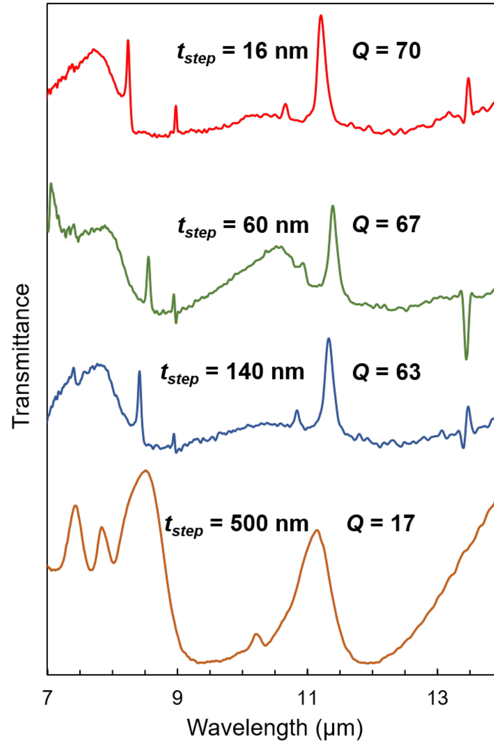

Figure 4.12: Measured transmittance spectra of two-step HCG with varying step heights. Figure referenced from [15].

4.3 Reduced Symmetry Hexagonal Gratings

The asymmetric 1D gratings in the preceding section are strongly polarization-dependent. For applications with an arbitrary polarization state, finding a geometry that permits polarization-independent BIC access is critical. At first glance, the 2D polarization-independent filters in Chapter II.6 may appear to fit the bill. However, the mode responsible for the narrow transmittance peak is a leaky bright mode. These modes occupy the upper bands at the high symmetry points in the SWG reciprocal lattice [68]. The mode symmetries are compatible with a normally incident plane wave, yielding intrinsically low Q values with little room for design (as opposed to stable BIC access via controlled symmetry-breaking). Many studies on polarization-independent SWGs target these symmetric bright modes [22, 32, 35, 39, 68, 115]. Other structures provide polarization-independent access to BICs, but of the accidental variety. These configurations require tight control of the geometric parameters and incident light conditions [32, 116]. Along this line, other works seek quasi-polarization-independence using careful design to achieve degenerate optical response for orthogonal polarizations [20, 38, 160]. The structures presented in this section enable truly polarization-independent access to symmetry-protected BICs, surmounting the limitations of pre-

vious work by relaxing strict design rules and fabrication tolerances.

4.3.1 Reduced Symmetry Square Grating

In some sense, polarization-independent BIC access presents conflicting goals, as stable BIC access prompts symmetry-relaxation while polarization-independence requires symmetry-preservation. The path to polarization-independent BIC access begins by considering the diffraction efficiency symmetry analysis in Section 2. The two-step 1D SWG induces asymmetric diffraction, preventing the complete destructive interference of pairs of modes evanescently coupled through diffraction orders of the opposite sign. It was shown in Chapter II.6 that SWGs with a $\leq \pi/2$ rotational symmetry are inherently polarization-independent [114]. The task, then, is to engineer asymmetric diffraction for each diffraction order pair (e.g. ± 1) at normal incidence. If the dielectric function is identical along orthogonal diffraction directions (e.g. $T_{\pm 1,0}$ and $T_{0,\pm 1}$), degenerate BICs may be simultaneously excited, allowing polarization-independent BIC access.

An illustration of this concept is shown in Figure 4.13a for a 2D square array. The figure shows the unit cell of a 2D square grating from the top-down view. By symmetrically perturbing one corner of a square pillar, the grating symmetry is reduced to the C_s point group at the Γ point. The $\eta_{m,n}$ parameter signifies the diffraction efficiency of order *m,n*. By inspection, $\eta_{0,1} = \eta_{1,0}$, $\eta_{0,-1} = \eta_{-1,0}$, and $\eta_{0,1} \neq \eta_{1,0}$. The asymmetric C_s grating induces asymmetric diffraction in two orthogonal directions. Accordingly, Figure 4.13b shows a sharp transmittance peak for the asymmetric grating, while the symmetric square-shaped grating predictably does not exhibit any high-*Q* resonances. Given the grating symmetry, it is clear that modes propagating along the *x*- and *y*-axes will have the same propagation constant. While analyzing diffraction efficiency symmetries reveals this insight, it is still unclear whether the structure in Figure 4.13 is fully polarization-independent.

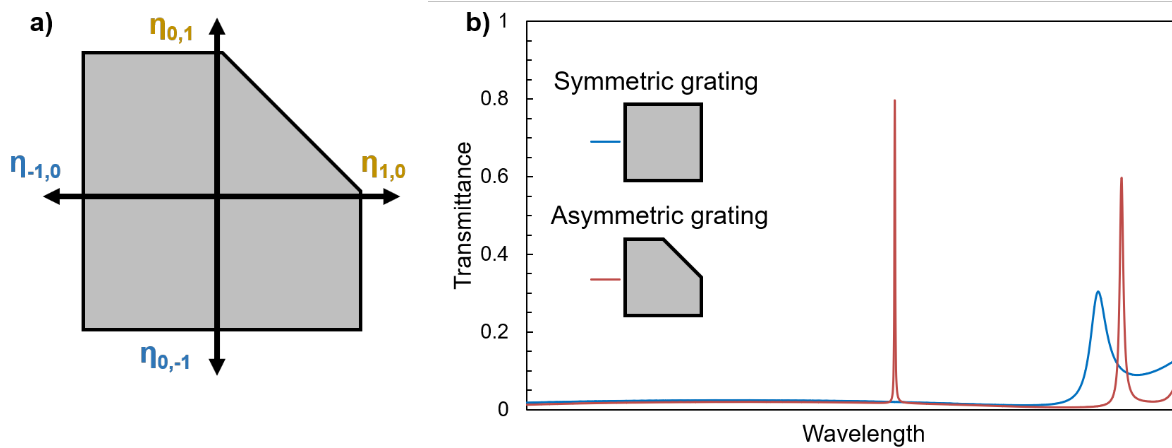

Figure 4.13: a) Unit cell of the C_s symmetry square lattice SWG. b) Simulated transmittance spectra of symmetric and asymmetric (C_s) square lattice SWGs.

Figure 4.14a defines the polarization angle, p, for light normally incident upon the square lattice gratings. Four high-symmetry angles are considered (p = 0, 45, 90, and 135°). The p = 0 and 90° linear polarization states correspond to the orthogonal directions indicated in Figure 4.13a (double-sided black arrows). Figure 4.14b shows that the 0° and 90° polarizations are fully degenerate but limited to $< 50\%$ transmission efficiency. In contrast, the 45 and 135° states are strongly polarization-dependent, as the 45° polarization is still symmetry-protected. The 0 and 90° states are thus a linear combination of p = 45° and 135°. The 135° state fully accesses the BIC since the propagating light alternates between "seeing" a corner and a notch. Diffraction is asymmetric along this direction. In the 45° direction, light only encounters corners and diffraction is symmetric.

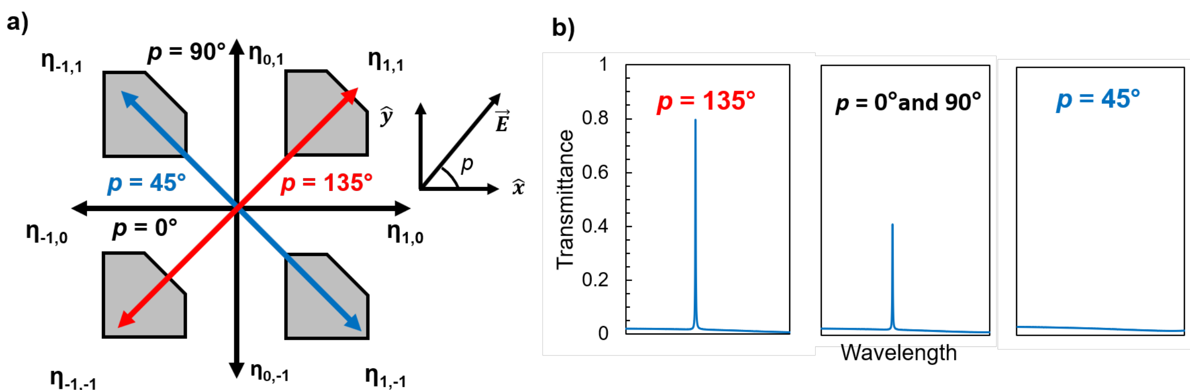

Figure 4.14: a) Definition of polarization directions in the C_s symmetry square lattice SWG. b) Simulated transmittance spectra for three high-symmetry polarization states.

4.3.2 Reduced Symmetry Hexagonal Grating

The hexagonal lattice SWG is next evaluated as a platform for polarization-independent BIC coupling. Figure 4.15 shows a schematic of the proposed design. In the reduced symmetry hexagonal grating, a hexagonal lattice of circular holes are patterned into a homogeneous slab. The unit cell is then perturbed every 120° by an amount *a*, as shown in Figure 4.15b. After perturbation, the unit cell belongs to the same symmetry group as an equilateral triangle.

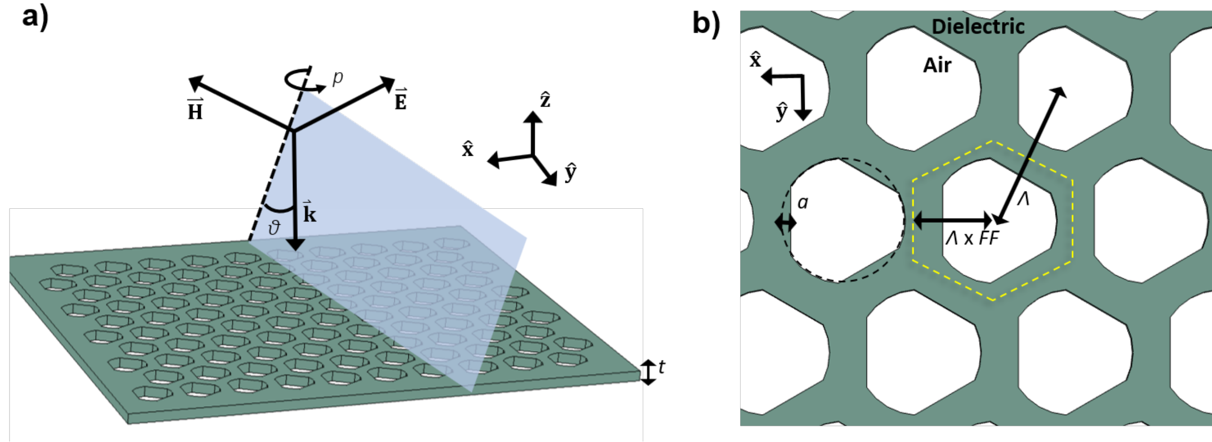

Figure 4.15: Schematic of the reduced symmetry hexagonal grating from a) perspective and b) top-down viewpoints. The E-field is parallel to the plane of incidence in the "in-plane" polarization state. The parameter *p* is the polarization angle. Figure referenced from [70].

Simulated transmittance spectra are shown in Figure 4.16a for varying values of the asymmetry parameter, *a*. The refractive index of the dielectric is chosen to be 3.29, which similar to GaAs in the IR [122]. For $a > 0$ a narrow transmittance peak appears near $\lambda = 1.25\Lambda$ and monotonically broadens with *a*, a clear signature of a symmetry-protected BIC. The spectra in Figure 4.16a are fully polarization-independent (not shown since spectra completely overlap). Figure 4.16b shows the simulated transmittance spectra for $a = 0.006\Lambda$ with an extracted *Q* of 8400. Though this slight degree of asymmetry is impractical for most lithography systems, larger values of *a* are equally valid with a proportional drop in *Q*. A small value for *a* is used in Figure 4.16 to give an illustrative comparison to the symmetric (*a* = 0) grating. Greater asymmetries distort the grating and require re-optimized parameters. The field profile in the inset reveals that the polarization-independent symmetry-protected mode belongs to the TM-mode E_2 irreducible representation of the C_{6v} hexagonal point group. Using group theoretical analysis, Overvig et al. independently proposed this same mode for polarization-independent BIC access [153].

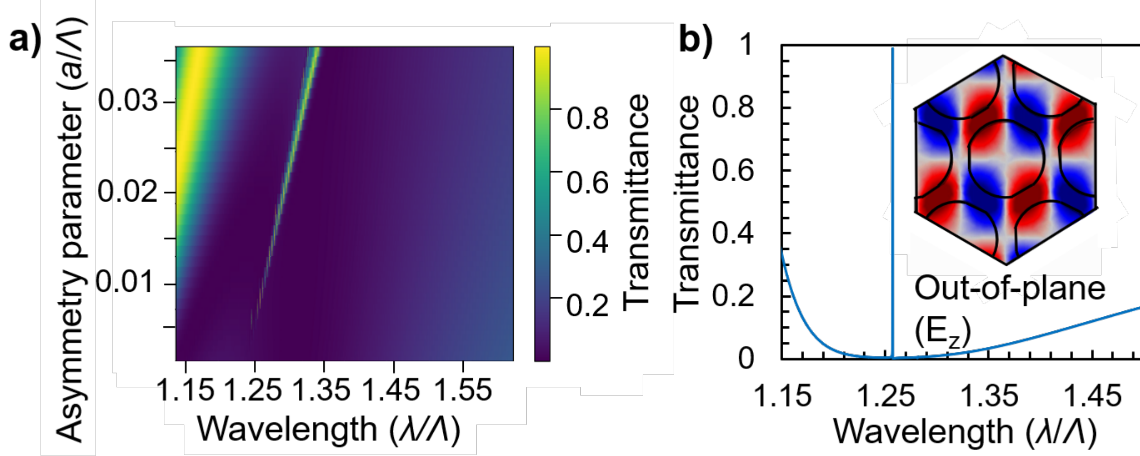

Figure 4.16: a) Simulated transmittance spectra as a function of the asymmetry parameter, *a*, at normal incidence. b) Normal incidence transmittance spectrum for the parameters *FF* = 0.826, *t* = 0.224Λ, and *a* = 0.006Λ. The inset shows the out-of-plane E-field profile at the λ = 1.26Λ resonance. Figure referenced from [70].

By perturbing the unit cell every 120°, asymmetric diffraction occurs for the three diffraction pairs depicted in Figure 4.17a. The unperturbed hexagonal lattice possesses C_6 rotational symmetry which is reduced to C_3 when $a > 0$. Figure 4.17a also defines the polarization angle, *p*. For the hypothesis of the diffraction efficiency analysis to be upheld, asymmetric diffraction must occur in each pair. The dispersive scattering parameters given in Figure 4.17b provide a useful stand-in for direct diffraction efficiency calculation. To estimate diffraction efficiencies, a listener port is placed in close proximity to the gratings and couples in the near field to the evanescent diffraction orders. Though the port interferes with the grating modes, the symmetries are maintained. Figure 4.17b shows asymmetric diffraction within the three groups of diffraction pairs: T_{01} and T_{0-1}, T_{-10} and T_{10}, T_{11} and T_{-1-1}.

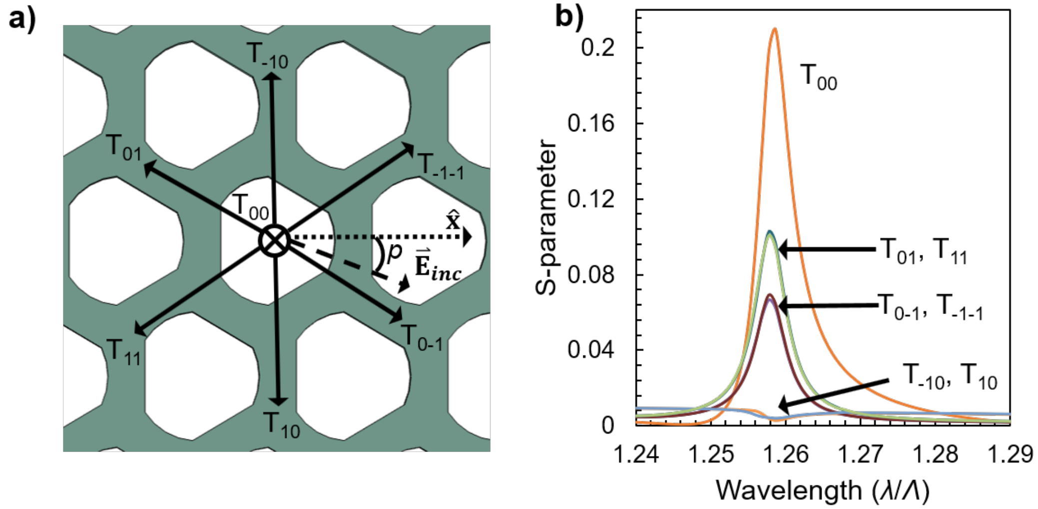

Figure 4.17: a) Reduced symmetry hexagonal grating schematic with definition of first-order diffraction vectors and polarization angle, p. b) Simulated out-of-plane scattering parameters at normal incidence and $p = 0°$. The grating parameters are $FF = 0.826$, $t = 0.22\Lambda$, and $a = 0.015\Lambda$. Figure referenced from [70].

A fuller picture is obtained by sweeping the polarization angle in a full 2π rotation and observing the diffraction efficiencies. In the symmetric grating the diffraction pairs remain completely degenerate for every polarization angle as shown in Figure 4.18a. This is expected as circular holes yield symmetric diffraction. As p rotates, the efficiency of each diffraction pair possesses 2π periodicity. The pairs are phase shifted by a predictable $\pm 2\pi/3$ with respect to each other. In the reduced symmetry grating in Figure 4.18b, the two efficiencies within each pair experience a phase shift. Diffraction efficiency is asymmetric with the exception of certain high-symmetry polarizations, such as T_{-10} and T_{10} at $p = \pi/2$. At the high-symmetry polarizations, the two remaining asymmetric pairs are at their largest degree of asymmetry. Thus, as one pair loses energy, the other two perfectly compensate. In true polarization-independent fashion, the relationship $T_{-10} + T_{0-1} + T_{11} = T_{10} + T_{01} + T_{-1-1}$ is upheld for every value of p. Given the grating's symmetry, the BIC is degenerate regardless of which diffraction order it is excited through. This is an interesting result since the grating is polarization-independent despite only possessing a C_3 rotational symmetry. In one sense the grating is polarization-dependent, as shown in Figures 4.16b and 4.17b, but it is actually the combined response of the the three diffraction pairs that is polarization-independent.

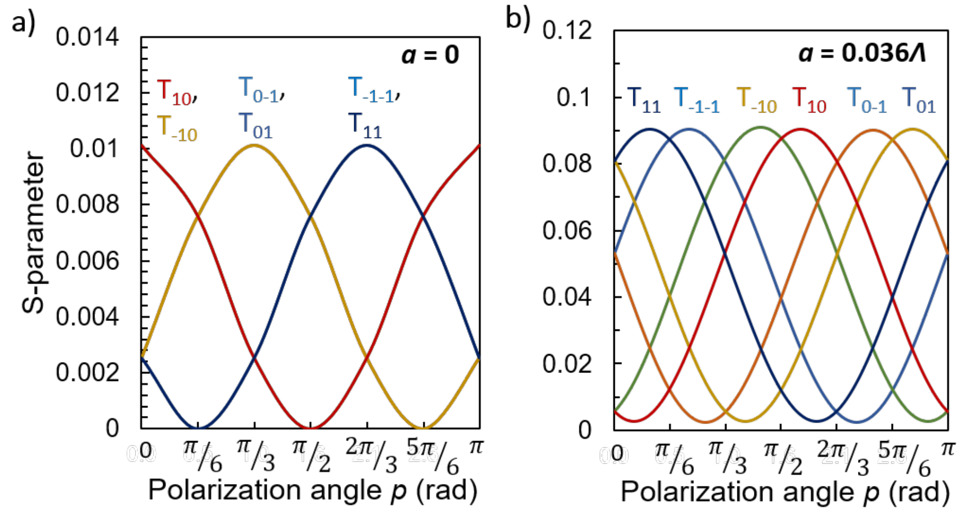

Figure 4.18: Dependence of scattering parameters on polarization angle for the a) symmetric and b) reduced symmetry hexagonal SWGs at the 1.26Λ resonance. The *FF* and *t* values are the same as in Figure 4.17. Figure referenced from [70].

CHAPTER 5

Emission and Propagation of Infrared Light in Subcranial Tissue

5.1 Introduction

As neural interfaces approach sub-mm dimensions, the optimal power source remains an open question [83]. Percutaneous wires cause infection and limit mobility. Battery-powered devices are safer, but have limited lifetime, require invasive surgery to replace depleted batteries, and have large form factor [161]. Harvesting environmental energy (e.g. heat, motion, chemical potential) is an interesting option, though present technologies cannot supply enough power for neural interfaces.

To overcome these limitations, several wireless modalities have been investigated. Inductive coupling via near-field RF radiation offers large channel counts and high power transfer efficiency (PTE) at mm-dimensions [78, 79]. The PTE is dependent on coil size, distance, and alignment, rapidly diminishing as the coils scale to sub-mm dimensions [162, 163]. The calculated PTE for a 10 mm^2 mote area is 23%, which decreases to 0.036% and 5.98µ% for 1 mm^2 and 0.1 mm^2 areas, respectively [83]. Moreover, smaller coils increase the optimal PTE frequency. In tissue, power attenuation worsens with frequency, raising heating concerns. Ultrasonic (US) power is also proposed for sub-mm implants [80, 164–166]. Slow propagation velocity imbues US waves with much shorter wavelengths than electromagnetic waves, allowing dramatically higher PTE, particularly for large implantation depths. Still, US power suffers drawbacks of its own, including high attenuation in bone. Bulky US transducers are difficult to scale to sub-mm dimensions and vertically integrate with CMOS circuitry. In US neural implants, data uplink is furnished via amplitude-modulated backscattering. This passive communication scheme requires external interrogation. For large numbers of motes this requires precise beamforming by the interrogator, degrading alignment tolerance and data bandwidth.

A third option uses near-infrared (NIR) light, taking advantage of a high-transparency window in biological tissue [81, 167]. Photovoltaic (PV) cells generate electrical power from an incident

radiation source, such as an LED, laser, or ambient light. Like the RF electromagnetic link, NIR power transfer is primarily limited by safe tissue heating limits. The central question is whether a given implant size can harvest enough power without exceeding safe tissue heating guidelines. Previous work in NIR powered neural recorders [168] and sub-mm sensors [82] assume intensity limits exceeding 200 mW/mm^2, though this assumption is based on highly localized multiphoton microscopy experiments [169]. Irradiation over a centimeter-scale area would likely cause dangerous heating, as the recommended exposure limit is 1.36 mW/mm^2 based on a 1-2°C temperature increase [170]. Clearly, designing a high efficiency NIR link is an urgent task.

Reference [84] uses a dual-wavelength NIR link for wireless power and data transfer. The implanted neural dust motes are powered by a dual-junction PV cell [85, 171] irradiated by an external source with a 850 nm central wavelength. An on-chip 1000 nm µLED relays detected neural activity to a subcranial repeater unit. The mote is implanted above the pia but beneath the dura, as shown in Figure 5.1. Preservation of the dura mater is imperative to long-term subject health, as this thick connective tissue serves several important anatomical roles. Consequently, photons emitted from implanted motes must propagate through the dura before reaching the repeater.

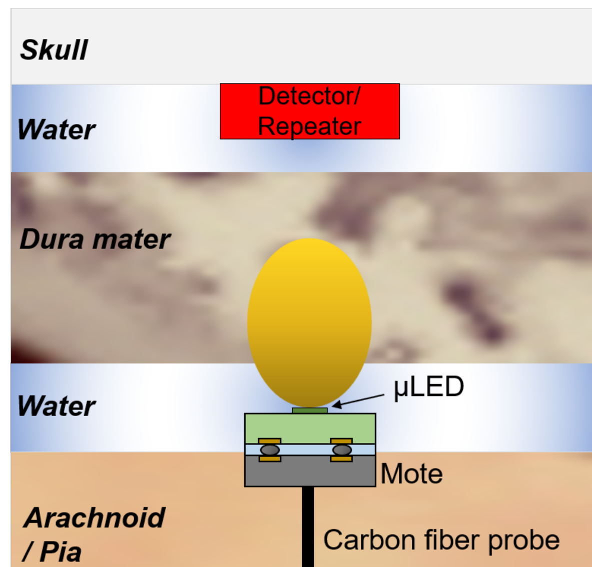

Figure 5.1: Optical beam path between an implanted mote and the detector/repeater unit.

Compared to electronics-grade materials, biological tissue is far less homogeneous. The size, orientation, and positioning of optical defects are somewhat randomly distributed. Different bodily tissues scatter light with varying degree of anisotropy [81, 172, 173]. The optical path from an embedded LED to a detector is therefore complicated and dependent on local tissue conditions. To account for this random scattering, Monte Carlo simulations are performed using an open source turbid material simulator (MCML) [174]. The following section models the beam path depicted in

Figure 5.1. Section 3 characterizes the experimental optical setup for µLED measurements.

5.2 Monte Carlo Simulations of NIR Propagation in Tissue

5.2.1 Model Details

MCML [175] constructs a light propagation model using five parameters for each material layer: layer thickness, *t*, refractive index, *n*, absorption coefficient, μ_α, scattering coefficient, μ_s, and anisotropy coefficient, g. The simulation domain is divided into a user-defined mesh, as illustrated in Figure 5.2, with an infinitely narrow photon beam normally incident upon the tissue stack. When a photon enters the next meshed element, it may be absorbed with a probability commensurate to μ_α and the element size. Similarly, μ_s determines the probability of a change in propagation direction. If g = +1(-1), scattering is fully forward(backward), while g = 0 corresponds to complete isotropy. In tissue, g typically ranges from 0.3-0.98. Scattered photons are deflected at an angle chosen from a g-dependent probability distribution. The deflection angle, θ is calculated by:

$$cos(\theta) = \begin{cases} \frac{1}{2g}\{1 + g^2 - [\frac{1-g^2}{1-g+2g\xi}]^2\} & \text{if } g \neq 0 \\ 2\xi - 1 & \text{if } g = 0 \end{cases} \tag{5.1}$$

where ξ is a random number ($0 < \xi < 1$). The azimuthal angle, ϕ, is randomly chosen according to $2\pi\xi$. The model accounts for specular reflections via input *n* values:

$$R = \frac{(n_1-n_2)^2}{(n_1+n_2)^2} \tag{5.2}$$

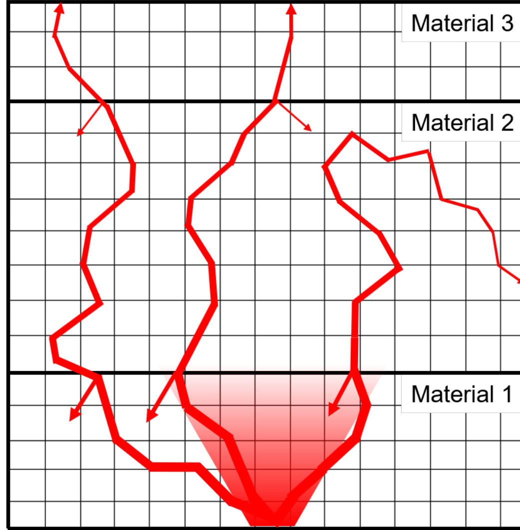

Figure 5.2: Illustration of example photon paths (not simulated). Figure displays the three scattering events: absorption, anisotropic defect scattering, and specular reflection at material interfaces.

Two scored physical quantities are of chief interest: transmittance and fluence. A launched photon begins with a weight, *W*. When a photon enters a new grid element a portion of the weight is deposited in the element according to $\Delta W = W\mu_a/(\mu_\alpha + \mu_s)$. After launching the full set of photons, the accumulated weight gives the absorption distribution, which is convertible to fluence by W/μ_α. A launched photon can terminate by falling beneath a threshold weight or encountering a boundary and leaving the tissue. When a photon encounters a boundary, it deposits its weight into the adjacent grid element, giving a transmission(reflection) distribution at the top(bottom) boundary. Extracted fluence and transmission distributions are useful for calculating the NIR PTE.

5.2.2 NIR Link Efficiency

Passive neural recording is but one of the arenas driving the development of wireless neural technology. Devices capable of high-fidelity recording and wireless signal transmission inspire great promise toward reestablishing severed nervous connections. For instance, NIR-powered motes may synthetically reconnect damaged spinal cords [75]. To estimate the efficiency of a NIR link in the spinal column, Monte Carlo simulations are performed for propagation through cerebrospinal fluid (CSF). This simple model provides initial insight before studying propagation through the complex stack in Figure 5.1. The optical properties of CSF are sourced from Reference [167] and are listed in Figure 5.3a. Figure 5.3a plots the fluence distribution at λ = 1000 nm. A 200 µm wide detector (labeled SPAD in the figure) is positioned directly above the photon source (labeled LED). At a 2.5 µm distance, the link efficiency between the LED and the SPAD (η_{link}) is $\approx 0.1\%$.

That is, 0.1% of the emitted photons are transmitted at the boundary where the 200 μm diameter detector would be.

The link efficiency is strongly dependent on the detector distance, d_{SPAD}. Figure 5.3b plots the relationship between η_{link} on d_{SPAD}. Shortening d_{SPAD} from 4 mm to 2 mm boosts η_{link} from 0.038% to 0.16%, a fourfold increase. Since CSF is 99% water it very weakly scatters light, as reflected by its low empirical scattering coefficients (μ_α = 0.04 cm^{-1} and μ_s = 1 cm^{-1}). Thus, the approximately quadratic relationship in Figure 5.3b is chiefly a geometric effect. Even slightly isotropic scattering (i.e. $|g| \neq 1$ and $\mu_s > 0$) significantly lowers η_{link} at large distances. At 2.5 mm, a deflection of only 1.1° will cause the photon to miss the detector. The situation is even worse for realistic angular emission profiles, such as the Lambertian distribution where the emission intensity is proportional to the cosine of the emission angle. Light emitted at an oblique angle is even less likely to reach the detector, especially for highly tangential configurations like the one in Figure 5.3a.

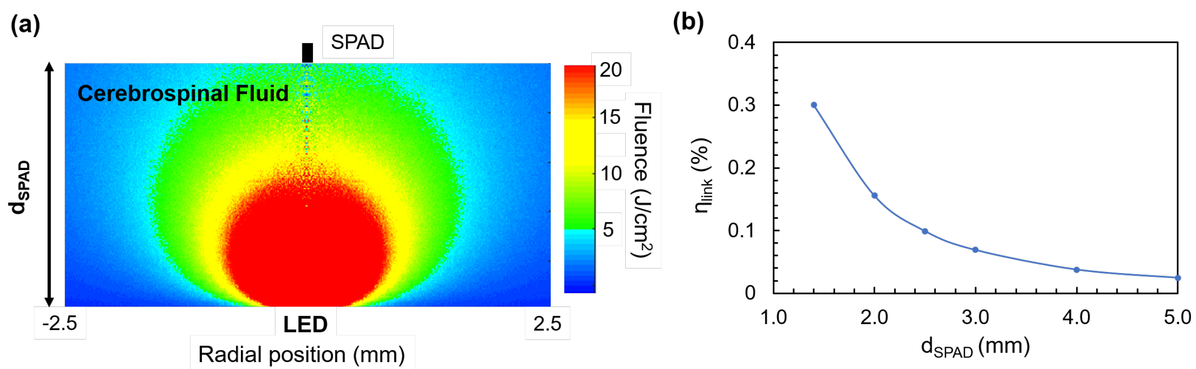

Figure 5.3: (a) Monte Carlo simulation of propagation through cerebrospinal fluid at λ = 1000 nm. The optical parameters are n = 1.4, μ_α = 0.04 cm^{-1}, μ_s = 1 cm^{-1}, and g = 0.89. (b) Link efficiency for varying detector distance.

To evaluate realistic operating conditions for motes implanted in the brain, the model simulates a 1 mm layer of human cerebral dura mater sandwiched between two 0.2 mm films of water [176]. Optical parameters are sourced from previous empirical studies at λ = 1 μm [81, 167]. Incomplete NIR data requires extrapolation and rational guesses at realistic parameters. The optical parameters for dura(water) are n = 1.4(1.32), μ_α = 0.8(0.04) cm^{-1}, μ_s = (45)(0) cm^{-1}, and g = 0.75(1). Roughly 1e7 test photons are needed for statistical convergence. Figure 5.4 shows the fluence plot of a 1 μm LED aligned to a 200 μm diameter detector. Compared to the CSF study in Figure 5.3, modeling propagation in the multilayer water/dura/water stack introduces several additional considerations. Since water and dura have similar optical density, Equation 5.2 indicates that only 0.09% of the incident power is reflected at the water/dura interfaces. Dura absorbs and scatters light much more

strongly than CSF. Thus, at a 1.4 mm detector distance, η_{link} is only 0.1% compared to 0.3% in CSF. In addition to increased absorptive loss, light propagating through dura is more likely to scatter and is deflected with a more isotropic angular distribution, lowering the probability of reaching the detector. Table 5.1 shows the dependence of η_{link} on the dura optical parameters, demonstrating the expected degradation for increased scattering, absorption, and deflection isotropy.

η_{link} (%)	μ_s (cm^{-1})	μ_α (cm^{-1})	g
0.102	45	0.8	0.75
0.075	**100**	0.8	0.75
0.137	**10**	0.8	0.75
0.060	45	**0**	0.75
0.088	45	**1.6**	0.75
0.117	45	0.8	**0.85**
0.188	45	0.8	**0.65**

Table 5.1: Influence of the dura optical parameters on link efficiency at λ = 1000 nm. The layer thicknesses, optical parameters of water, and dura refractive index are all fixed.

The detector sensitivity S_{det} (optical power required to register a data pulse), η_{link}, and the LED's external quantum efficiency (EQE_{LED}) are sufficient to calculate the electrical energy required to register an optical pulse (P_{pulse}) from the LED:

$$E_{pulse} = S_{det}/(\eta_{link} \cdot EQE_{LED}) \tag{5.3}$$

As an example, if the detector's pulse detection limit is 50 photons/pulse (for λ = 1000 nm), η_{link} = 0.1%, and $EQE_{LED} = 2.5\%$, the system must supply the LED with 189 fJ/pulse. The following section gives a more thorough treatment of pulse detection efficiency.

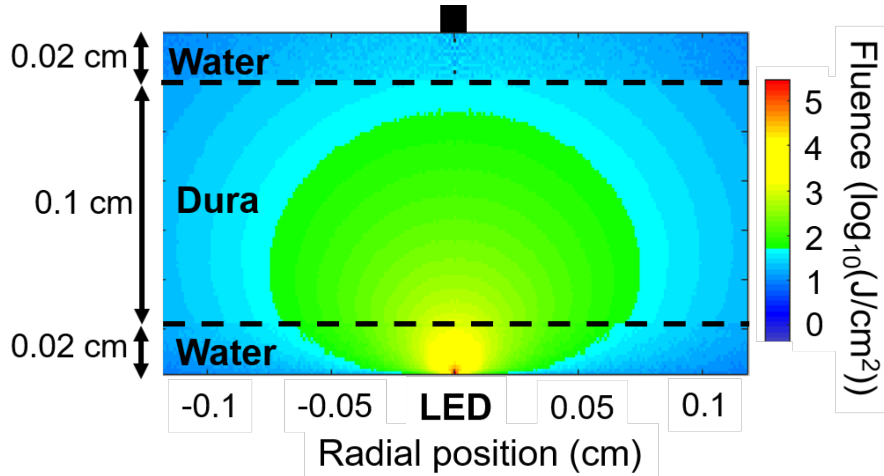

Figure 5.4: Monte Carlo simulation of NIR propagation through dura mater at λ = 1000 m. The dura optical parameters are n = 1.4, μ_α = 0.8 cm^{-1}, μ_s = 45 cm^{-1}, and g = 0.75.

5.3 Experimental Pulse Detection

5.3.1 Experimental Setup

Reliable photon detection is vital, as poor light collection may negate even the most exemplary neural recorder designs. The overarching wireless neural dust project includes two phases of optical testing. First, pulses must be reliably detected from a single neural dust mote under realistic operating conditions. Then, after validating single-unit performance, another setup detects an array of simultaneously pulsing units. Given the weak LED signal, the system requires extremely reliable detection efficiency. When operated in Geiger mode, single-photon avalanche diodes (SPAD) offer exceptional quantum efficiency with sub-kilohertz dark count. AUREA Technology's thermoelectrically cooled InGaAs/InP SPAD (SPD_OEM_NIR) offers high efficiency at 1000 nm (QE $>$ 15%) with 700 counts/second dark count [177]. The SPAD position within the test setup is shown in Figure 5.5. As a feature of the wireless neural dust application, the setup must simultaneously provide radiation for light harvesting and detect the emitted LED pulses [84]. To minimize crosstalk, the PV is powered by 850 nm light while the LED emits at 1000 nm. The InGaAs SPAD advantageously cuts off near 900 nm. A Y-shaped reflection probe (RP23, Thorlabs) handles the two wavelengths. The RP23 consists of a seven-fiber bundle, the central fiber branching to one leg and the outer six going to the other leg. A ferrule combines the legs into a single fiber probe. An 850 nm modulated laser source couples into one leg, while the 1000 nm signal detected at the probe is out-coupled into the SPAD at the other leg. Lastly, given the extreme (indeed, single-photon) sensitivity of the SPAD, it is critical to filter the 850 nm light reflected at the sample

surface. A high-density long pass filter fulfills this task. An 850 nm bandpass filter at the LED output promotes spectral purity. Figure 5.5 shows a schematic of the full optical setup.

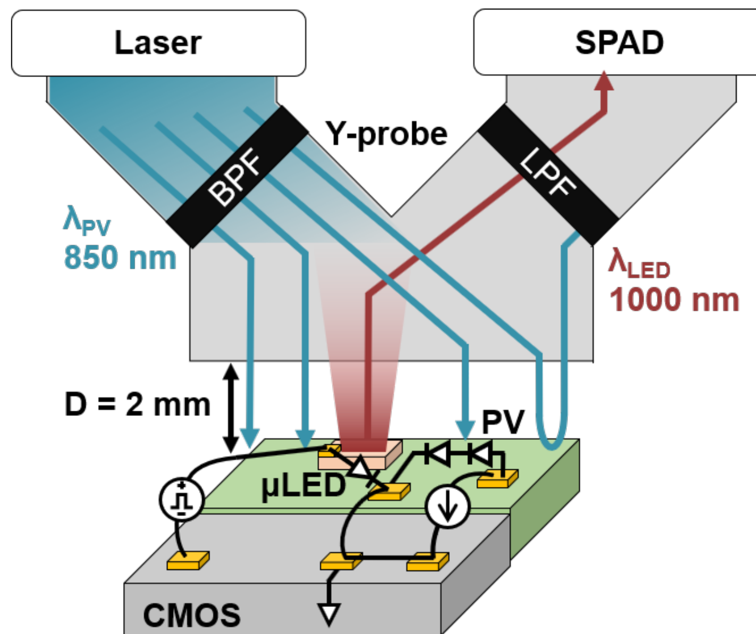

Figure 5.5: Schematic of integrated PV and CMOS chips interfaced with the Y-probe optical setup. All of the components in the Y-probe setup are fiber-coupled. Figure referenced from [179].

Carriers photogenerated in the SPAD active area rapidly multiply via avalanche breakdown. To prepare the SPAD for the next detection cycle, the photogenerated carriers are cleared by a quenching circuit. The quenching duration is known as "dead time", t_{dt}, and places an upper limit on the detector bandwidth. An optimal quenching time of 20 µs ensures low afterpulsing with adequate resolution to detect 50 µs pulses from the LED, as shown in Figure 5.6. The SPAD bandwidth and pulse detection efficiency are also impacted by the dark count rate (DCR), referring to the rate that thermally generated carriers initiate avalanche breakdown. When fully cooled and set for $\approx$ 10% QE with t_{dt} = 10 µs, the DCR is ≈700 Hz. When the laser is turned on with a 0.64 mW/mm^2 intensity, 850 nm light reflects from the GaAs substrate, increasing the effective DCR to 1300 Hz. At λ = 850 nm, the long pass filter transmits 0.038% of photons, affirming the importance of filtering the reflected laser light. Removing the 850 nm bandpass filter raises the effective DCR to 10 kHz.

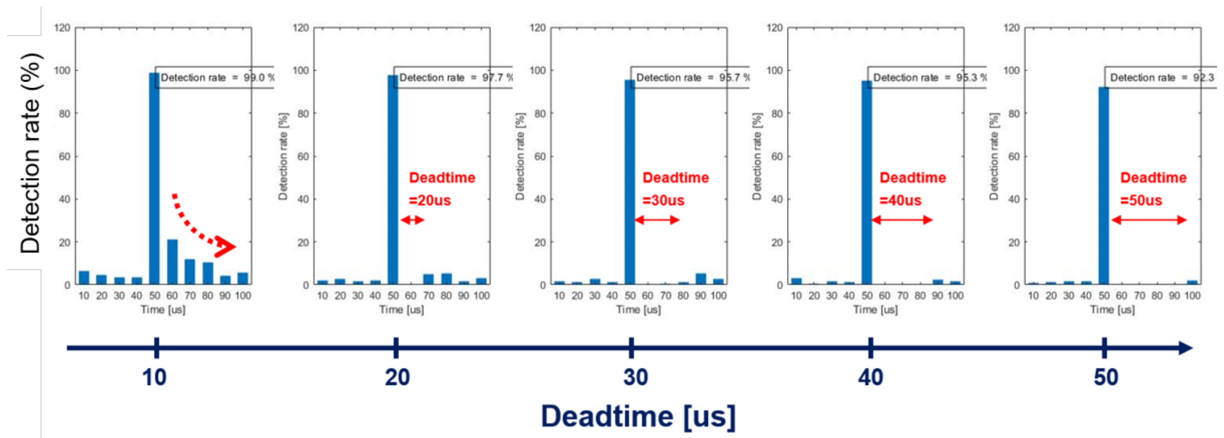

Figure 5.6: Afterpulsing after a 10 µs LED pulse for several dead time durations. (The measurements and figure are provided by Jongyup Lim).

The many components possess variously sized optical fiber cores. Specialty components such as the SPAD (Ø 50 µm) and RP23 (Ø 200 µm) are fixed, while the fiber patch cables are flexible. Filters are housed in specialty compartments for rapid interchanging. A collimating lens couples light from the fiber to the free space of the filter compartment. Light transmitted through the filter(s) couples back into a fiber via a second collimating lens with a coupling efficiency proportional to the fiber core diameter. However, mismatch with the Ø 50 µm SPAD coupler presents another loss avenue. Given these considerations, it was found that the Ø 200 µm fibers allow the highest efficiency amongst the other commercially available core sizes. Photographs of the experimental optical setup are shown in Figure 5.7. The figure shows a slight variation on Figure 5.5, where a fiber-coupled LED is used in place of the laser.

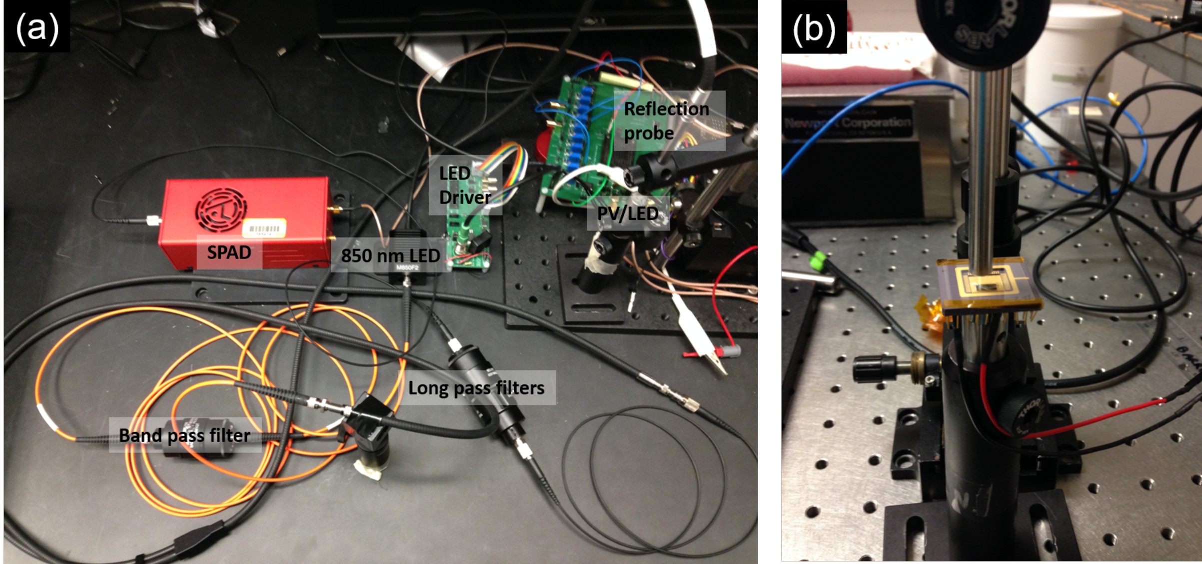

Figure 5.7: Photographs of the optical setup showing a) the total setup and b) a closer view of the sample/probe interface.

5.3.2 Empirical Pulse Detection Probability

The neural dust system in Reference [84] differentiates each mote by a randomly generated on-chip ID. Detected neural activity is transmitted via the NIR uplink in the form of digital pulses corresponding to the mote ID. Accurate recordings require both high fidelity detection and minimal crosstalk between nearby motes. It is imperative to determine the detection efficiency to properly choose the pulse power and duration. Poor optimization can severely degrade the detection bandwidth and accuracy. Pulse detection is a probabilistic function, as the SPAD signal is binary; either a photon initiates avalanche breakdown or it does not. The probability that an emitted photon initiates a detection event is given by:

$$P_{det,photon} = QE_{SPAD} \cdot \eta_{link} \tag{5.4}$$

In this case η_{link} still refers to percentage of emitted photons that reach the SPAD, though the link now consists of propagation through dura as well as the Y-probe setup. An unpackaged mote was wire-bonded to a pin grid array and the Y-probe was positioned approximately 1 mm above, as shown in Figure 5.7b. The measured attenuation of η_{link} was -61.3 dB (7.35e-3%), -43 dB of which occurs after light has been coupled into the Y-probe. Thus, for a 10% SPAD QE, an emitted photon at a distance of 1 mm has a 7.35e-4% chance of initiating a detection event. If a pulse contains *N* photons, the probability that the pulse is detected is given by Equation 5.5. For example, achieving a 99% pulse detection probability requires 62654 photons.

$$P_{det,pulse} = 1 - (1 - P_{det,photon})^N \tag{5.5}$$

This, however, significantly underestimates η_{link} for an array of detectors embedded beneath the skull, such as Reference [84] envisions for the subcranial repeater unit. Pixelated SPAD detector arrays are commercially available. An example includes the SPC3 series (Micro Photonic Devices), which consists of a 64x32 array of 30 µm wide SPADs with a 150 µm pitch [178]. The specifications are well-suited for the wireless neural dust application, with 300 Hz DCR, $\approx 1\%$ QE, and 100 ns dead time. For a SPAD array, the pulse detection probability needs to be calculated for both aligned and misaligned detectors. Since the NIR link is analogous to a free-space LiFi network [179], the power incident on the detector is

$$H_{DC} = \frac{(m+1)A_r}{2\pi D^2} cos^m(\phi) cos(\psi) 1_{\psi \leq \psi_{FOV}}(\psi) \tag{5.6}$$

$$m = -log_2(cos(\phi_{1/2})) \tag{5.7}$$

where ϕ is the radiant angle between the LED and SPAD, ψ is the angle between the LED and the direction normal to the SPAD, ψ_{FOV} is the SPAD field of view, A_r is the SPAD area, *D* is the distance between the SPAD and LED, and *m* is the Lambertian emission order determined by the half-power semi-angle $\phi_{1/2}$. Equation 5.6 is an approximation, since it assumes small solid angles, where $D^2 >> A_r$. The link efficiency must then be revised to

$$\eta_{link}(\phi, \theta_1, \theta_2) = \eta_{dura} \int_{\theta_1}^{\theta_2} H_{DC}(\phi, \theta)\, d\theta \tag{5.8}$$

where $\theta_{1(2)}$ is the radiant angle from the LED to the near(far) edge of the SPAD and η_{dura} is the transmission probability through the dura. The preceding analysis estimates the dependence of pulse detection efficiency on SPAD misalignment. The model considers SPADs with 2 mm vertical displacement and 30 μm^2 active area. 17.9×10^{-12} Coulombs/pulse are supplied to the LED, corresponding to 1.9×10^6 photons/pulse at λ = 1000 nm. The SPAD and LED QE are 10% and 1.7%, respectively. Under these conditions the pulse detection remains >99% for 200 µm displacement and >50% for 3 mm displacement. This bodes well for alignment tolerance, but suggests major crosstalk between adjacent motes. That is, an emitting mote will trigger a large number of SPAD pixels. This poor light collimation is due to the approximately Lambertian emission profile and tissue scattering within the dura. Fortunately, crosstalk may be overestimated since the model does not account for specular reflection at the high index contrast interface between dura/water and the SPAD semiconductor, which increases with angle of incidence.

To determine the number of emitted photons needed to register a pulse, it is not enough to use

Equation 5.5. Though this expression correctly models the likelihood of missing pulses, it does not account for the signal-to-noise ratio (SNR). Depending on the DCR and the detection time window (Δt), the number of photons emitted by the LED must exceed

$$N_{LED} > \frac{(DCR)(F)(\Delta t)}{\eta_{link} QE_{SPAD}} \quad (5.9)$$

where F is the noise margin for the number of additional photons needed to achieve a given SNR, η_{link} is defined in Equation 5.8, and QE_{SPAD} is the SPAD quantum efficiency.

Chapter VII.3 summarizes the culmination of this chapter's work, wherein the CMOS neural recording chip [84] is integrated with a PV/µLED chip (PV cell presented in [171]). The Y-probe setup is aligned ≈2 mm above the PV/LED and an 850 nm LED illuminates the PV cell with 150 µW/mm^2 optical intensity, which is below the 190 µW/mm^2 exposure limit. A test neural signal triggers an LED pulse train. Under these realistic conditions, the decoded SPAD output identifies LED pulses with an over 99% detection rate [87].

CHAPTER 6

Hybrid Integration of GaAs-Based Optoelectronic Devices and Si CMOS Chips for Neural Systems

6.1 Mote Assembly Overview

While Chapter V details important progress, a true demonstration of wireless neural motes requires full mote assembly. The proposed design in Figure 6.1 has a $150\times170\times190$ μm^3 volume (not including the carbon fiber shank) [84]. These tiny dimensions push the envelope in circuit design, PV efficiency, microfabrication, and surgical implementation. Cortese et al. demonstrated an NIR-powered microscale sensor at similar dimensions, though the system only contains a Si PV cell, a µLED, and a field effect transistor to amplify the detected signal [82]. Wireless neural recording prompts more sophisticated circuitry. The CMOS integrated circuit (IC) in Reference [84] contains circuits for clock and data recovery, random chip-ID generation, spiking-band power detection, neural recording amplification, and an LED driver.

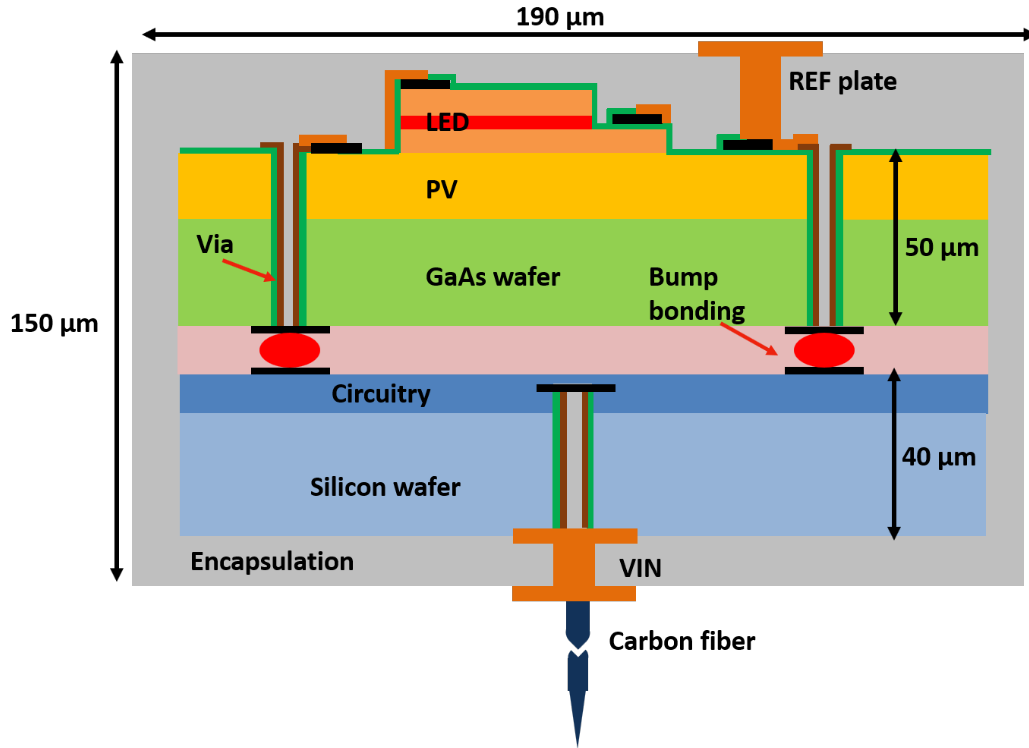

Figure 6.1: Schematic cross-section of the fully assembled wireless neural mote.

Scaling to smaller sizes complicates mote design and construction. As the motes shrink so does the available footprint of the IC and the PV active area. The PV supplies less current while the LED power requirements remain largely unchanged. Further, non-radiative sidewall recombination worsens at smaller PV dimensions [86, 180]. It is therefore essential that the IC and PV encompass the entire 150×170 µm^2 footprint. To utilize the respective advantages of Si and GaAs, mote assembly requires heterogeneous integration of these disparate material systems. Many interesting approaches have been proposed to meet this challenge. Direct bonding heterogeneous wafers allows high alignment accuracy but is mostly confined to back-end CMOS processes [181]. Novel approaches such as epitaxial growth of GaAs on Si [182] and micro-transfer printing [183] are still in development. Flip-chip bonding is a mature technology poorly suited to large scale integration, but realistic for small batches of motes. In addition to stringent lateral dimensions, the proposed design is exceptionally thin (150 µm). This has steep fabrication consequences since thinned wafers are brittle and require careful mounting to avoid damage and bowing during processing.

This chapter explores the challenges and solutions to realize the complicated design in Figure 6.1. Special attention is given to three areas of the fabrication process flow: 1) GaAs through-wafer vias 2) blind Si probe vias for carbon fiber insertion and 3) heterogeneous integration. The CMOS

circuitry is fabricated at an industrial foundry in the 180 nm node. The multilayer PV and LED structures are grown via molecular beam epitaxy on a semi-insulating GaAs substrate. LED mesa structures, contact pads, and interconnects are defined using standard microfabrication techniques.

6.2 GaAs Through-Wafer Vias

The mote assembly consists of four components: the LED, the PV, the IC, and the carbon fiber probe. The PV and LED are monolithically integrated in the same epitaxial stack and are positioned at the mote surface to maximize light harvesting and LED signal strength. On the opposite side of the mote, the carbon fiber probe inserts into brain tissue. These basic considerations fix the orientation of the GaAs and Si wafers as shown in Figure 6.1. PV-generated current flows to the IC, while signal detected by the probe is relayed to the LED. This requires an electrical conduit between the top and bottom of the GaAs wafer, known as a through-wafer via (TWV). Though through-silicon vias are well-established in 3D ICs [184], GaAs TWVs have seen considerably less attention. The generalized process flow is illustrated in Figure A.6 in Appendix A.2. For thorough review of TWVs, the curious reader is directed to References [185–187].

6.2.1 Via Hole Definition

GaAs TWV fabrication begins by defining an etch mask, followed by pattern transfer into GaAs by an anisotropic etch. Maximizing the PV active area means minimizing the TWV size. The target via hole dimensions are thus deep ($\approx$60 µm) and high aspect ratio (AR, $>$3:1). This places several demands on the etching process, which must be anisotropic, highly selective to the etch mask, and produce reasonably smooth sidewalls. Inductively-coupled plasma reactive ion etching (ICP) is an attractive option. An inductive coil generates a high density of reactive species in plasma, which are accelerated by an RF bias to an electrode holding the sample. Via the dual action of chemical and physical etching, a well-optimized ICP process can exhibit excellent anisotropy with high selectivity between various materials. In this work, 15-35 µm wide TWVs are patterned into a photoresist (PR) etch mask. An HBr-based ICP process transfers the pattern into GaAs. Process details are given in Appendix A.2.

Bromine etch chemistries are uncommon in the GaAs device literature, the bulk of which utilizes chlorine- or fluorine-based etchants (e.g. Cl_2, BCl_3, CCl_3F_2, CHF_3, etc.) [131–133, 188]. An HBr-based ICP process deviates from this trend. HBr ICP is a proven alternative for shallow InP and GaAs structures, such as gratings and ridge waveguides [137, 138], yet no results are published for deep through-wafer structures. The HBr ICP process gives a favorable trade-off between etch rate, sidewall quality, and selectivity to a PR mask. Figure 6.2a shows a cross-sectioned

GaAs TWV after a 35 min HBr ICP etch. The time averaged etch rates for TWVs with 2.3:1 and 3.2:1 ARs were 2.6 µm/min and 2.3 µm/min, respectively, corresponding to 91.5 µm and 79.0 µm etch depths. This is comparable to chlorine-based processes, at $\approx 50\% - 150\%$ of the published rates [131–133]. Exceptional selectivity to PR is another advantage of the HBr ICP process, with >80:1 GaAs:PR selectivity. High selectivity to PR minimizes etch mask erosion and enables high-fidelity pattern transfer and smooth sidewalls after long etch durations.

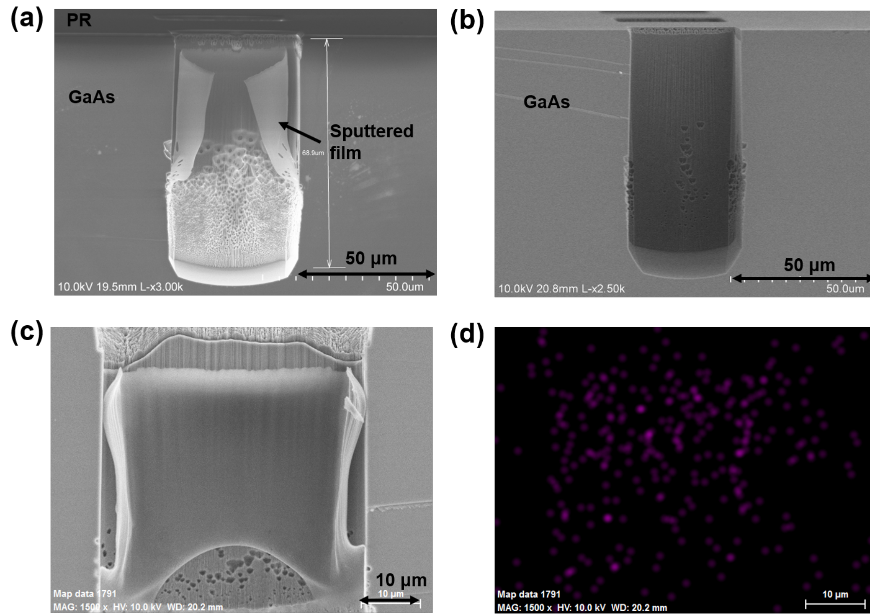

Figure 6.2: SEM cross-sectional images of a GaAs TWV a) immediately after ICP and b) after a BHF dip and O_2 treatment. c) SEM image of post-etch sidewall passivation. d) Energy-dispersive X-ray spectroscopic imaging of (c) for energies corresponding to Si transitions.

A thin sputtered film conspicuously coats the TWV sidewalls in Figures 6.2(a, c). As shown in Figure 6.2d, energy-dispersive X-ray spectroscopic measurements suggest that this film is a Si-containing polymer, a claim corroborated by other studies [133, 138]. The use of a PR soft mask in Figure 6.2 implies that the Si originates at the Si carrier and/or quartz chamber walls. Si plays two important roles in the HBr ICP process, protecting the TWV sidewalls from lateral etch and stabilizing the plasma. Replicating the results in Figure 6.2 requires a large area of exposed Si ($\approx 90\%$ in this study). A short BHF dip cleanly removes the sputtered film as shown in Figure 6.2b. The excellent verticality and minimal sidewall roughness are a testament to the passivating qualities of the Si-containing film. As the AR increases, the thickness of the Si film decreases while sidewall pitting worsens. This is possibly due to transport limitations, as sputtered Si is more likely to adsorb near the top of the vias. Since Br is less electronegative than Cl and F, the physical component of the ICP process is of greater importance, promoting sidewall quality

and anisotropy at the expensive of etch rate. There is evidence that adding O_2 may thicken the Si passivation layer [138], though the ICP tool does not permit a low enough O_2 flow to confirm this. For any chemistry, basic ICP principles introduce trade-offs between sidewall quality, etch rate, and material selectivity [131–133, 137, 138, 189]. The sidewall quality may be improved by lowering the chamber pressure and/or the HBr flow rate. Reference [132] describes a Cl_2-based ICP etch that produces GaAs TWVs with smooth sidewalls, a 3 µm/min time averaged etch rate at 10:1 AR, and high selectivity to a PR mask. It is therefore unclear which etch chemistry is superior for GaAs TWVs, but HBr shows promise and meets the needs of the motes.

6.2.2 Thin Film TWVs

After etching the via holes, the TWVs need to be electrically isolated from the GaAs substrate and coated with a conductive film. Infilling the vias with copper allows mΩ-scale resistances [185]. Electrochemically deposited (ECD) Cu requires a conductive seed layer to initiate plating and provide a current path to reduce adsorbed Cu ions. Figure A.6 in Appendix A.2 shows the fabrication process flow. In applications requiring only sub-kΩ TWV resistance, it is possible to skip the complication of Cu ECD and simply be content with the conductive thin film layer. Atomic layer deposition (ALD) is an ideal thin film deposition technique, allowing conformal deposition of metallic and dielectric thin films with precise thickness control. A 300 Å layer of insulating Al_2O_3 is deposited, followed by a 100 Å layer of conductive TiN. After ALD, the sample surface is coated in a 7 µm thick layer of parylene C, infilling the vias and providing critical structural support for thinned GaAs. Lastly, the chip is thinned to 50 µm and Ti/Au contacts are patterned on the backside of the TWVs for electrical measurement. A microscope image of the sample backside after thinning is shown in Figure 6.3a.

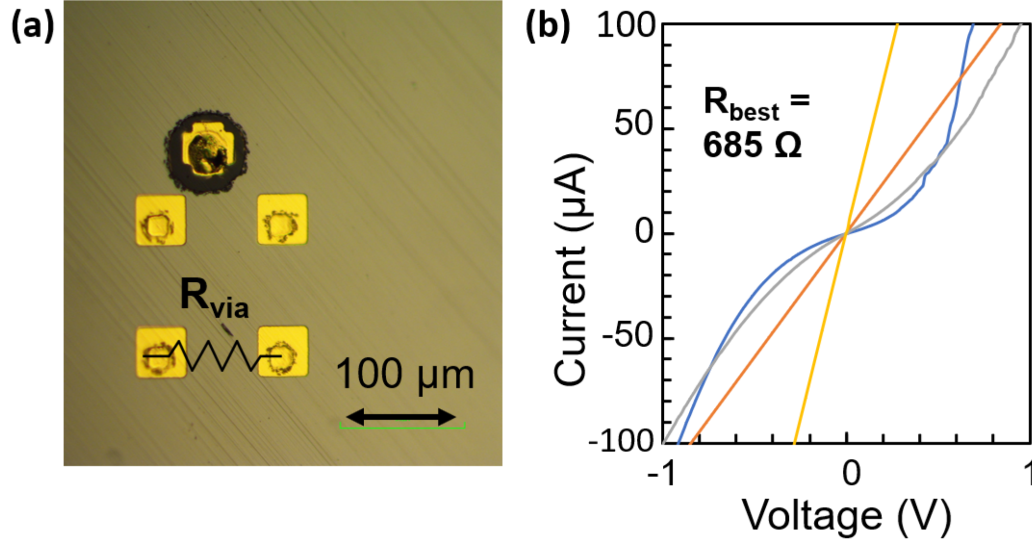

Figure 6.3: a) Optical microscope image of the backside of a thinned GaAs sample, showing Ti/Au contact pads above parylene-infilled thin film TWVs. b) Measured I-V curves for several representative GaAs TWVs.

Electrical measurements are performed by probing the backside contact pads and extracting current-voltage (I-V) curves using a Keithley 4200 parameter analyzer. The TWVs are shorted at the surface by TiN, thus the current path between adjacent TWVs consists of the two TWVs and the planar TiN connecting them (100 µm distance). DC via resistances (R_{via}) are calculated by dividing the slope of the I-V curve by two, noting that the TiN connection at the surface makes this somewhat of an overestimation. Figure 6.3b shows representative I-V curves for the thin film TWVs with a best measured value of R_{via} = 685 Ω for TWVs that are 20 µm wide and 50 µm deep. The considerable variability between structures is attributed to non-uniformities in the TiN film, particularly near corners and other sharp features. Hall effect measurements of unpatterned TiN on semi-insulating GaAs indicate a resistivity of ρ_{TiN} = 1.45x10^{-4} Ω· cm. For a 20 µm diameter circular TWV that is 50 µm long, ρ_{TiN} gives R_{via} = 110 Ω, which is the same order of magnitude as the observed values.

6.2.3 Seed Layer Patterned TWVs

Applications requiring lower R_{via} necessitate a Cu infill. As shown in Figure A.7 in Appendix A.2, the Cu-filled TWV process flow begins similarly to the thin film TWVs. After defining the via holes, ALD Al_2O_3 insulates the sidewalls while 100 Å of ALD Pt acts as a seed layer for Cu ECD. While TiN is sufficiently conductive, poor Cu adhesion was observed. Additionally, the Pt seed layer provides a barrier for detrimental Cu diffusion into GaAs [190]. Since the Pt seed

layer conformally covers the entirety of the sample surface, Cu will be plated everywhere. This technique, known as ”damascene plating”, is the predominant Cu plating technique for TWVs. Cu plated on (or protruding above) the chip surface is known as overburden. Overburden shorts the TWVs, enlarges the mote form factor, and blocks NIR transmission. In high-density CMOS applications, overburden is removed by chemical-mechanical polishing (CMP). However, CMP presents many uncertainties, since CMP increases fabrication cost and complexity and is less understood for GaAs processes [191]. CMP may also endanger delicate surface structures like the PV/LED mesas in the motes. Lastly, for thinned chips mounted with a temporary adhesive, total thickness variation presents a major cause of defects during CMP. For these reasons, the neural dust motes require a CMP-less GaAs TWV fabrication process flow.

The literature offers several techniques for CMP-less TWV fabrication. One solution uses a wet copper etch to remove most of the overburden, but leaves an unacceptable amount for mote assembly [192]. Another strategy electropolishes the overburden using a negative anodic current in a phosphoric acid bath [193]. While effective, precise timing control is needed to avoid excessive electropolishing, similarly to dishing in CMP. To overcome these limitations, two novel CMP-less process flows are proposed. In the first, referred to as ”seed layer patterned TWVs”, the Pt seed layer is selectively patterned and etched, as shown in Figure 6.4a. This technique allows the simultaneous plating of TWVs and surface-level interconnects. Figure 6.4b shows the Cu-plated interconnects after ECD. A pulsed plating program encourages deposition uniformity by periodically turning off the power supply, allowing the Cu^{2+} concentration to regain equilibrium [194]. Further details of the plating process are given in the Appendix A.2. Figure 6.4c shows the backside of the chip after thinning, revealing significant non-uniformity in Cu thickness between TWVs. In most of the vias, the Cu is only a few µm thick. As shown in the SEM cross-section in Figure 6.4d, Cu plates the surface interconnects much more rapidly than the TWVs. Contact profilometric measurements reveal an interconnect height of $\approx$16 µm despite the TWV plating being only a few µm thick. Though the ECD process is poorly optimized, the vias are significantly more conductive than their thin film counterparts whose conductive layer is only 10 nm thick. Figures 6.4(e, f) show experimental R_{via} measurements, revealing a best value of 1.7 Ω. This technique is, however, sub-optimal for mote assembly, since the Cu interconnects are themselves overburden and must be broken to electrically isolate the TWVs.

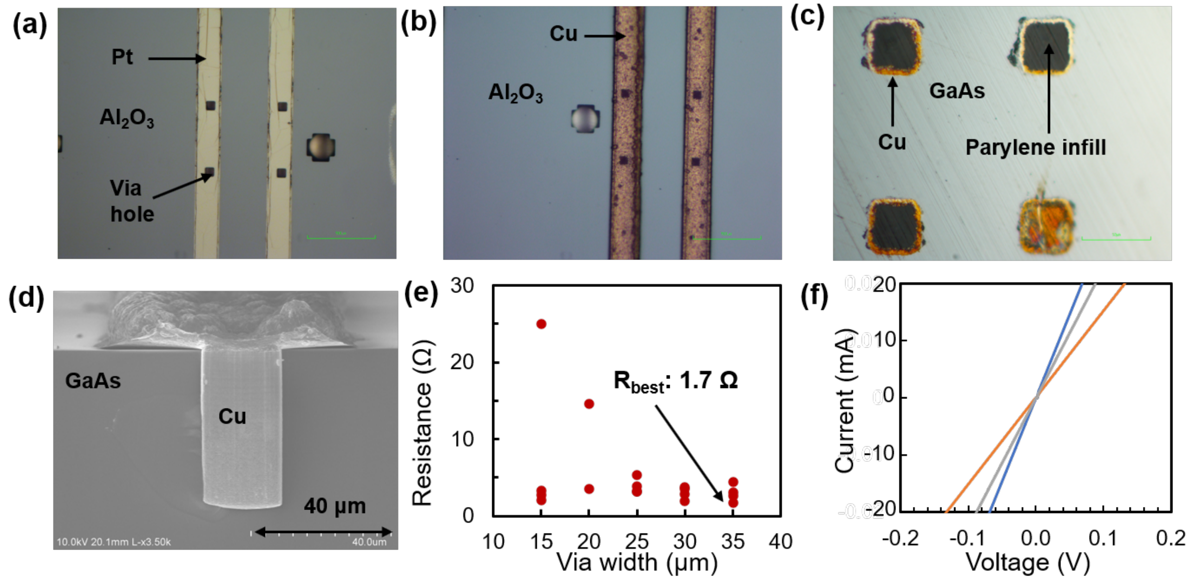

Figure 6.4: Optical microscope images of a) Pt seed layer patterning b) Cu-plated interconnects c) the backside of a thinned GaAs chip after ECD. d) SEM cross-sectional image of a plated TWV. e) Measured via resistances for several opening widths. f) Measured I-V curves.

6.2.4 Selective Damascene Plating

Traditional damascene plating requires CMP since the electroplated metal covers the entire chip surface. This section introduces ”selective damascene plating”, wherein the sample is conformally coated in a Pt seed layer yet plating is restricted to the TWVs. This is accomplished using pulse reverse current (PRC) plating and an evaporated TiO_2 mask. In PRC, a negative bias is placed on the anode for a short duration after the forward pulse, as shown in Figure 6.5. During the reverse pulse, ECD copper is oxidized and removed from the vias, a process that occurs more rapidly near the top of the structures [193–197]. For purely forward pulse plating, the top of the vias close off before the TWVs are completely infilled, leaving a keyhole in the center. On the other hand, the stripping step during PRC enables bottom-up filling and reduces overburden. The other essential technique is the deposition of a TiO_2 mask before plating (see Appendix A.2 for process details). Evaporation via an electron beam is highly directional, leaving a thick layer of TiO_2 on the chip surface but a negligible amount on the sidewalls. The deposited mask is self-aligned to the TWVs and is easily removed by a short BHF dip. PRC plating promotes bottom-up filling while the dielectric mask prevents any surface deposition.

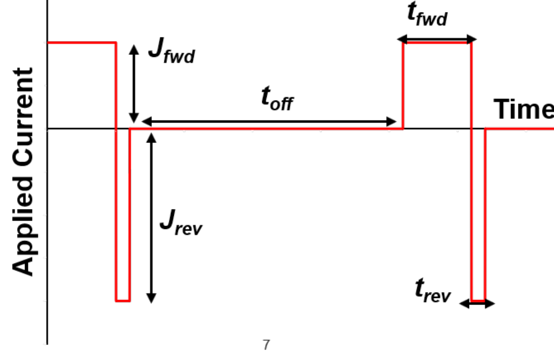

Figure 6.5: Pulse timing program for pulse reverse current plating.

Figure 6.6 compares PRC plating to pulse forward plating using a set of TWVs with an evaporated TiO_2 plating mask. The current densities and timing parameters are given in Table 6.1. The plating durations (T_{total}) are chosen for equal charge transfer, as given by:

$$T_{total} = Q_{total} \cdot (t_{fwd} + t_{rev} + t_{off})/(I_{fwd} \cdot t_{fwd} - I_{rev}) \cdot t_{rev}) \tag{6.1}$$

where Q_{total} is the total charge transferred. For example, the parameter sets in Table 6.1 both yield Q_{total} = 500 mA·min. As shown in Figure 6.6, the pulse forward TWVs exhibit significant overburden, while PRC TWVs have minimal overburden for an equivalent Q_{total} transfer. This result confirms the fundamental assertions that PRC plating promotes bottom-up filling and that the evaporated dielectric mask prevents Cu deposition on the chip surface. For the neural dust motes, via resistance values on the order of 1-5 Ω are well within the application tolerance. Thus, the TWVs provide a conductive path through the GaAs wafer without the need for CMP to remove overburden. However, the ECD process is clearly nonoptimal as large voids exist at the bottom of each structure. Achieving a complete via in-fill is a difficult task that requires optimizing the five PRC parameters as well as other variables (plating solution, temperature, agitation rate, electrode size and distance, etc.). Increasing t_{off} and t_{rev} promotes bottom-up filling but requires a longer plating time. In fact, if the t_{rev}/t_{fwd} ratio is too large the denominator of Equation 6.1 equals zero and no plating occurs at all.

Plating program	J_{fwd} (mA/cm^2)	J_{rev} (mA/cm^2)	t_{fwd} (ms)	t_{rev} (ms)	t_{off} (ms)	T_{total} (min)
Pulse forward	50	N/A	5	0	10	30
Pulse reverse	50	100	5	1	10	53.3

Table 6.1: Parameters for the pulse forward and pulse reverse plating programs in Figure 6.6

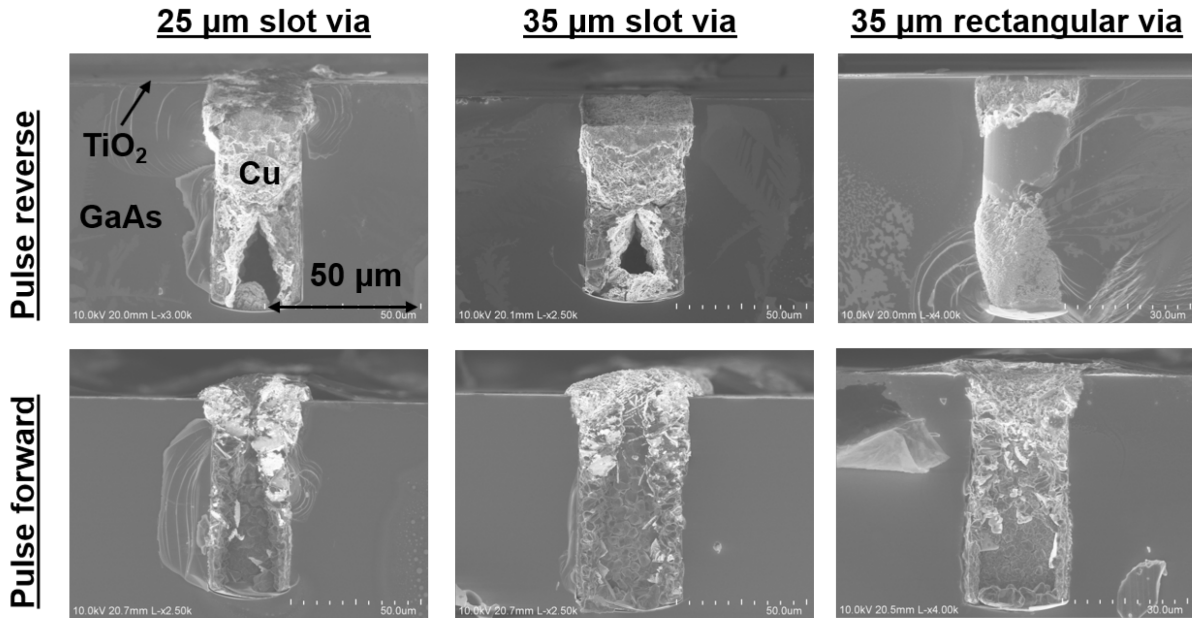

Figure 6.6: SEM cross-sections of Cu-infilled GaAs TWVs. The top row was subject to the PRC program while the bottom had only forward pulses. The slot vias are 100 μm long.

Figure 6.7 exemplifies the efficacy of selective damascene plating. Despite the TiO_2 mask, TWVs given the pulse forward program show many instances of overburden and mask breakdown. Alternatively, the PRC TWVs show no such instances. The failure mechanism is ascertained in Figure 6.7c, where ECD Cu grows on the Pt seed layer beneath the TiO_2. In pulse forward plating there is no mechanism to prevent this and the TiO_2 is simply pushed aside. PRC remedies this by stripping any copper that deposits near the surface. Further, by periodically applying reverse bias, PRC prevents charge buildup at high aspect ratio features, such as surface roughness or via edges. This aids plating uniformity and discourages TiO_2 mask failure. Selective damascene plating has several advantages over other CMP-less TWV strategies. A common strategy for bottom-up filling is the use of organic additives to slow the deposition rate near the top of the TWVs [185, 190, 193, 198]. Compared to PRC plating, the use of additives is expensive, raises optimization complexity, and adversely affects Cu conductivity [194]. As previously mentioned, electropolishing is another option for CMP-less TWV fabrication [193]. This technique uses damascene plating and PRC timing to achieve bottom-up filling and to uniformly deposit Cu on the chip surface. A reverse current uniformly strips the overburden, requiring precise timing control to fully remove overburden without over-stripping the copper infill. Particularly for instances where <1 μm of overburden is acceptable, selective damascene offers a straightforward CMP-less fabrication technique.

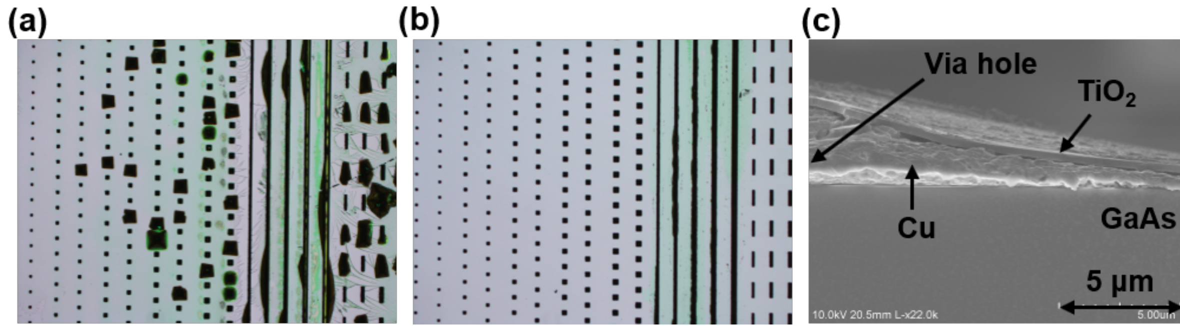

Figure 6.7: Top-down optical microscope images of GaAs TWVs plated with a a) pulse forward and b) PRC program. c) SEM micrograph of a TWV after pulse forward plating, showing Cu deposition beneath TiO_2.

6.3 Blind Si Vias for Carbon Fiber Probe Insertion

GaAs TWVs are not the only vias in the mote assembly. Deep Si vias in the IC chip provide two essential functions. They lend a strong mechanical base for a carbon fiber probe and relay neural data from the probe to the CMOS circuitry. Figure 6.8 illustrates the fully processed Si chip. In addition to the ICs fabricated in the 180 nm process mode, the CMOS chip contains metal layers embedded within dielectric silicon oxynitride (SiO_xN_y). Unlike the GaAs TWVs, the Si probe via is blind, meaning it does not extend completely through the wafer. This presents a particular challenge: how to insulate the via sidewalls while maintaining connection to the buried CMOS metal layer? This section details conductive blind Si vias that solve this dilemma.

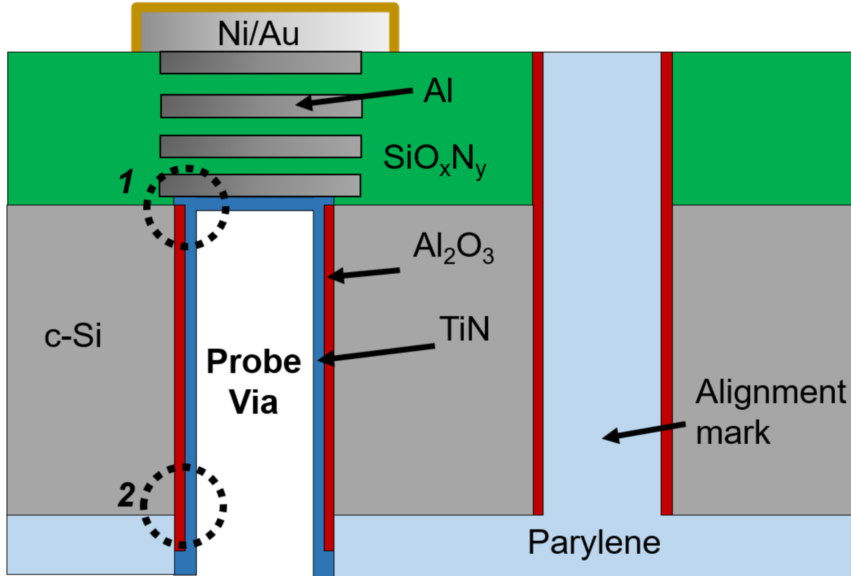

Figure 6.8: Schematic of the fully processed CMOS chip, including blind probe via, through-wafer alignment mark, and Ni/Au solder contacts for flip-chip bonding. The dashed black circles indicate 1) the buried Al etch stop junction 2) the edge leakage path.

To ensure the fidelity of recorded neural signals, via conductivity should be maximal while substrate leakage should be minimal. Designing the fabrication process flow is further complicated by material incompatibilities. For example, a viscous material like PR outgasses at low pressures, making it incompatible with ALD and other high vacuum processes. The blind probe via fabrication is further complicated by its back-end of the line position within the process flow, requiring all of the fabrication steps to be performed on a thinned chip. A self-aligned parylene etch mask overcomes these challenges. The via fabrication process is briefly as follows. An alignment mark is etched through the topside of the wafer, followed by wafer thinning to 40 µm. Next, ≈5 µm of parylene C is deposited on the backside. After spinning thick (≈ 7 µm) photoresist on the parylene, the probe via pattern is aligned to the through-wafer marks and developed into an etch mask. An O_2 plasma transfers the via pattern to parylene, followed by a deep reactive ion etch (DRIE) to etch the Si down to the Al etch stop. To insulate the sidewalls, a 300 Å layer of ALD Al_2O_3 is deposited. Another reactive ion etch removes the ALD Al_2O_3 that covers the exposed Al, allowing a conductive path to the CMOS circuits without compromising the sidewall insulation. Lastly, a 100 Å of ALD TiN makes the via conductive. Optical microscope images, schematic images of key process steps, and greater technical detail are given in Appendix A.3.

Given the difficulty of characterizing the blind vias on a CMOS chip (requiring nearly complete mote assembly), test structures are fabricated on a bulk Si wafer patterned with 500 nm thick aluminum contacts on the topside, serving as an etch stop for probe vias processed on the backside.

Experimental DC measurements are shown in Figure 6.9, showing via resistances as low as 150 Ω. The electrical measurements are similar to the GaAs TWV measurements, where adjacent vias are probed from the backside and shorted through the topside (in this case by a single 100 μm long Al contact).

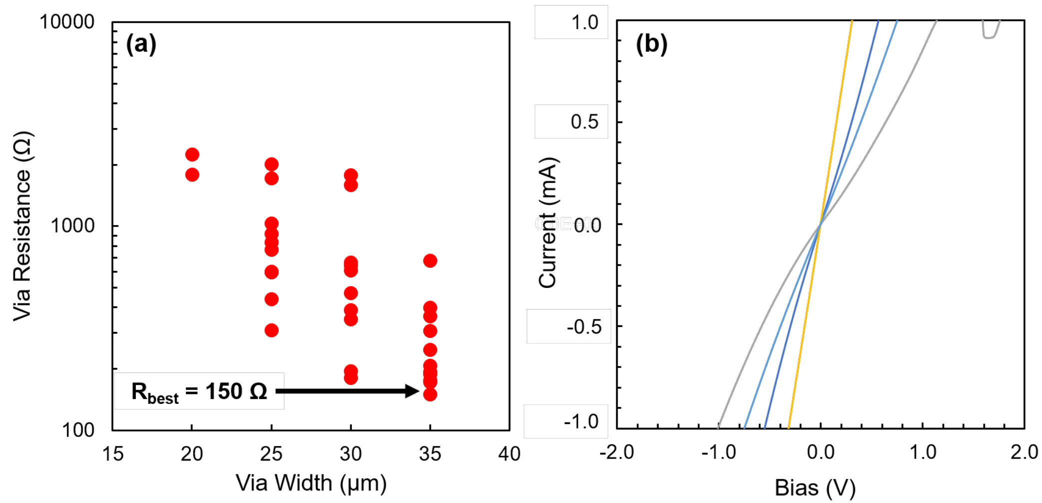

Figure 6.9: a) Measured resistance of blind Si vias with varying nominal widths. b) Characteristic I-V curves for several of the structures in (a).

To understand the relationship between via resistance and width, consider the buried Al contact after Al_2O_3 deposition (denoted by the dashed circle labeled "1" in Figure 6.8). The Al_2O_3 conformally coats the entire via, blocking electrical access to the buried Al etch stop. Given the high directionality of reactive ion etching, the films at the bottom of the via are etched more quickly than the sidewalls. However, this becomes less true for higher aspect ratio vias, as transport limitations reduce the etch rate. Even worse, sample tilt can cause the via bottom to be completely shadowed, preventing any Al_2O_3 etching. These effects becomes worse as the aspect ratio increases. Thus, the narrower vias are less likely to be fully etched through, as reflected by the distribution in Figure 6.9a.

While this technique gives high enough conductivity for the neural dust motes, the substrate insulation must also be confirmed. The dashed circle labeled '2' in Figure 6.8 designates another area of concern. During the Al_2O_3 etch, the surface of the chip will etch at least as quickly as the bottom of the via, inevitably creating a current leakage path at the via edge. However, using the insulating parylene mask, significant edge erosion may occur before a leakage path opens. A similar technique is given in Reference [199]. Parylene is insulating, biocompatible, and may be conformally coated in thick layers. It has seen diverse application in biomedical applications [200–203] and through-silicon vias [199, 204]. Given the high chemical resistivity, oxygen plasma

etching is nearly the sole technique for parylene patterning and removal [200,201,203]. Despite its high stability, deep features may be etched into parylene with minimal sidewall slope, particularly at the probe via aspect ratios (≈1:4 for 20 µm wide vias) [203]. In Figure A.10c of Appendix A.3, the parylene mask yields circular vias that are roughly the correct size.

As shown in Figure 6.10b, the resistance between adjacent vias that are not shorted at the topside is on the order of 10s of GΩ. For the majority of the voltage sweep, the current is below the detection limit. In conclusion, the blind Si probe vias provide sub-kΩ series resistance and GΩ isolation. The self-aligned parylene etch mask helps minimize current leakage and lends structural support to the thinned CMOS chip.

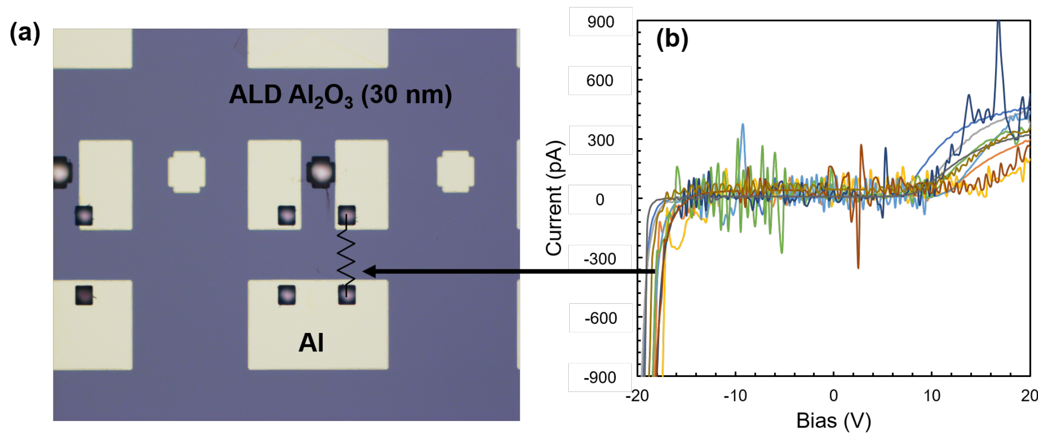

Figure 6.10: a) Optical microscope image showing the measurement setup for the isolation measurements. b) Collection of I-V curves between adjacent disconnected vias. For most of the voltage sweep, the current is below the source meter detection limit.

6.4 Heterogeneously Integrating GaAs and Si CMOS Chips

Integrating the PV/LED and CMOS chips is perhaps the tallest obstacle to full mote assembly. As discussed in Section 6.1, flip-chip bonding is a realistic option for a system of this complexity [205]. Flip-chip bonding requires solder pads on the top of the CMOS chip and the bottom of the PV/LED chip. Using solder jetting and a short, localized laser reflow, the pads on the CMOS chip are bumped with solder balls. The PV/LED chip is then flipped and aligned to the CMOS chip. Finally, the solder is reflowed at high temperature, assuring electrical and mechanical connection. In many flip-chip applications, the gap between the chips is underfilled with a dielectric material. This section describes a conventional flip-chip process flow, though alternative techniques such as anisotropic films and nonconductive adhesives are promising [206]. Both chips are thinned to <50 µm prior to bonding. Thin film stress induces extreme bowing on the order of millimeters,

requiring a temporary bonding technique that minimizes total thickness variation (TTV) and is compatible with high reflow temperatures.

To heterogeneously integrate the CMOS and PV/LED chips, contact pads are first defined on both chips. In the microelectronics industry, the solder pads are referred to as 'under bump metallization' (UBM). UBM typically consists of electrolessly plated Ni or Cu coated wtih a thin noble metal to prevent oxidation [207]. To obtain adequate shear strength, flip-chip pads are typically several micrometers thick, whereas metal layers deposited via physical vapor deposition are <1 µm. The electroless UBM processes are not amenable to thin, mounted chips or the laboratory setting generally. Instead, the chips are coated in a 50 nm Au seed layer and spin-coated with photoresist. A contact pad pattern is exposed into the photoresist mask and 3-5 µm thick Ni contacts are deposited using pulsed electrochemical deposition. Another 50 nm Au deposition coats the UBM, followed by ion milling to remove excess Au. Appendix A.4 provides process details. Figure 6.11 shows SEM images of solder balls jetted and reflowed on the Ni/Au UBM.

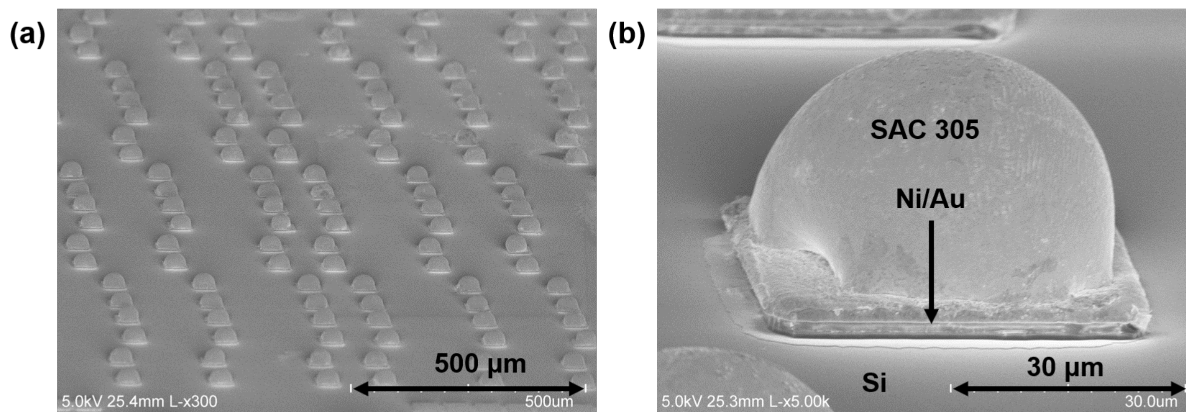

Figure 6.11: Perspective SEM images of solder bumps jetted onto Ni/Au UBM after reflow.

For successful flip-chip bonding, the mounting technique must be temporary, have low TTV (<10 µm), and be stable at the solder reflow temperature. A beeswax-like polymer is used in this work. First, the beeswax is melted on a carrier wafer at 85°C and spread over an appropriate area. Next, the thinned sample is placed on the melted wax and compressed under high pressure for 5 min at 85°C. The high pressure allows only a thin layer of beeswax between the sample and carrier. Surface tension keeps the sample firmly affixed to the carrier, enabling low TTV even at temperatures above the beeswax melting point. After 15 min, pressure is removed and the carrier is rapidly cooled on a water-cooled table. Excess beeswax is cleaned with xylenes, acetone, and IPA. A photo of a mounted 3x2.6 cm^2 Si test chip is shown in Figure 6.12a. The chip contains a 2x2 array of ≈4x5 μm^2 dies, each consisting of 480 UBM bumps and through-wafer alignment marks. The contact profilometric measurement in Figure 6.12b shows that TTV across one die is

on the order of 1-2 µm, which is well under the ≈10 µm requirement for solder bump jetting.

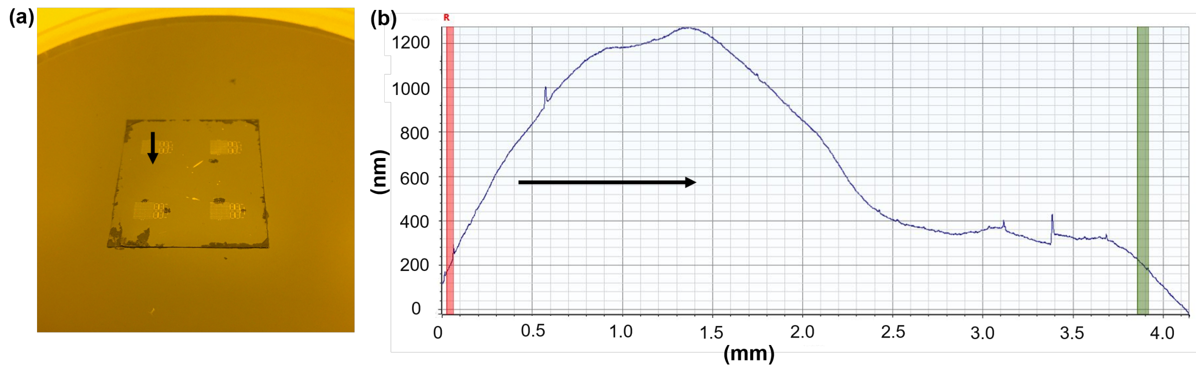

Figure 6.12: a) Photo of a 50 µm thick Si test structured mounted to a Si carrier with beeswax. The black arrow indicates the profilometric path taken in (b). b) Contact profilometry of the mounted Si piece in (a).

Due to the temporary adhesive mounting, thermal budget is limited. Thus, a laser reflow is ideal, since a small beam spot can provide localized thermalization without heating the substrate. The samples in this work are bumped via the SB^2-Jet process offered by PacTech, wherein solder balls are individually jetted on the UBM pads and reflowed by a 1064 nm laser. Up to 8 J can be delivered in 10 ms at the bumps while maintaining approximately ambient conditions at the substrate. A <6 mrad beam divergence assures high localization. SAC 305 (96.5% Sn, 3% Ag, and 0.5% Cu) is used in Figure 6.11. SAC 305 melts at 217°C and is typically reflowed at 233-235°C. The initial solder ball height is 40 µm, and reduces to ≈27 µm after laser reflow. Every tested solder joint withstood 13.6 gf pad lift and 12.6 gf ball shear tests. As shown in Figure 6.11, solder balls were accurately placed on the UBM of a thinned Si test chip. This positive result is largely attributable to the low TTV allowed by the beeswax mounting technique and the nearly nonexistant substrate heating during laser reflow.

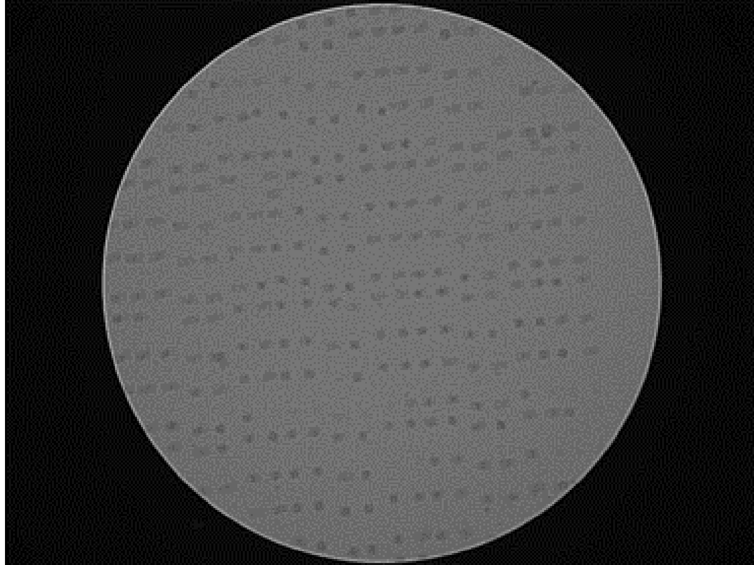

Figure 6.13: X-ray image of the bonded solder junctions after flip-chip alignment and reflow.

Early attempts at flip-chip bonding the two thinned chips show mixed results. As shown by the X-ray image in Figure 6.13, the chips are well-aligned. However, the flip-chip process uses a global 233°C reflow to attach the solder balls to the PV/LED chip. Though the chips are well-bonded, the beeswax chemistry is altered, preventing dismounting from the carrier wafer. Further process development is needed to overcome this limitation. It is unclear at which temperature the changes occur. Using a lower temperature solder, such as Sn42/Bi58 (T_{melt} = 138°C)), may be a solution. Laser reflow may also be used for flip-chip bonding, though it is unclear how well the laser will transmit through the substrate. Lastly, the use of a non-conductive adhesive may lower the temperature requirement [206].

Several questions still linger for the realization of the mote in Figure 6.1. Dicing and encapsulation processes remain untested and are described in Chapter VII. Preliminary results for carbon fiber probe insertion experiments are also included. Chapter VII illuminates the remaining path for the novel wireless neural assembly, highlighting possible strategies for heterogeneous integration, dicing, encapsulation, and carbon fiber probe insertion.

CHAPTER 7

Future Work and Conclusions

7.1 Hyperspectral Imaging via Subwavelength Grating Filters

The subwavelength grating (SWG) filters studied in Chapters II-IV are partially motivated by hyperspectral imaging (HSI) systems and their myriad applications [55–62, 64–66]. Recall that HSIs strive for high-spatial and -spectral resolution, necessitating compact and narrowband spectral filters. A schematic of a 2×2 HSI pixel is shown in Figure 7.1, containing electrically isolated solid state detectors integrated with a SWG filter array. The resonant wavelength (λ_i) of each filter is statically tuned by adjusting the period, Λ, with each detector corresponding to a different wavelength.

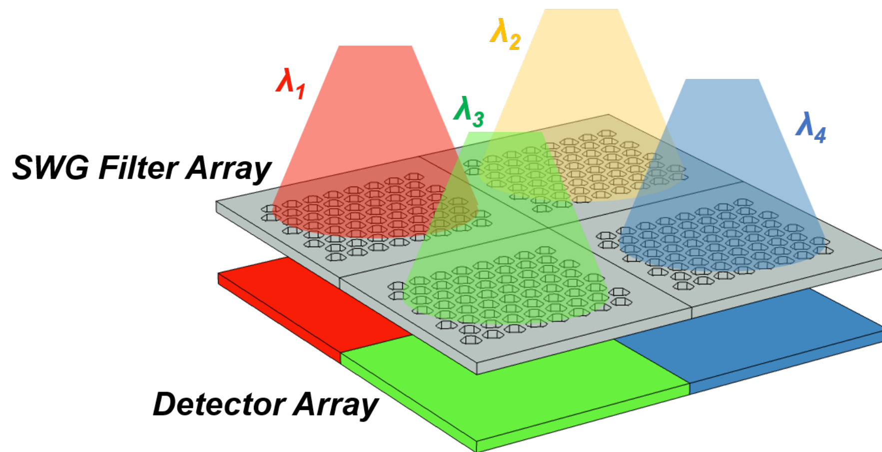

Figure 7.1: Schematic of a hyperspectral imaging pixel, containing a SWG filter array integrated with a solid state detector array.

The prospect of directly integrating SWG filters with solid state photodetectors is bolstered by the GaAs high contrast gratings (HCG) in Chapter III and the reduced-symmetry hexagonal grating design in Chapter IV [70]. The polarization-independent hexagonal grating design is well-suited for the HSI application. By geometrically tuning the peak linewidth, optimization of the

filter size/resolution trade-off is straightforward. Furthermore, InGaAs photodetectors offer efficient NIR detection, with cut-off wavelengths exceeding 1700 nm. InGaAs, AlGaAs, and GaAs are readily integrated via epitaxial growth, prompting monolithic integration between an InGaAs detector, an AlGaAs etch stop, and a GaAs HCG. Emerging room-temperature infrared photodetectors, such as InGaAs/GaAsSb Type-II superlattices [208], may push the cut-off wavelength beyond 2.5 µm while maintaining compatibility with suspended GaAs photonic structures.

7.2 Neural Mote Assembly

The neural motes still require considerable effort to realize the fully working system in Figure 6.1. After individual processing, the CMOS and PV/LED chips must be heterogeneously integrated, diced, inserted with a carbon fiber probe, and hermetically sealed.

7.2.1 Heterogeneous Integration

Chapter VI demonstrated progress toward heterogeneously integrating $<$50 µm thick Si CMOS and GaAs PV/LED chips. As shown in Figures 6.11 and A.11 in Appendix A.4, solder jetting and laser reflow can reliably bump the chips with $\approx$27 µm thick SAC 305 solder balls. Preliminary efforts to bond the two chips gave mixed results. Though the chips are well-aligned, the high SAC 305 reflow temperature (T_{re}, 233°C) produced chemical changes in the temporary beeswax adhesive, inhibiting sample dismount after flip-chip bonding.

Going forward, it is imperative to develop a flip-chip bonding process that is in harmony with the temporary adhesive. The two optimization knobs are T_{re} and the choice of adhesive. The adhesive must admit low ($<$10 µm) thickness variation, maintain adhesion at T_{re}, and be easily removed after bonding. If this last condition is not met, such as with beeswax at T_{re} = 233°C, the assembly may be destroyed while dismounting from the carrier wafers. Most polymer adhesives transition to liquid well before 233°C, though they are still viable if surface tension is strong enough to hold the chips in place. Alternatively, T_{re} may be reduced by using a lower temperature solder, such as Sn42/Bi58 (T_{re} = 138°C), or using a flip-chip process that minimizes substrate heating. Examples of the latter include laser reflow and non-conductive adhesives (NCA) [206]. As shown in Figure 7.2, NCA flip-chip bonding mates the two chips under high pressure. Instead of reflowing the solder, the chips are fixed together by curing the adhesive at a lower T_{re} ($<$180°C) [209]. NCA flip-chip bonding enables lower T_{re} and shorter bump pitch, but suffers from high thermal expansion coefficients, humidity absorption, and polymer trapping between the under bump metallization and solder [206, 209].

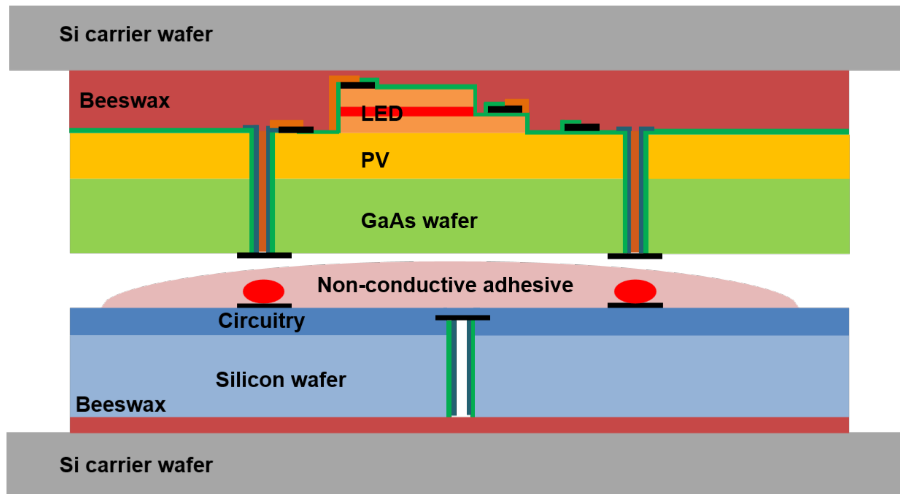

Figure 7.2: Schematic of flip-chip bonding using a non-conductive adhesive.

7.2.2 Mote Singulation

After bonding the chips, the motes must be singulated. Previous attempts at mechanically dicing 150 μm thick Si test motes resulted in ≈20% die loss and significant chipping at the mote edges, as shown in Figure 7.3. These non-idealities are expected to worsen for the complicated chip stack in Figure 7.2. Though the actual CMOS circuits have a built-in crack stop, the PV/LED chip does not. A less stressful dicing process is needed to avoid catastrophic failure during singulation.

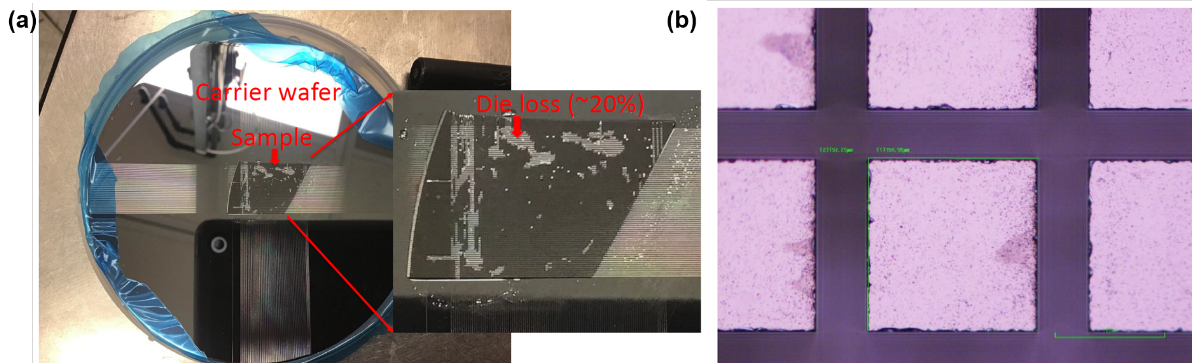

Figure 7.3: Mechanically diced Si test motes. a) Photograph showing ≈20% die loss. b) Optical micrograph of diced test motes. Figures courtesy of Eunseong Moon.

Figure 7.4 depicts a schematic for singulating the motes via etching. A combination of wet and dry etching processes can theoretically etch each of the diverse materials in the assembly. Table 7.1 outlines the proposed etching strategy. As shown in Figure 7.5, plasma dicing produces much smoother edges and reduces die loss (not shown). While successful for bulk Si pieces, this

technique has not been tried on the full chip stack. In addition, photolithography has not been attempted on bonded chips. Though plasma etching induces thermal stress, this is mitigated by breaking long etch steps into several shorter ones. Nevertheless, the etching scheme may present a viable alternative to the stresses of mechanical dicing.

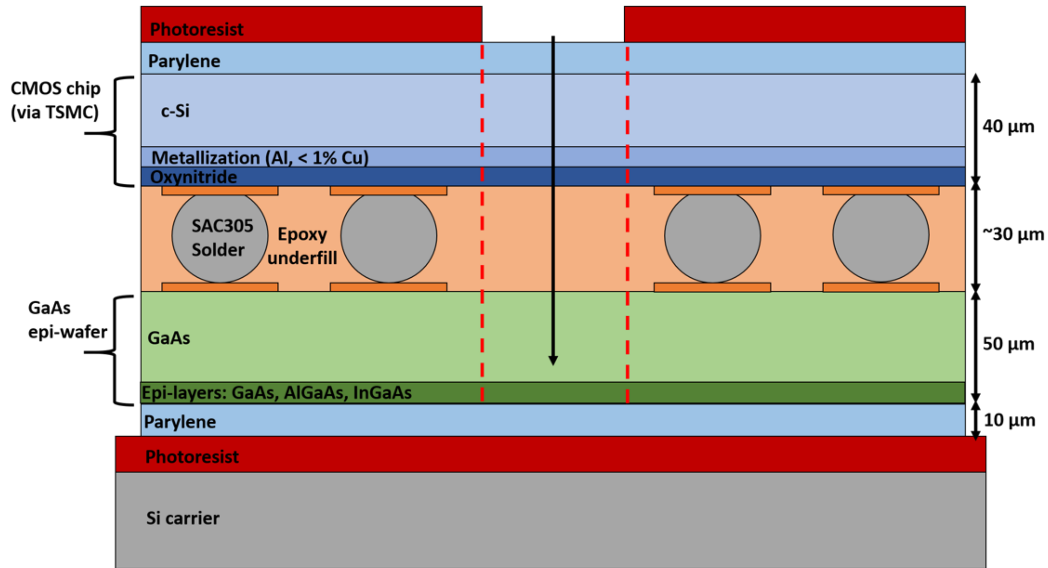

Figure 7.4: Schematic of the proposed plasma dicing scheme.

Layer name	Material(s)	Wet / Dry	Etchant
Parylene	parylene C	dry	O_2
c-Si	c-Si	dry	SF_6
Metallization	Al (low Cu %)	wet	BHF
Oxynitride	SiO_xN_y	wet	BHF
Epoxy underfill	epoxy	dry	O_2
GaAs	GaAs	dry	HBr
Epi-layers	GaAs, AlGaAs, InGaAs	dry	HBr
Parylene	parylene C	dry	O_2

Table 7.1: Proposed etching techniques to singulate the motes without mechanical dicing.

7.2.3 Carbon Fiber Probe Insertion

To assess the feasibility of inserting carbon fiber probes into the blind vias, test structures were fabricated on a 350 µm thick Si wafer. After coating one side of the wafer with 7 µm thick parylene, through-wafer via holes and dicing trenches are etched into the other surface using switched

deep reactive ion etching (described in Appendix A.3). The vias are coated in a 100 Å layer of conductive TiN via plasma-assisted atomic layer deposition. Each mote has a 50x50 μm^2 Ti/Au contact pad to evaluate the carbon fiber's electrical connection. The test motes are shown in Figure 7.5 after plasma dicing. As shown in Figure 7.6a, it is possible to individually insert carbon fiber probes by hand. A 3×2 array of test motes are inserted with carbon fiber probes and mounted to an insertion rig using a putty. The array was successfully implanted into a in vivo rat brain (not shown; performed by Joseph Letner). As a key component of the mote assembly, further process development is required for full heterogeneous integration. The carbon fiber probe must be interfaced with the CMOS blind via, sharpened for insertion, seamlessly encapsulated with the rest of the mote, and functionalized at the tip with PtIr.

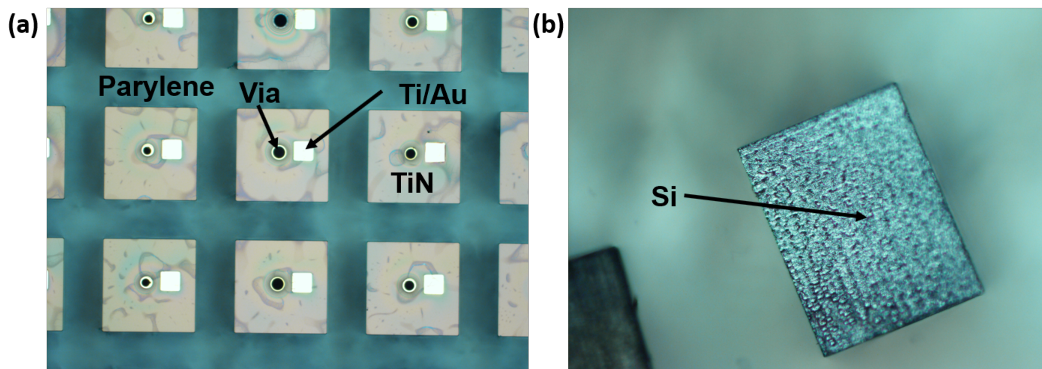

Figure 7.5: Optical micrographs of a) Si test motes singulated via switched reactive ion etching and b) a Si test mote tipped on its side showing sidewall profile.

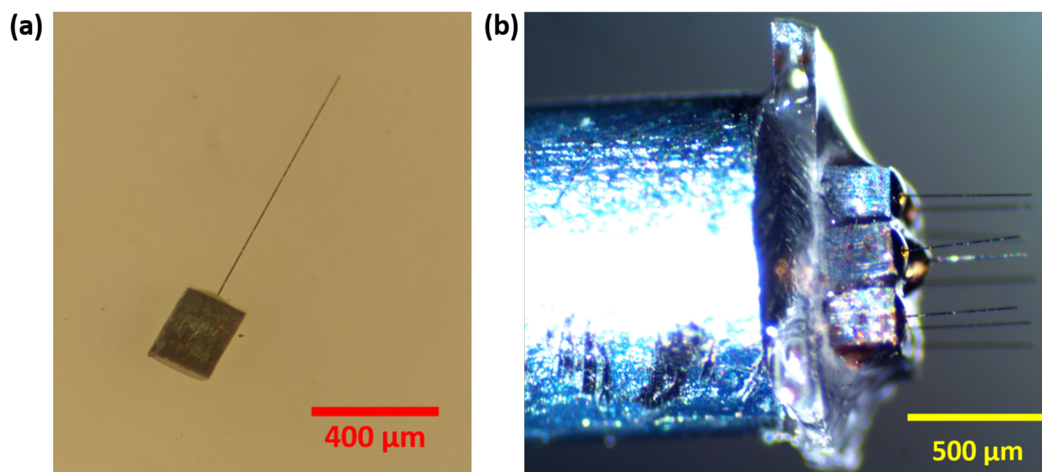

Figure 7.6: a) A Si test mote inserted with a carbon fiber probe. b) A 3×2 array of Si test motes inserted with carbon fiber probes and mounted to an insertion rig with a putty. (Figures courtesy of Joey Letner).

7.2.4 Mote Encapsulation

Encapsulation is a pressing question for chronically-implanted neural dust. A high-quality hermetic seal prevents toxic chemicals from entering brain tissue, and conversely extends the lifetime of the motes by keeping the electronics dry. The schematic in Figure 6.1 depicts a parylene encapsulation. Parylene has many attractive properties, such as biocompatibility, flexibility, and high conformality. However, parylene consistently cracks after months of implantation [210, 211]. For chronic implantation, encapsulation layers should withstand the brain's saline environment for years. Bilayer approaches, such as parylene C and ALD Al_2O_3 [211] or ALD Al_2O_3 and ALD HfO_2 [212] may significantly extend the lifetime of implanted neural devices. Despite promising results on planar structures it is less clear how these bilayer films perform on more complicated topographies [202]. The problem requires innovative deposition technique, as even the most intrinsically robust films are subverted by poor conformality. This issue is mitigated by minimizing contact between the devices and the deposition stage, which can be accomplished, for example, by a specially designed mesh [212]. Multi-step depositions may also be a solution.

7.3 The "Last Millimeter" Gap of the Neural Dust Interface

A demonstration of NIR wireless data and power transfer under realistic operating conditions is an important step toward the realization of the neural dust system. Akin to the last kilometer problem in transportation and telecommunications, bridging the last millimeter between the motes and an external detector is a technological challenge. Reference [87] demonstrates full end-to-end functionality for a PV/LED chip integrated with a CMOS neural recording chip. Using the optical setup in Figure 5.5, the Y-probe is aligned ≈2 mm above the μLED. An 850 nm illuminates the PV cell with a 150 μW/mm^2 optical intensity, which is well below the 190 μW/mm^2 exposure limit. The PV cell delivers 1.5 μW at 1.35 V, meeting the continuous power requirements of the CMOS IC (0.73 μW and 0.9-1.5 V). As shown in Figure 7.7, an input neural signal triggers a sequence of LED pulses, which are in turn detected by the SPAD via the Y-probe optical setup. When decoded, the SPAD output signal identifies the LED trigger events with a $>$99% detection rate. As indicated by the Monte Carlo calculations for NIR propagation, the expected optical link has -30 dB power attenuation, which is less lossy than the Y-probe setup (-41.3 dB). Going forward, wireless power and data transfer remains unproven for implanted motes, though the demonstration in [87] lends confidence.

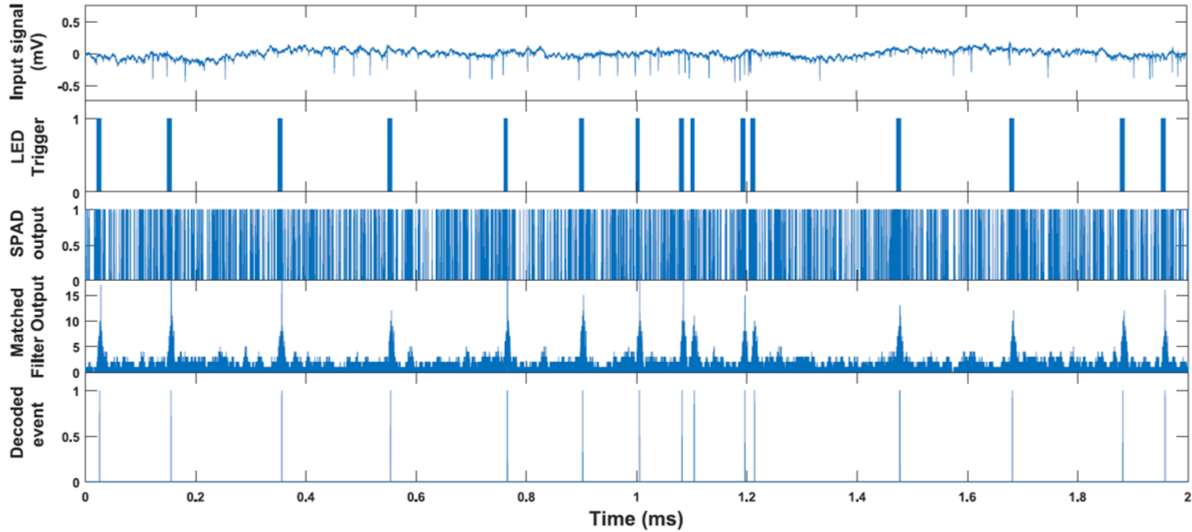

Figure 7.7: Demonstration of end-to-end recording, beginning with an input neural signal and ending with decoded neural events. Figure is referenced from [87].

The Y-probe optical setup is a useful test platform but is unsuitable for the simultaneous detection of a large ensemble of motes. Ultimately, a repeater unit will be placed beneath the skull to inductively relay detected neural signals from the motes to external electronics. Key components in the repeater unit include a pixelated SPAD array for mote detection, integrated µLEDs to power implanted motes, and inductive coils for wireless power and communication. To develop this system, an intermediate goal is to image multiple µLEDs using a SPAD camera, such as the 64x32 pixel SPC^3 available from Micro Photon Devices [178]. The ideal camera reliably detects simultaneously pulsing motes and is resilient to crosstalk.

7.4 Enhancing LED Light Extraction Efficiency

The InGaAs/GaAs µLEDs in Chapter V exhibit 2.5% experimental EQE compared to a 90% calculated IQE. Temperature-dependent photoluminescence experiments confirm high epitaxial growth quality, suggesting that poor light extraction efficiency (LEE) is responsible for this disparity. In planar LED structures, reflection at the semiconductor/air interface severely limits LEE, especially as the emission angle deviates from perpendicular incidence.

All LEE enhancement strategies possess the same goal: improve phase matching between the optical states in the semiconductor and those in the low index cover material. The chief techniques are surface texturization and mode manipulation. Surface texture increases the probability that an emitted photon impinges below the critical angle and allows more opportunities for light to escape via multiple reflections [213–215]. Alternatively, periodic structures can also remedy interfacial

momentum and energy mismatch. Example devices include photonic crystals (such as the SWG structures in Chapters II-IV) [216,217] and plasmonic nanostructures [218]. Periodic texturization may also alter the local density of states, increasing the LED emission rate via the Purcell effect [219].

Random surface texturization is an effective yet practical LEE enhancement strategy. Roughening techniques include chemical roughening [215] and colloidal lithographic masks [213]. In Reference [213], close-packed colloidal polystyrene spheres create a randomly textured mask that is transferable to the LED via dry etching. Using 400 nm wide spheres with a 200 nm etch depth, $\approx 4\times$ extraction enhancement was observed [213]. This result is understandable via simple geometric optics, where emitted light is more likely to impinge below the critical angle.

In Figure 7.8, full-wave calculations (via finite element methods) estimate LEE enhancement for several pseudorandom surface textures. The simulated structure consists of a textured GaAs substrate, an air cover layer, and a radiating dipole point source. The LEE enhancement is defined relative to the emission profile of a similar planar structure. Figure 7.8a shows the extraction enhancement for seven textures, demonstrating consistent improvement for all patterns and dipole orientations. Though seven measurements are insufficient to establish full Monte Carlo analysis, these calculations show the promise of using texturization to boost NIR LED LEE.

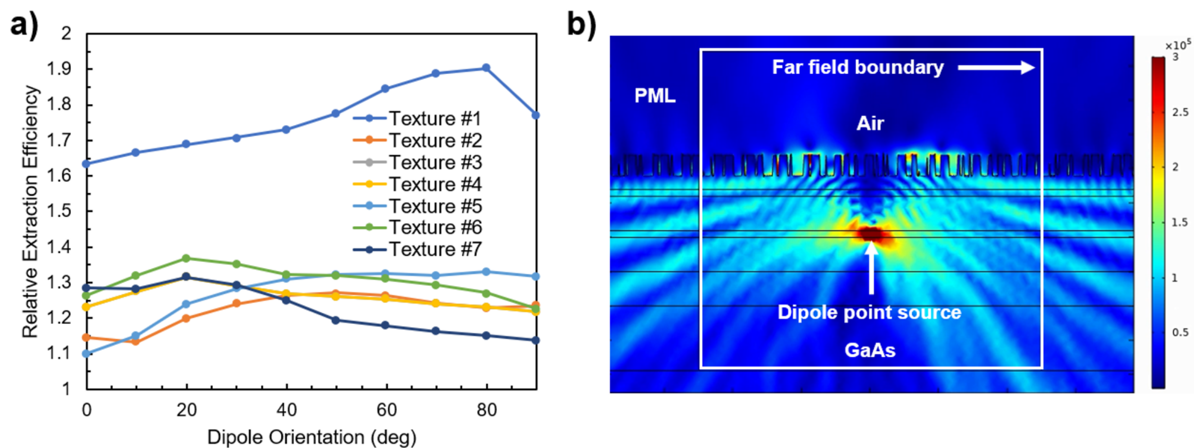

Figure 7.8: a) Calculated LEE enhancement for several pseudorandom surface textures. Enhancement is relative to the unpatterned, planar structure. b) E-field radiation pattern of textured GaAs LED with “Texture 1”. The texture depth is 200 nm and the dipole radiates at 1000 nm.

7.5 Conclusions

As with the decades-long miniaturization enjoyed by the microelectronics industry, optical systems are rapidly scaling to the microscale. This dissertation introduced a diverse group of studies to

advance the capabilities of microscale infrared (IR) technologies. The reduced scale makes almost every phase of the engineering process more difficult (design, fabrication, characterization, etc.). The presented works addressed each of these considerations, experimentally demonstrating novel subwavelength grating (SWG) filters and important developments for wireless neural devices.

Chapter II presented a background on SWG filters, lending insight into the fundamental physics of these surprising structures. An experimental study on zero-contrast grating transmittance filters observed quality factors (Q) exceeding 150, some of the highest reported for SWGs in the mid-wave IR (MWIR). Innovations in fabrication and characterization technique enabled these findings. By extending the SWG filters into gratings periodic in two directions, a polarization-independent optical response was confirmed. Finally, the effects of finite grating periodicity were empirically clarified. A SWG bounded by gold reflectors was proposed to mitigate these deleterious effects. This latter study is of keen importance for microscale devices.

The SWG filter technology was translated from the Si platform in Chapter II to the GaAs material system in Chapter III. Epitaxially growing GaAs and AlGaAs layers on a GaAs substrate presented two advantages. First, the epitaxial layers were grown to device thickness with minimal variation. Second, the availability of highly selective etch chemistries allowed easy release of suspended GaAs structures. This study found comparable filter performance to other material systems in the MWIR, with > 50 Q and $> 50\%$ transmission efficiency. These filters promise monolithic integration with other III-V optical devices, such as lasers and photodetectors.

Chapter IV gave an in-depth study into bound states in the continuum (BIC) in SWGs. High symmetry SWG geometries prohibit access to infinite lifetime grating modes. An asymmetric ”two-step” grating broke this symmetry-protection, enabling high-Q coupling to quasi-BICs at normal incidence. The theoretical effects of symmetry-breaking were experimentally confirmed by fabricating two-step SWGs with varying degrees of asymmetry. Fano resonance analysis lent additional insight into quasi-BIC coupling, revealing a trade-off between Q and transmission efficiency. In another study, a reduced symmetry hexagonal grating enabled fully polarization-independent access to symmetry-protected modes at normal incidence. Design and analysis was bolstered by analyzing diffraction efficiency symmetries.

To determine the detectability of implanted wireless neural recorders, Chapter V studied near IR (NIR) emission and propagation in subcranial tissue. Monte Carlo scattering simulations accounted for random scattering and absorption in turbid materials such as dura tissue and cerebrospinal fluid. For a neural mote positioned 1 mm from a 200 µm wide detector, the calculated link efficiency was $\approx 0.1\%$. An optical setup was presented to simultaneously provide a power downlink at 850 nm and a communication uplink at 1000 nm. A Y-shaped reflectance probe and single photon avalanche photodetector enabled $>99\%$ pulse detection efficiency at a safe optical intensity. This work is a milestone on the path toward >1000 channel systems.

Chapter VI presented innovative fabrication strategies to realize wireless neural motes. The hybrid integration of GaAs-based optoelectronic devices and Si CMOS integrated circuits prompted extensive process development. Key achievements included conductive GaAs through-wafer vias (TWV), blind Si vias for carbon fiber probe insertion, and progress toward bonding two thinned ($<$50 μm) heterogeneous chips. An evaporated dielectric plating mask enabled copper-infilled GaAs TWVs without overburden or the use of destructive chemical mechanical polishing. Series resistances as low as 1.4 Ω were recorded. For the blind Si probe vias, a self-aligned parylene etch mask allowed sub-kΩ connection to a buried metal contact and GΩ substrate isolation. Lastly, developments in thinned wafer mounting, solder bump jetting, and flip chip bonding represented progress toward fully assembled neural motes.

This dissertation concluded with several proposed studies to further advance IR microscale technologies. Before in vivo experiments may be considered, the neural motes require significant development, particularly in the fabrication process flow and system-level detection scheme. Chapter VII outlined a path toward full heterogeneous integration, mote singulation, encapsulation, and carbon fiber probe insertion. Strategies to detect an ensemble of implanted modes were also suggested. A SWG-integrated hyperspectral imager was a natural culmination of the work presented in Chapters II-IV. While hyperspectral imaging is a focal point, the high-Q SWG filters are also intriguing structures for any application requiring narrow linewidth or high field enhancement, such as biosensors, optical absorbers, nonlinear devices, and optical phased arrays.

APPENDIX A

Fabrication Process Details

A.1 GaAs Etch Development for Shallow Optical Structures

GaAs is an important material in this dissertation and IR devices generally. Many GaAs structures require controlled, anisotropic etch profiles. Examples include suspended optical structures (Chapter III), through-wafer vias (Chapter VI), LED surface texture (Chapter VII), and nanoelements for flat optics technologies. The various applications have different considerations such as etch rate, sidewall smoothness, anisotropy, and selectivity to etch mask and etch stop materials. With the appropriate parameter adjustments, an HBr-based inductively-coupled plasma reactive ion etch (ICP) meets all of these needs. Chapters III and VII describe the etch details for suspended gratings and through-wafer vias, respectively.

While not investigated in this dissertation, metalenses and other flat optical structures also motivate GaAs etch development. Tuning a nanoelement's optical phase shift requires precise thickness control. Rather than timing the etch depth, high etch stop selectivity simplifies the proposition since the etch rate plummets when the target depth is reached. To ensure the fidelity of the nanoelement dimensions, the etch must have minimal undercut and be highly selective to an AlGaAs etch stop. To obtain high selectivity between GaAs and $Al_{0.2}Ga_{0.8}As$, Reference [134] introduced an ICP process containing BCl_3 and SF_6. The SF_6 forms AlF_x groups with AlGaAs, inhibiting the chemical etch component at the etch stop. Figure A.1 repeats this experiment with a similar process to Reference [134]. The process parameters in Figure A.1 are 400 W ICP power, 7 mtorr chamber pressure, 45 sccm BCl_3, 45 sccm He flow, and 8 sccm SF_6 flow. Though GaAs:$Al_{0.2}Ga_{0.8}As$ selectivity is as high as 22:1, Figure A.1b shows significant undercut.

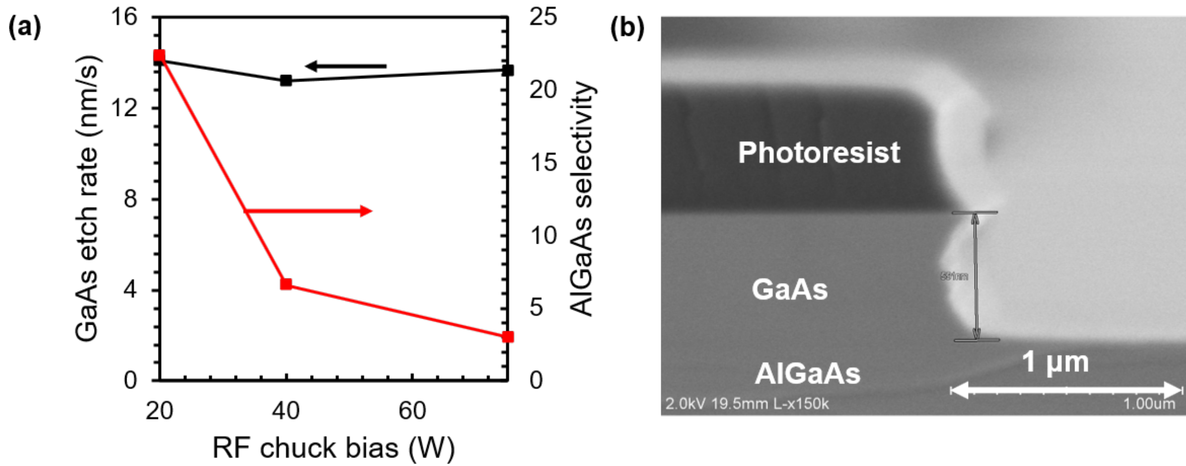

Figure A.1: a) GaAs etch rate and $Al_{0.2}Ga_{0.8}As$ for varying RF chuck power. b) SEM cross-section for the 40 W point in (a).

An HBr ICP process reduces undercut by passivating the sidewalls with a Si-containing polymer, as was shown in Sections III.3 and VI.2. The process parameters are 600 W ICP power, 30 mtorr chamber pressure, 100 sccm HBr flow, 20 sccm SF_6 flow, and 100 sccm He flow. Figure A.2 shows SEM cross-sectional images for structures with varying aspect ratio (AR). Low AR trenches, such as the 3000 nm gratings in (a, e) and the isolated lines in (d, h) exhibit high sidewall verticality, whereas the high AR trenches experience significant undercut. Transport limitation prevents passivation in the deep, high AR trenches. Accordingly, this etch is better suited for isolated features (such as metalens nanolements) rather than high AR gratings.

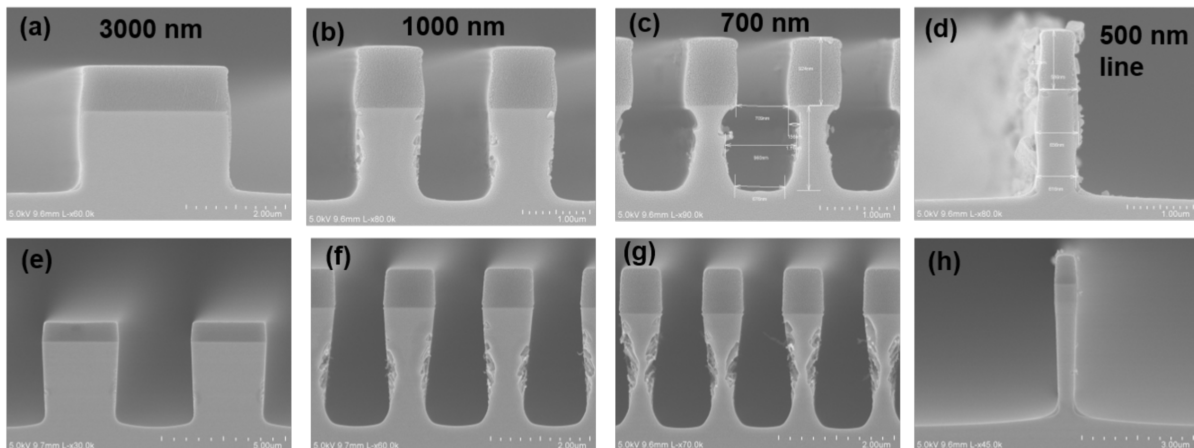

Figure A.2: SEM cross-sections showing dependence of sidewall quality on feature size. Figures (a-c) and (e-g) are patterned with 1D rectangular gratings with nominal periods of (a,d) 3000 nm, (b,c) 1000 nm, and (c,g) 700 nm with a 50% nominal duty cycle. (d) and (h) show isolated 500 nm lines. The RF chuck power is (a-d) 50 W and (e-h) 120 W.

As shown in Figure A.3a, the GaAs:$Al_{0.2}Ga_{0.8}As$ selectivity exceeds 160:1 at 50 W RF chuck bias. The GaAs:$Al_{0.2}Ga_{0.8}As$ and GaAs:photoresist(SPR) selectivities monotonically decrease with bias, while the GaAs etch rate only modestly increases. This suggests that the GaAs etch rate is limited by the density of charged ions rather than the physical bombardment energy. In this case, raising the chamber pressure may increase etch rates at the expense of sidewall quality [135]. The 50 W bias gives enough energy to remove volatile GaAs byproducts but not enough to sputter significant amounts of AlF_x. This leads to the very high observed selectivity. As the bias increases, the physical component of the AlF_x etch increases while the GaAs rate remains roughly the same. A similar effect occurs with the GaAs:SPR selectivity. At higher bias the physical etch component dominates the chemical component and the process loses selectivity. Figure A.3b shows the dependencies on the SF_6 flow rate. As expected, since AlF_x cannot form without SF_6, selectivity is lost at 0 sccm SF_6. For a constant pressure, introducing SF_6 displaces HBr, causing the GaAs etch rate to decrease at higher SF_6 flow rates. The severe reduction in GaAs etch rate at 30 sccm SF_6 may be due to the formation of a nonvolatile GaF_x layer.

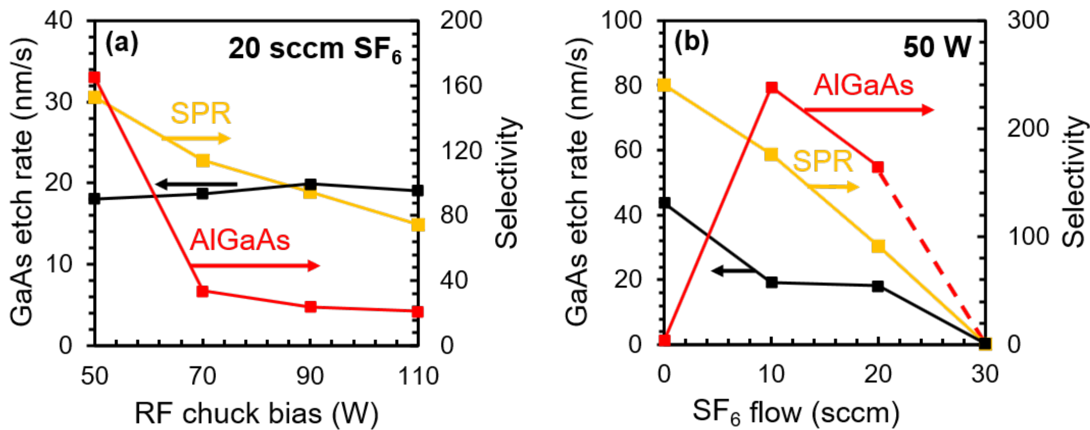

Figure A.3: GaAs etch rate and selectivity to $Al_{0.2}Ga_{0.8}As$ and photoresist (SPR) for varying a) RF chuck bias and b) SF_6 flow rate. The AlGaAs selectivity is unmeasurable at 30 sccm SF_6 flow.

A.2 GaAs Through-Wafer Vias

Figure A.4 depicts the process flow for the thin film TWV, which has considerable overlap with the CMP-less processes in Figures A.6 and A.7. To minimize the waste of epitaxially grown material, process validation is performed on 50 mm single-crystal (100) GaAs substrates (AXT Inc.). The wafer is first stripped of organic residues with a high power oxygen plasma (150°C chuck temperature, 800 W RF power, 80 sccm O_2 flow, 180 s). In step (b) of Figure A.4, positive photoresist (PR) is spin-coated to a thickness of ≈3 µm (MEGAPOSIT SPR 220). A 90 s soft-bake

at 115°C evaporates solvents in the PR. Using h-line contact lithography, the PR mask is exposed with 15-35 μm wide circular and rectangular TWVs, 100 μm long slot vias, dicing trenches, and alignment marks. The wafers are again placed on a hot plate at 115°C for 90 s, followed by an 80 s development in AZ 726 MIF (MicroChemicals). A short, low power oxygen descum strips any undeveloped PR (60°C chuck temperature, 100 W RF power, 35 sccm O_2 flow, 20 s). Next, the wafer is mounted to a 150 mm Si carrier wafer using a thermally conductive diffusion oil.

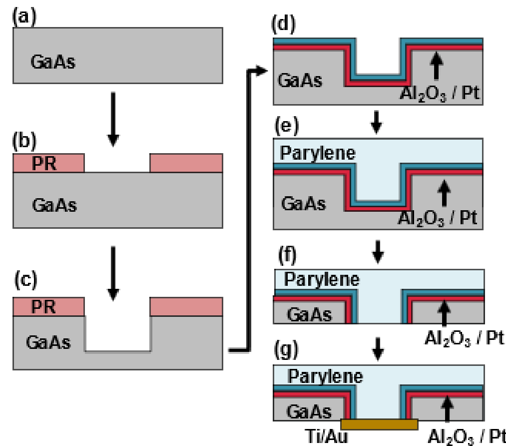

Figure A.4: Fabrication process flow for the thin film GaAs TWVs.

Step (c) depicts the ICP-RIE step. Prior to the main etch, a short breakthrough step removes native oxides. The breakthrough step parameters are 5 mtorr chamber pressure, 300 W ICP coil power, 100 W RF power, and 60 sccm Cl_2 flow. The parameters for the main etch step are 30 mtorr chamber pressure, 600 W ICP coil power, 90 W RF power, 100 sccm HBr flow, and 100 sccm He flow. Etching is performed using a LAM 9400 SE (LAM Research Corporation). Following the etch step, the mounted wafer is placed in acetone at 65°C to safely dismount from the carrier. Acetone residue is removed by a dip in isopropyl alcohol dip (IPA) followed by a rinse in deionized water (DI). To remove the Si-containing passivation layer, the wafer is placed in a buffered hydrofluoric (BHF) acid solution for 5 min then rinsed in DI. Finally, organic residue is stripped with another high power oxygen plasma treatment for 180 s. In step (d), 300 Å of Al_2O_3 are deposited at 200°C via thermal atomic layer deposition (ALD) (Cambridge Nanotech Fiji). Next a 100 Å layer of TiN(or Pt) is deposited at 250(200)°C via plasma-assisted ALD. In step (f), the wafer is backgrinded to 50 μm, which is a precarious state for a brittle material like GaAs. To infill the TWVs, protect the surface during thinning, and provide structural support for the thinned substrate, step (e) deposits a 7 μm thick layer of parylene C (Speciality Coating Systems, PDS 2035 CR) with adhesion promoter. After parylene deposition, the wafer is mounted to dicing tape, backgrinded to 50 μm, and given a 4000 grit polish (performed by Integra Technologies, Wichita,

KS).

Post-thinning, the wafer is removed from dicing tape by first applying Crystalbond 555 wax (Aremco) to a Si carrier wafer, heating the adhesive to 80°C on a hot plate and spreading over an area larger than the thinned wafer. Next, the thinned wafer is placed on the Crystalbond adhesive and removed from the hot plate. Figure A.5a shows this step of the process. From the bottom-up, the stack consists of a 4” Si carrier wafer, Crystalbond 555 wax, a thinned 3” Si wafer containing test chips, and the dicing tape on a metal frame. Now that the thinned wafer is glued to the carrier, the tape may be carefully pealed from the carrier and thinned wafer, leaving the thinned GaAs wafer face-up on the carrier as shown in Figure A.5b. The thinned GaAs wafer is removed from the carrier by submerging the wafer in DI at 85°C until the samples debond. The PR pattern in step (b) includes dicing trenches that are partially etched into the wafer during step (c). After thinning, multiple samples on one wafer are automatically singulated during the hot DI release step. As shown in Figure A.5c, the thinned samples are then mounted backside-up on Si carrier wafers using a 10 µm layer of PR (SPR 220) as an adhesive. A lift-off PR (LOR-B, MICROCHEM) and SPR 220 are spin-coated on the samples. A pattern containing 50 µm wide contact pads is aligned to the TWVs, followed by the standard contact lithography steps detailed in the first paragraph of this section. 10 nm of Ti and 500 nm of Au are deposited via magnetron sputtering. Lastly, a 15 min soak in Remover PG at 65°C facilitates lift-off and completes the backside contact pad fabrication.

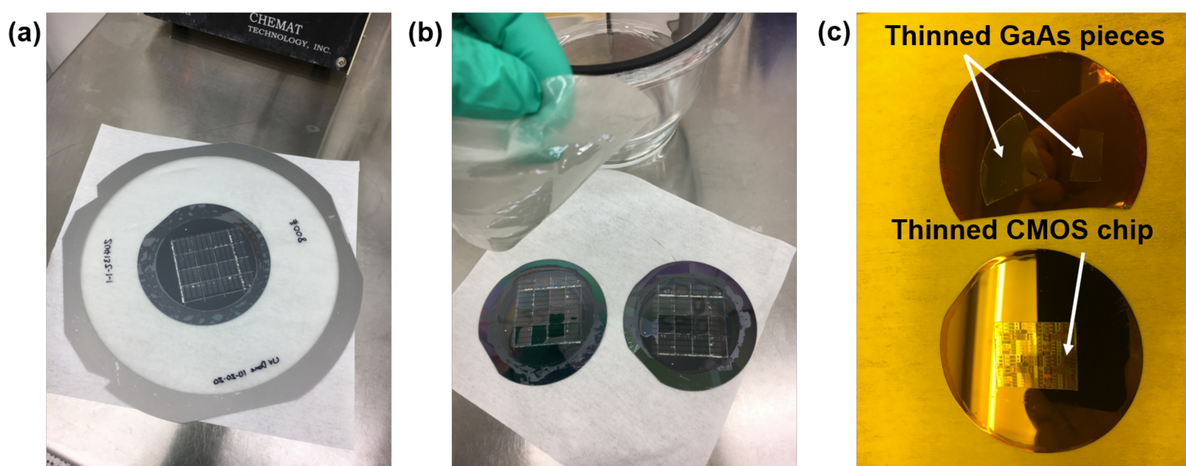

Figure A.5: a) Photo of the tape removal process for a thinned Si wafer. b) Two thinned 3” Si wafers mounted to 4” carrier wafers after tape removal. c) Thinned sample mounting using thick SPR 220 photoresist.

The seed layer patterning technique in Figure A.6 follows Figure A.4 through step (d). After depositing ALD Al_2O_3 and Pt, the seed layer pattern is defined in a PR etch mask using standard contact lithography. In step (a) an ion mill (Intlvac Nanoquest II) removes the Pt layer, while a sec-

ondary ion mass spectrometer monitors the sputtered Pt and Al concentrations to ensure minimal overetch into Al_2O_3. The PR mask is then stripped in a high power oxygen plasma. The Cu ECD process in step (b) is performed in a commercially-available additive-free plating solution (Copper Plating Acid Type, Transene), containing copper sulfate and sulfuric acid. The plating solution is maintained at approximately room temperature (≈21°C), agitated at 220 rpm, and continually filtered. The power supply anode is connected to a Cu sheet, while the cathode is clipped to the GaAs sample, providing a low resistance path to the Pt seed layer. The pulse timing is t_{fwd} = 5 ms and t_{off} = 50 ms, with an approximate forward current density of 10 mA/cm^2. The plating time is 55 min. Steps (c-e) are the same as in Figure A.4.

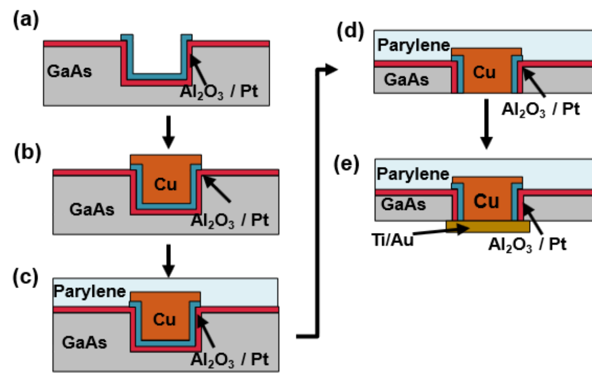

Figure A.6: Fabrication process flow for the selective seed layer patterning technique.

In the selective damascene technique in Figure A.7, after ALD a 300 nm thick layer of TiO_2 is deposited via electron beam evaporation (Angstrom Engineering, Evovac). An SiO_2 film was also investigated, but it exhibited a high defect density after Cu ECD. The ECD plating setup is identical to that of the seed layer patterning technique in Figure A.6. The current densities and timing parameters are given in Table 6.1. After plating, the TiO_2 is removed by a 5 min dip in BHF, and the Pt layer is etched with an ion mill. Steps (c-e) are the same as in Figure A.4.

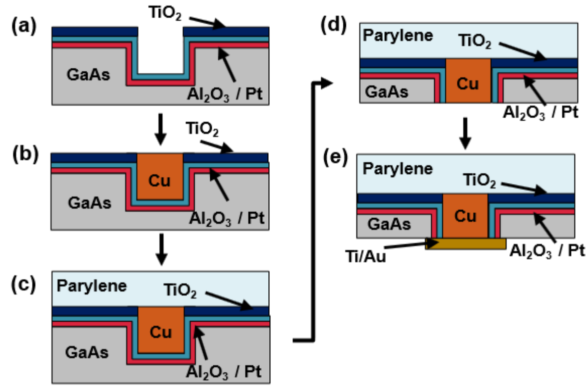

Figure A.7: Fabrication process flow for the selective damascene plating technique.

Though the studies in Chapter VI are performed on a bulk GaAs substrate, the GaAs TWV fabrication techniques are compatible with the greater PV/LED process flow. As shown in Figure A.8, TWVs fabricated on the epitaxially-grown PV/LED structure minimally effect device performance. The output current drop is primarily related to the loss of PV active area and sidewall recombination at the TWVs.

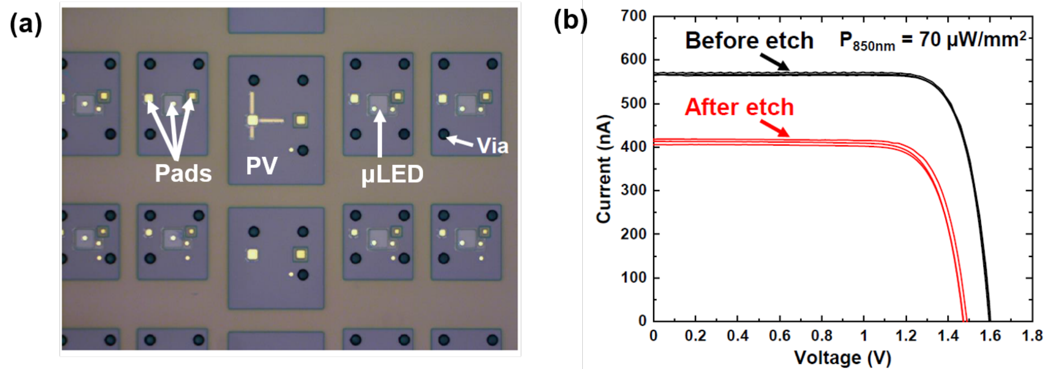

Figure A.8: Optical micrograph of an array of PV/LED cells for the neural motes, showing successful integration with the GaAs TWV flow in Figure A.7. (Figures from Eunseong Moon)

A.3 Si Blind Vias for Probe Insertion

Via test structures are fabricated on a 3" p-type (100) Si wafer with 0-100 Ω resistivity. The wafer is first cleaned in acetone at room temperature, then successively rinsed in IPA and DI. A high power oxygen plasma strips the surface of organic residue (150°C, 800 W RF power, 80 sccm O_2 flow, 180 s). Next, SPR 220 positive photoresist is spin-coated and baked at 115°C for 90 s. A through-wafer alignment mark pattern is exposed into the PR using h-line contact photolithography, then

baked at 115°C for 90 s and developed for 80 s in AZ 726. Next, the wafer is mounted with a diffusion oil to a 4” Si carrier wafer containing 2 μm of thermally grown SiO_2. An inductively-coupled plasma reactive ion etch (ICP) tool (SPTS Technologies) etches ≈ 50 μm deep features using a switched Bosch process. The etch(deposition) cycle parameters are 2800(200) W ICP coil power, 60(0) W RF bias power, 30(24) mtorr chamber pressure, 30(250) sccm C_4F_8 flow, 390(0) sccm SF_6 flow, 39(0) sccm O_2 flow, 2.6(2) s, 20°C chuck temperature, and 10 min total duration. After another solvent and O_2 clean, a 300 Å layer of Al_2O_3 is deposited at 200°C via thermal ALD. This layer isolates the Al contacts from the substrate. Next, LOR-B lift-off resist and SPR 220 are spin-coated and baked at 165°C(for 180 s) and 115°C(for 90 s), respectively. A contact pad pattern is exposed using standard SPR 220 photolithography, and 500 nm of Al is deposited via a magnetron sputtering tool. A 15 min soak in Remover PG at 65°C facilitates lift-off, followed by another solvent and plasma clean. The wafer is then coated in 7 μm of parylene C, backgrinded to 40 μm, and given a 4000 grit polish.

The preceding process steps simulate a CMOS chip, as shown in Figure A.9a. After thinning, dicing tape is removed using the process described in Section 2. Trenches etched during the alignment mark etch step automatically singulate the wafer into 13×15 mm^2 pieces. Next another 5 μm layer of parylene C is coated on the backsides of the pieces. The thinned samples are then mounted backside-up on a 3” Si carrier wafer using a 10 μm layer of PR (SPR 220) as an adhesive. An extended 15 bake time (at 85°C) is required to evaporate the suspended solvents. Probe via holes are patterned into a PR mask using thick SPR 220 spin-coated at 1000 rpm and baked for 240 s at 115°C. Post-exposure, the sample is baked at 115°C for 120 s and developed in AZ 726 for 160 s. The via hole pattern is transferred into the parylene by an oxygen plasma etch (60°C, 800 W, 50 sccm O_2 flow, 9 min), as depicted in Figure A.9b. Notably, the parylene:SPR selectivity is $\approx$1:1. Next, the 3” Si carrier wafer is mounted to a 4” with a thermally conductive diffusion oil. In Figure A.9c, another use of the switched ICP process (18 min) etches via holes from the backside of the piece to the bottom of the topside Al contacts.

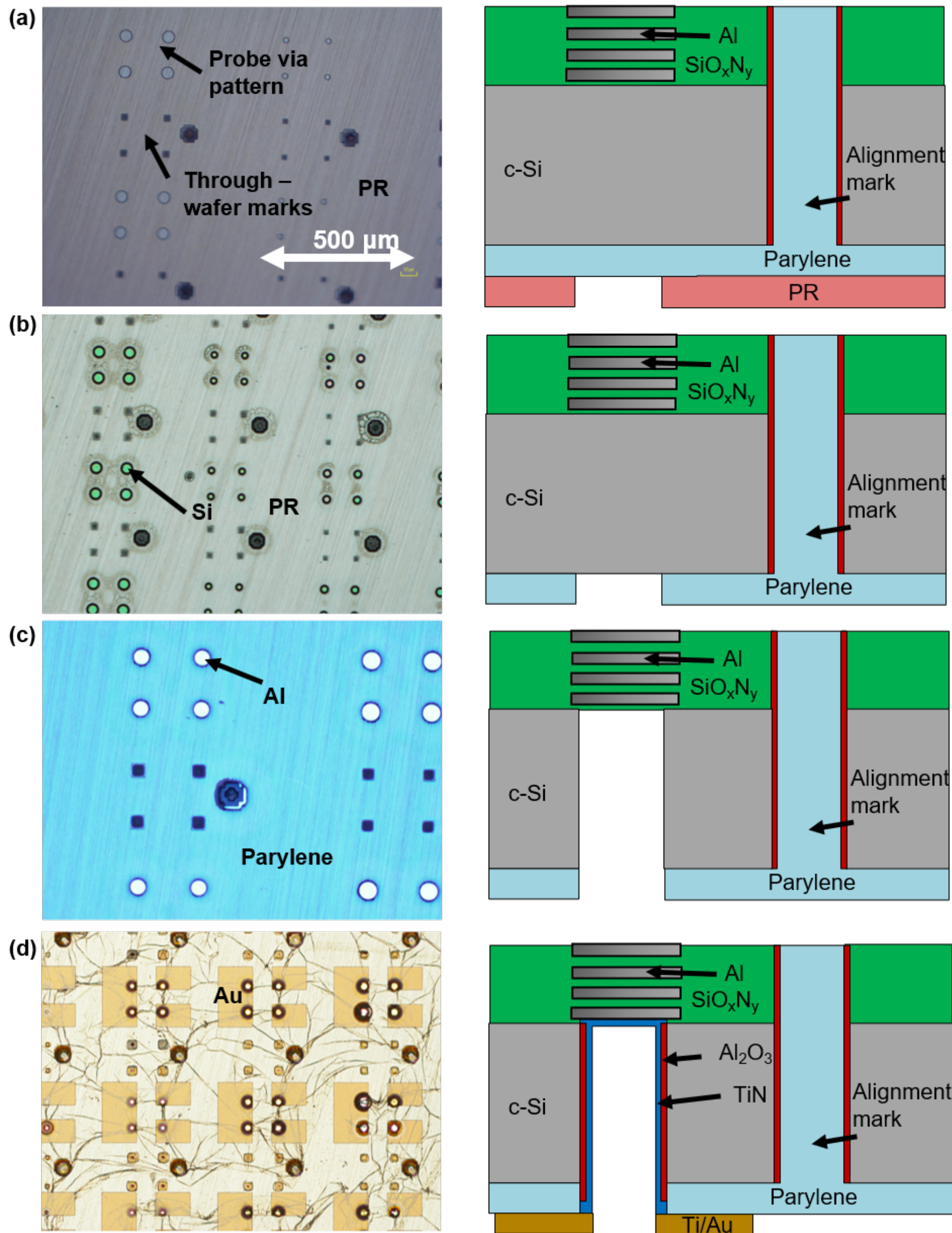

Figure A.9: Optical micrographs and schematics showing a) the PR mask for the parylene etch b) the parylene etch c) DRIE through the parylene mask into Si d) Au contacts for electrically characterizing the vias.

Since PR is incompatible with the high vacuum of ALD, the samples are demounted via an overnight soak in acetone. For the first step of Figure A.10d, a 300 Å layer of Al_2O_3 coats the sidewalls via 200°C thermal ALD. The samples are then remounted to Si carriers with thick SPR 220. The Al_2O_3 coating the buried Al contact is removed by another ICP process (600 W ICP coil

power, 50 W RF bias power, 5 mtorr chamber pressure, 25 sccm HBr flow, 25 sccm BCl_3 flow, and 160 s total duration). The samples are again demounted by an overnight acetone soak. Next, a 100 Å layer of TiN is deposited by plasma-assisted ALD at 250°C. To provide contact pads for electrical measurement, 500 nm Ti/Au contacts are fabricated via photolithography and lift-off, as shown in Figure A.9d. An ion mill removes the TiN between the contacts.

The preceding process flow is modified for the actual CMOS chip fabrication. After CMOS processing, the Al contact is already buried within the SiO_xN_y layer. Therefore the first step is to define the through-wafer alignment marks. A single etch mask must withstand both the SiO_xN_y and Si etch steps. A Si-containing hard mask will be rapidly etched by one of the etch steps, while a metal hard mask is incompatible with the etch tools. Thus, a 10 μm thick layer of SPR 220 (7.0) is spin-coated at 1500 rpm and baked for 600 s at 85°C. Exposure and development times are comparably increased. The ICP parameters for etching through the SiO_xN_y are 600 W ICP coil power, 50 W RF bias power, 5 mtorr chamber pressure, 25 sccm HBr flow, 25 sccm BCl_3 flow, and 160 s total duration. The Si etch uses the same switched Bosch process as the test structures in Figure A.9c. In Figure A.10a, alignment marks are aligned to the CMOS circuitry and etched ≈ 50 μm through the SiO_xN_y and into the Si. Figure A.10b shows a Si probe via etched through the Si from the backside of a thinned CMOS chip. When aligned to the through-wafer marks, the probe via holes are well-aligned to the buried Al layer near the top of the chip. Backside processing of the probe vias uses the same self-aligned parylene mask technique as the test structures. Fabrication is completed after the TiN deposition, as the motes do not require backside contact pads.

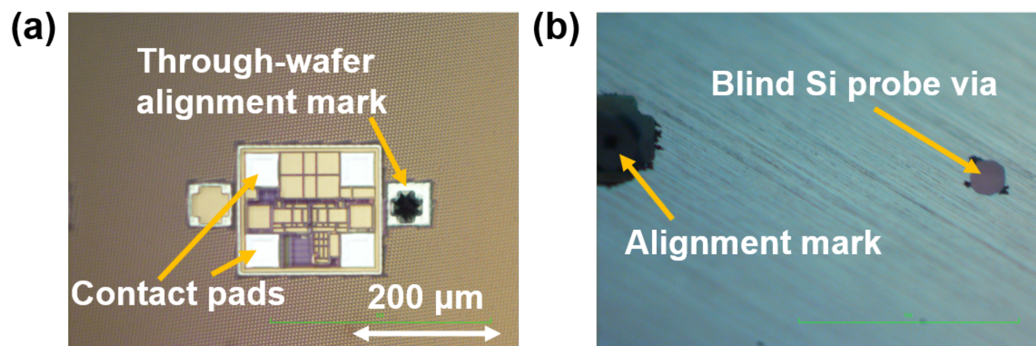

Figure A.10: Optical micrograph showing a) a through-wafer alignment mark within the CMOS mote circuitry and b) a blind Si probe via fabricated on the backside of a thinned CMOS chip.

A.4 Flip-Chip Bonding UBM

This section describes the fabrication process for the flip-chip bonding under bump metallization (UBM). A 500 Å Au seed layer coats the sample via a magnetron sputtering tool. A plating mask is

patterned by first spin-coating the wafer with 3 μm thick SPR 220 positive photoresist and baking at 115°C for 90 s. Next, the sample is exposed with h-line contact photolithography and baked again at 115°C for 90 s. The resist is then developed in AZ 726 for 80 s. The adhesion strength between Ni and the Au seed layer is greatly improved by introducing a plasma activation treatment before electroplating (300 mT base pressure, 300 W power, 50 sccm O_2 flow, 7 sccm Ar flow, 120 s duration, Glen Technologies Glen 1000p). Plasma treatment promotes adhesion by stripping organic contaminants, activating the Au surface by introducing chemical functional groups, and increasing the surface area of the bonding interface [220].

Nickel is electrochemically deposited in a solution containing nickel (II) sulfate ($NiSO_4(H_2O)_6$) and nickel sulfamate ($Ni(SO_3NH_2)_2$). The plating solution is maintained at 50°C, continuously filtered, and agitated at 220 rpm. A pulse plating program alternates between 1 ms of 20 mA/cm^2 anodic current density and 1 ms of zero bias, with a measured Ni deposition rate of $\approx$180 nm/min. The sample is then cleaned in acetone and IPA to remove the photoresist mask. A second 500 Å Au seed layer is sputtered to prevent Ni oxidation. Another iteration of photolithography patterns the Ni/Au bumps for excess Au removal. An ion mill removes the excess Au between the UBM, while the UBM is protected by the photoresist mask. Figure A.11(a, b) shows Ni/Au UBM before and after solder bump jetting and laser reflow. Figure A.11c shows Ni UBM fabricated on the backside of a thinned GaAs wafer, aligned above GaAs TWVs. This proves that the Ni/Au UBM fabrication process flow is amenable to thinned wafer processing.

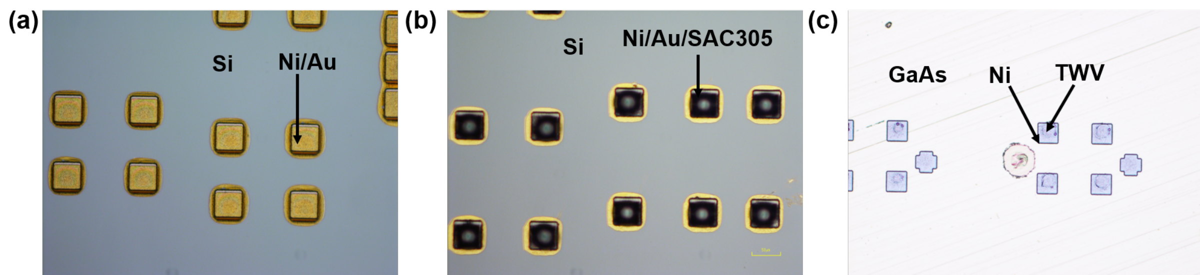

Figure A.11: Optical micrographs of a) Ni/Au UBM before solder bump jetting b) Ni/Au UBM after solder bump jetting and laser reflow and c) Ni UBM fabricated on the backside of a thinned GaAs wafer, aligned above GaAs TWVs.

BIBLIOGRAPHY

[1] G. W. Paltridge and C. M. R. Platt, *Radiative Processes in Meteorology and Climatology*. Elsevier, 1976.

[2] M. Ebermann, N. Neumann, K. Hiller, M. Seifert, M. Meinig, and S. Kurth, "Tunable MEMS Fabry-Pérot filters for infrared microspectrometers: A review," in *MOEMS and Miniaturized Systems XV*, vol. 9760, (San Francisco, CA), Mar. 2016.

[3] A. Hessel and A. A. Oliner, "A new theory of Wood's anomalies on optical gratings," *Appl. Opt.*, vol. 4, no. 10, pp. 1275–1297, 1965.

[4] L. Mashev and E. Popov, "Zero order anomaly of dielectric coated gratings," *Opt. Commun.*, vol. 55, pp. 377–380, Oct. 1985.

[5] S. S. Wang, R. Magnusson, and J. S. Bagby, "Guided-mode resonances in planar dielectric-layer diffraction gratings," *J. Opt. Soc. Am. A*, vol. 7, pp. 1470–1474, Aug. 1990.

[6] A. Sharon, D. Rosenblatt, A. A. Friesem, H. G. Weber, H. Engel, and R. Steingrueber, "Light modulation with resonant grating-waveguide structures," *Opt. Lett.*, vol. 21, no. 19, pp. 1564–1566, 1996.

[7] S. Peng and M. Morris, "Experimental demonstration of resonant anomalies in diffraction from two-dimensional gratings," *Opt. Lett.*, vol. 21, no. 8, pp. 549–551, 1996.

[8] A. Sharon, D. Rosenblatt, and A. A. Friesem, "Resonant grating-waveguide structures for visible and near-infrared radiation," *J. Opt. Soc. Am. A*, vol. 14, no. 11, pp. 2985–2993, 1997.

[9] D. L. Brundrett, E. N. Glytsis, and T. K. Gaylord, "Normal-incidence guided-mode resonant grating filters: design and experimental demonstration," *Opt. Lett.*, vol. 23, pp. 700–702, May 1998.

[10] R. Magnusson and S. S. Wang, "Transmission bandpass guided-mode resonance filters," *Appl. Opt.*, vol. 34, no. 35, pp. 8106–8109, 1995.

[11] S. Tibuleac and R. Magnusson, "Reflection and transmission guided-mode resonance filters," *J. Opt. Soc. Am. A*, vol. 14, pp. 1617–1626, July 1997.

[12] C. J. Chang-Hasnain and W. Yang, "High-contrast gratings for integrated optoelectronics," *Adv. Opt. Photonics*, vol. 4, pp. 379–440, Sept. 2012.

[13] J. Inoue, A. Tsuji, K. Kintaka, K. Nishio, and S. Ura, “Wavelength division multiplexer based on cavity-resonator-integrated guided-mode resonance filters for a compact multi-wavelength light source,” *Opt. Express*, vol. 26, no. 3, pp. 2212–2219, 2018.

[14] R. Zakirullin, “Grating optical filters for smart windows: materials, calculations and prospects,” *AIMS Mater. Sci.*, vol. 7, no. 6, pp. 720–771, 2020.

[15] M. Barrow, M. Scherr, and J. D. Phillips, “Influence of subwavelength grating asymmetry on long-wavelength infrared transmittance filters,” *IEEE Photonics J.*, vol. 10, p. 8, Dec. 2018.

[16] A. Liu, W. Zheng, and D. Bimberg, “Comparison between high- and zero-contrast gratings as VCSEL mirrors,” *Opt. Commun.*, vol. 389, pp. 35–41, 2017.

[17] P. Qiao, K. Li, K. T. Cook, and C. J. Chang-Hasnain, “MEMS-tunable VCSELs using 2D high-contrast gratings,” *Opt. Lett.*, vol. 42, pp. 823–826, Feb. 2017.

[18] H. Yan, L. Huang, X. Xu, S. Chakravarty, N. Tang, H. Tian, and R. T. Chen, “Unique surface sensing property and enhanced sensitivity in microring resonator biosensors based on subwavelength grating waveguides,” *Opt. Express*, vol. 24, pp. 29724–29733, Dec. 2016.

[19] E. Luan, H. Shoman, D. M. Ratner, K. C. Cheung, and L. Chrostowski, “Silicon photonic biosensors using label-free detection,” *Sensors*, vol. 18, no. 10, p. 42, 2018.

[20] G. Niederer, W. Nakagawa, H. P. Herzig, and H. Thiele, “Design and characterization of a tunable polarization-independent resonant grating filter,” *Opt. Express*, vol. 13, pp. 2196–2200, Mar. 2005.

[21] S. Hernandez, O. Gauthier-Lafaye, A.-L. Fehrembach, S. Bonnefont, P. Arguel, F. Lozes-Dupuy, and A. Sentenac, “High performance bi-dimensional resonant grating filter at 850 nm under high oblique incidence of ˜60,” *Appl. Phys. Lett.*, vol. 92, p. 3, Jan. 2008.

[22] D. W. Peters, R. R. Boye, J. R. Wendt, R. A. Kellogg, S. A. Kemme, T. R. Carter, and S. Samora, “Demonstration of polarization-independent resonant subwavelength grating filter arrays,” *Opt. Lett.*, vol. 35, pp. 3201–3203, Oct. 2010.

[23] A.-L. Fehrembach, O. Gauthier-Lafaye, K. C. S. Yu, A. Monmayrant, S. Bonnefont, E. Daran, P. Arguel, F. Lozes-Dupuy, and A. Sentenac, “Measurement and modeling of 2D hexagonal resonant-grating filter performance,” *J. Opt. Soc. Am. A*, vol. 27, pp. 1535–1540, July 2010.

[24] A.-L. Fehrembach, F. Lemarchand, A. Talneau, and A. Sentenac, “High Q polarization independent guided-mode resonance filter with ”doubly periodic” etched Ta_2O_5 bidimensional grating,” *J. Light. Technol.*, vol. 28, pp. 2037–2044, July 2010.

[25] M. R. Saleem, D. Zheng, B. Bai, P. Stenberg, M. Kuittinen, S. Honkanen, and J. Turunen, “Replicable one-dimensional non-polarizing guided mode resonance gratings under normal incidence,” *Opt. Express*, vol. 20, pp. 16794–16800, July 2012.

[26] A. Monmayrant, S. Aouba, K. C. S. Yu, P. Arguel, A.-L. Fehrembach, A. Sentenac, and O. Gauthier-Lafaye, “Experimental demonstration of 1D crossed gratings for polarization-independent high-Q filtering,” *Opt. Lett.*, vol. 39, pp. 6038–6041, Oct. 2014.

[27] M. Niraula, J. W. Yoon, and R. Magnusson, “Single-layer optical bandpass filter technology,” *Opt. Lett.*, vol. 40, pp. 5062–5065, Nov. 2015.

[28] Y. H. Ko and R. Magnusson, “Flat-top bandpass filters enabled by cascaded resonant gratings,” *Opt. Lett.*, vol. 41, pp. 4704–4707, Oct. 2016.

[29] Y. H. Ko, M. Niraula, and R. Magnusson, “Divergence-tolerant resonant bandpass filters,” *Opt. Lett.*, vol. 41, pp. 3305–3308, July 2016.

[30] B. Sheng, H. Zhou, C. Tao, A. Zahid, Z. Ni, Y. Huang, R. Hong, and D. Zhang, “Tunable and polarization-independent wedged resonance filter with 2D crossed grating,” *IEEE Photonic. Tech. L.*, vol. 28, pp. 2211–2214, Oct. 2016.

[31] A.-L. Fehrembach, K. Sharshavina, F. Lemarchand, E. Popov, A. Monmayrant, P. Arguel, and O. Gauthier-Lafaye, “$2 \times$ 1D crossed strongly modulated gratings for polarization independent tunable narrowband transmission filters,” *J. Opt. Soc. Am. A*, vol. 34, pp. 234–240, Feb. 2017.

[32] A.-L. Fehrembach, A. Talneau, O. Boyko, F. Lemarchand, and A. Sentenac, “Experimental demonstration of a narrowband, angular tolerant, polarization independent, doubly periodic resonant grating filter,” *Opt. Lett.*, vol. 32, pp. 2269–2271, Aug. 2007.

[33] W. Wang, X. Gao, X. Shen, Z. Shi, and Y. Wang, “Spectral responses of linear grating filters under full-conical incidence,” *Opt. Lett.*, vol. 43, pp. 391–394, Feb. 2018.

[34] L. Fan, K. Jia, and J. Ma, “Transmission filter controlled by incident conditions in single-layer waveguide grating structures,” *Appl. Opt.*, vol. 58, no. 31, pp. 8371–8375, 2019.

[35] R. C. Ng, J. C. Garcia, J. R. Greer, and K. T. Fountaine, “Polarization-independent, narrowband, near-IR spectral filters via guided mode resonances in ultrathin a-Si nanopillar arrays,” *ACS Photonics*, vol. 6, pp. 265–271, Jan. 2019.

[36] D. Wang, Q. Wang, and Z. Zhan, “Polarization-independent filter based on 2-D crossed grating under oblique incidence,” *IEEE Photonics J.*, vol. 10, p. 9, Sept. 2018.

[37] T. Clausnitzer, T. Kämpfe, E.-B. Kley, A. Tünnermann, U. Peschel, A. V. Tishchenko, and O. Parriaux, “An intelligible explanation of highly-efficient diffraction in deep dielectric rectangular transmission gratings,” *Opt. Express*, vol. 13, pp. 10448–10456, Dec. 2005.

[38] A.-L. Fehrembach and A. Sentenac, “Unpolarized narrow-band filtering with resonant gratings,” *Appl. Phys. Lett.*, vol. 86, p. 3, Mar. 2005.

[39] E. Sakat, G. Vincent, P. Ghenuche, N. Bardou, C. Dupuis, S. Collin, F. Pardo, R. Haïdar, and J.-L. Pelouard, “Free-standing guided-mode resonance band-pass filters: from 1D to 2D structures,” *Opt. Express*, vol. 20, pp. 13082–13090, May 2012.

[40] J. M. Foley, S. M. Young, and J. D. Phillips, "Narrowband mid-infrared transmission filtering of a single layer dielectric grating," *Appl. Phys. Lett.*, vol. 103, Aug. 2013.

[41] B. Hogan, S. P. Hegarty, L. Lewis, J. Romero-Vivas, T. J. Ochalski, and G. Huyet, "Realization of high-contrast gratings operating at 10 μm," *Opt. Lett.*, vol. 41, pp. 5130–5133, Nov. 2016.

[42] Y. Zhong, Z. Goldenfeld, K. Li, W. Streyer, L. Yu, L. Nordin, N. Murphy, and D. Wasserman, "Mid-wave infrared narrow bandwidth guided mode resonance notch filter," *Opt. Lett.*, vol. 42, pp. 223–226, Jan. 2017.

[43] M. Scherr, M. Barrow, and J. D. Phillips, "Long-wavelength infrared transmission filters via two-step subwavelength dielectric gratings," *Opt. Lett.*, vol. 42, pp. 518–521, Feb. 2017.

[44] L. Mace, O. Gauthier-Lafaye, A. Monmayrant, S. Calvez, H. Camon, and H. Leplan, "Highly-resonant two-polarization transmission guided-mode resonance filter," *AIP Adv.*, vol. 8, p. 7, Nov. 2018.

[45] J. Lee., V. Leung, A. H. Lee, J. Huang, P. Asbeck, P. P. Mercier, S. Shellhammer, L. Larson, F. Laiwalla, and A. Nurmikko, "Wireless ensembles of sub-mm microimplants communicating as a network near 1 GHz in a neural application," *bioRxiv*, 2020.

[46] A. S. L. Krishna, V. Mere, S. K. Selvaraja, and V. Raghunathan, "Polarization-independent angle-tolerant mid-infrared spectral resonance using amorphous germanium high contrast gratings for notch filtering application," *OSA Continuum*, vol. 3, pp. 1194–1203, May 2020.

[47] C. F. R. Mateus, M. C. Y. Huang, Y. Deng, A. R. Neureuther, and C. J. Chang-Hasnain, "Ultrabroadband mirror using low-index cladded subwavelength grating,," *IEEE Photonic. Tech. L.*, vol. 16, pp. 518–520, Feb. 2004.

[48] C. F. R. Mateus, M. C. Y. Huang, L. Chen, and C. J. Chang-Hasnain, "Broad-band mirror (1.12-1.62 μm) using a subwavelength grating," *IEEE Photonic. Tech. L.*, vol. 16, pp. 1676–1678, July 2004.

[49] R. Cetin and T. Akin, "Numerical and experimental investigation into LWIR transmission performance of complementary silicon subwavelength antireflection grating (SWARG) structures," *Sci. Rep.*, vol. 9, no. 4683, 2019.

[50] K. J. Lee, R. LaComb, B. Britton, M. Shokooh-Saremi, H. Silva, E. Donkor, Y. Ding, and R. Magnusson, "Silicon-layer guided-mode resonance polarizer with 40-nm bandwidth," *IEEE Photonic. Tech. L.*, vol. 20, no. 22, pp. 1857–1859, 2008.

[51] Y. Long, L. Shen, H. Xu, H. Deng, and Y. Li, "Achieving ultranarrow graphene perfect absorbers by exciting guided-mode resonance of one-dimensional photonic crystals," *Sci. Rep.*, vol. 6, no. 32312, 2016.

[52] J. Nie, J. Yu, W. Liu, T. Yu, and P. Gao, "Ultra-narrowband perfect absorption of monolayer two-dimensional materials enabled by all-dielectric subwavelength gratings," *Opt. Express*, vol. 28, no. 26, pp. 28592–38602, 2020.

[53] M. V. N. Surendra Gupta, E. Ameen, S. Unnikrishnakurap, K. Balasubramaniam, A. Veeraragavan, and B. Pesala, "Spectral filtering of sub-bandgap radiation using all-dielectric gratings for thermophotovoltaic applications," *J. Photonics Energy*, vol. 11, p. 015501, Jan. 2021.

[54] R. Magnusson and Y. H. Ko, "Guided-mode resonance nanophotonics: fundamentals and applications," in *Proceedings Volume 9927, Nanoengineering, Fabrication, Properties, Optics, and Devices XIII*, vol. 992702, (San Diego, CA, USA), SPIE, 2016.

[55] K. E. Hege, D. O'Connell, W. Johnson, S. Basty, and E. L. Dereniak, "Hyperspectral imaging for astronomy and space surveillance," in *Imaging Spectrometry IX*, vol. 5159, (San Diego, CA), pp. 380–391, SPIE, Jan. 2004.

[56] M.-A. Gagnon, P. Tremblay, S. Savary, M. Duval, P. Lagueux, and M. Chamberland, "Airborne thermal infrared hyperspectral imaging of gases," in *6th Workshop on Hyperspectral Image and Signal Processing: Evolutionin Remote Sensing (WHISPERS)*, (Lausanne, Switzerland), June 2014.

[57] R. S. Allison, J. M. Johnston, G. Craig, and S. Jennings, "Airborne optical and thermal remote sensing for wildfire detection and monitoring," *Sensors*, vol. 16, p. 29, Aug. 2016.

[58] M. Govender, K. Chetty, and H. Bulcock, "A review of hyperspectral remote sensing and its application in vegetation and water resource studies," *Water SA*, vol. 33, no. 2, pp. 145–151, 2007.

[59] E. Adam, O. Mutanga, and D. Rugege, "Multispectral and hyperspectral remote sensing for identification and mapping of wetland vegetation: a review," *Wetlands Ecol. Manage.*, vol. 18, no. 3, pp. 281–296, 2010.

[60] C. Fischer and I. Kakoulli, "Multispectral and hyperspectral imaging technologies in conservation: current research and potential applications," *Stud. Conserv.*, vol. 7, pp. 3–16, 2006.

[61] M. Kamruzzaman, G. ElMasry, D.-W. Sun, and P. Allen, "Non-destructive prediction and visualization of chemical composition in lamb meat using NIR hyperspectral imaging and multivariate regression," *Innov. Food Sci. Emerg. Technol.*, vol. 16, pp. 218–226, Oct. 2016.

[62] N. Panigrahi, C. S. Bhol, and B. S. Das, "Rapid assessment of black tea quality using diffuse reflectance spectroscopy," *J. Food Eng.*, vol. 190, pp. 101–108, 2016.

[63] R. Schuler, P. Kish, and C. Plese, "Preliminary observations on the ability of hyperspectral imaging to provide detection and visualization of bloodstain patterns on black fabrics," *J. Forensic Sci.*, vol. 57, no. 6, pp. 1562–1569, 2012.

[64] S. Boubanga-Tombet, A. Huot, I. Vitins, S. Heuberger, C. Veuve, F. Marcotte, and M. Chamberland, "Thermal infrared hyperspectral imaging for mineralogy mapping of a mine face," *Remote Sens.*, vol. 10, p. 15, Sept. 2018.

[65] O. Carrasco, R. B. Gomez, A. Chainani, and W. E. Roper, “Hyperspectral imaging applied to medical diagnoses and food safety,” in *Geo-Spatial and Temporal Image and Data Exploitation III*, vol. 5097, (Orlando, FL), pp. 215–221, 2003.

[66] M. A. Afromowitz, J. B. Callis, D. M. Heimbach, L. A. DeSoto, and M. K. Norton, “Multispectral imaging of burn wounds: a new clinical instrument for evaluating burn depth,” *IEEE Trans. Biomed. Eng.*, vol. 35, no. 10, pp. 842–850, 1988.

[67] G. Lu and B. Fei, “Medical hyperspectral imaging: a review,” *J. Biomed. Opt.*, vol. 19, p. 23, Jan. 2014.

[68] M. Barrow and J. D. Phillips, “Mid-wave infrared filtering in silicon subwavelength zero-contrast gratings,” in *High Contrast Metastructures IX*, vol. 11290, (San Francisco, CA), p. 112900K, International Society for Optics and Photonics, Feb. 2020.

[69] M. Scherr, M. Barrow, and J. D. Phillips, “Influence of finite grating size on guided mode resonance transmission filters,” in *2018 IEEE Photonics Conference (IPC)*, (Reston, VA), p. 2, IEEE, Oct. 2018.

[70] M. Barrow and J. D. Phillips, “Polarization-independent narrowband transmittance filters via symmetry-protected modes in high contrast gratings,” *Opt. Lett.*, vol. 45, no. 15, pp. 4348–4351, 2020.

[71] T. Aflalo, S. Kellis, C. Klaes, B. Lee, Y. Shi, K. Pejsa, K. Shanfield, S. Hayes-Jackson, M. Aisen, C. Heck, C. Liu, and R. A. Andersen, “Decoding motor imagery from the posterior parietal cortex of a tetraplegic human,” *Science*, vol. 348, pp. 906–910, May 2015.

[72] B. Pesaran, M. Vinck, G. T. Einevoll, A. Sirota, P. Fires, M. Siegel, W. Truccolo, C. E. Schroeder, and R. Srinivasan, “Investigating large-scale brain dynamics using field potential recordings: analysis and interpretation,” *Nat. Neurosci*, vol. 21, pp. 903–919, July 2018.

[73] G. K. Anumanchipalli, J. Chartier, and E. F. Chang, “Speech synthesis from neural decoding of spoken sentences,” *Nature*, vol. 568, pp. 493–501, Apr. 2019.

[74] J. L. Collinger, B. Wodlinger, J. E. Downey, W. Wang, E. C. Tyler-Kabara, D. J. Weber, A. J. C. McMorland, M. Velliste, M. L. Boninger, and A. B. Schwartz, “High-performance neuroprosthetic control by an individual with tetraplegia,” *Lancet*, vol. 381, pp. 557–564, Feb. 2013.

[75] A. B. Ajiboye, F. R. Willett, D. R. Young, W. D. Memberg, B. A. Murphy, J. P. Miller, B. L. Walter, J. A. Sweet, H. A. Hoyen, M. W. Keith, P. H. Peckham, J. D. Simeral, J. P. Donoghue, L. R. Hochberg, and R. F. Kirsch, “Restoration of reaching and grasping movements through brain-controlled muscle stimulation in a person with tetraplegia: a proof-of-concept demonstration,” *Lancet*, vol. 389, pp. 1821–1830, May 2017.

[76] Z. T. Irwin, K. E. Schroeder, P. P. Vu, A. J. Bullard, D. M. Tat, C. S. Nu, A. Vaskov, S. R. Nason, D. E. Thompson, and J. N. Bentley, “Neural control of finger movement via intracortical brain-machine interface,” *J. Neural Eng.*, vol. 14, p. 11, Oct. 2017.

[77] L. F. Nicolas-Alonso and J. Gomez-Gil, “Brain computer interfaces, a review,” *Sensors*, vol. 12, no. 2, pp. 1211–1279, 2012.

[78] J. Lee, E. Mok, J. Huang, L. Cui, A.-H. Lee, V. Leung, P. Mercier, S. Shellhammer, L. Larson, P. Asbeck, R. Rao, Y.-K. Song, A. Nurmikko, and F. Laiwalla, “An implantable wireless network of distributed microscale sensors for neural applications,” in *9th International IEEE EMBS Conference on Neural Engineering*, (San Francisco, CA), IEEE, 2019.

[79] J. Lee, F. Laiwalla, J. Jeong, C. Kilfoyle, L. Larson, A. Nurmikko, S. Li, S. Yu, and V. W. Leung, “Wireless power and data link for ensembles of sub-mm scale implantable sensors near 1GHz,” in *2018 IEEE Biomedical Circuits and Systems Conference (BioCAS)*, (Cleveland, OH), IEEE, Oct. 2018.

[80] M. M. Ghanbari, D. K. Piech, K. Shen, S. F. Alamouti, C. Yalcin, B. C. Johnson, J. M. Carmena, M. M. Maharbiz, and R. Muller, “A 0.08mm^2 ultrasonic implantable wireless neural recording system with linear AM backscattering,” in *2019 IEEE International Solid-State Circuits Conference (ISSCC)*, (San Francisco, CA), pp. 284–286, Feb. 2019.

[81] S. L. Jacques, “Corrigendum: Optical properties of biological tissues: a review,” *Phys. Med. Biol.*, vol. 58, pp. 37–61, May 2013.

[82] A. J. Cortese, C. L. Smart, T. Wang, M. F. Reynolds, S. L. Norris, Y. Ji, S. Lee, A. Mok, C. Wu, F. Xia, N. I. Ellis, A. C. Molnar, C. Xu, and P. L. McEuen, “Microscopic sensors using optical wireless integrated circuits,” *Proc. Natl. Acad. Sci. U S A*, vol. 117, pp. 9173–9179, Apr. 2020.

[83] K. W. Yang, K. Oh, and S. Ha, “Challenges in scaling down of free-floating implantable neural interfaces to millimeter scale,” *IEEE Access*, vol. 8, pp. 133295–133320, 2020.

[84] J. Lim, E. Moon, M. Barrow, S. R. Nason, P. R. Patel, P. G. Patil, S. Oh, H.-S. Kim, D. Sylvester, D. Blaauw, C. A. Chestek, J. D. Phillips, and T. Jang, “A 0.19$\times$0.17mm^2 wireless neural recording IC for motor prediction with near-infrared-based power and data telemetry,” in *2020 IEEE International Solid-State Circuits Conference*, (San Francisco, CA), pp. 416–418, IEEE, Feb. 2020.

[85] E. Moon, D. Blaauw, and J. D. Phillips, “Infrared energy harvesting in millimeter-scale GaAs photovoltaics,” *IEEE Trans. Electron. Devices*, vol. 64, pp. 4554–4560, Sept. 2017.

[86] E. Moon, D. Blaauw, and J. D. Phillips, “Subcutaneous photovoltaic infrared energy harvesting for bio-implantable devices,” *IEEE Trans. Electron. Devices*, vol. 64, pp. 2432–2437, Mar. 2017.

[87] M. Eunseong, M. Barrow, J. Lim, J. Lee, S. Nason, J. Costello, H. S. Kim, T. Jang, C. Chestek, D. Blaauw, and J. Phillips, “Bridging the ”last millimeter” gap of brain-machine interfaces via near-infrared wireless power transfer and data communications,” *ACS Photonics*, 2021.

[88] S. S. Wang and R. Magnusson, “Theory and applications of guided-mode resonance filters,” *Appl. Opt.*, vol. 32, pp. 2606–2613, May 1993.

[89] V. Karagodsky and C. J. Chang-Hasnain, “Physics of near-wavelength high contrast gratings,” *Opt. Express*, vol. 20, pp. 10888–10895, May 2012.

[90] S. M. Rytov, “Electromagnetic properties of a finely stratified medium,” *J. Exp. Theor. Phys.*, vol. 2, p. 466, June 1956.

[91] C. W. Haggans, L. Li, and R. K. Kostuk, “Effective-medium theory of zeroth-order lamellar gratings in conical mountings,” *J. Opt. Soc. Am. A*, vol. 18, no. 8, pp. 1912–1928, 2001.

[92] H. Hemmati and R. Magnusson, “Applicability of Rytov’s full effective-medium formalism to the physical description and design of resonant metasurfaces,” *ACS Photonics*, vol. 7, pp. 3177–3187, 2020.

[93] G. Quaranta, G. Basset, O. J. F. Martin, and B. Gallinet, “Recent advances in resonant waveguide gratings,” *Laser Photonics Rev.*, vol. 12, no. 1800017, 2018.

[94] J. D. Joannopoulos, S. G. Johnson, J. N. Winn, and R. D. Meade, *Photonic Crystals: Molding the Flow of Light*. Princeton University Press, 2nd ed., 2008.

[95] C. Kittel, *Introduction to Solid State Physics*. Wiley, 2004.

[96] L. Sun-Goo and R. Magnusson, “Band flips and bound-state transitions in leaky-mode photonic lattice,” *Phys. Rev. B*, vol. 99, p. 5, Jan. 2019.

[97] A. A. Bogdanov, K. L. Koshelev, P. V. Kapitanova, M. V. Rybin, S. A. Gladyshev, Z. F. Sadrieva, K. B. Samusev, Y. S. Kivshar, and M. F. Limonov, “Bound states in the continuum and Fano resonances in the strong mode coupling regime,” *Advanced Photonics*, vol. 1, no. 1, p. 12, 2019.

[98] A. S. Kupriianov, Y. Xu, A. Sayanskiy, V. Dmitriev, Y. S. Kivshar, and V. R. Tuz, “Metasurface engineering through bound states in the continuum,” *Phys. Rev. Appl.*, vol. 12, p. 8, July 2019.

[99] J. M. Foley and J. D. Phillips, “Normal incidence narrowband transmission filtering capabilities using symmetry-protected modes of a subwavelength, dielectric grating,” *Opt. Lett.*, vol. 40, pp. 2637–2640, June 2015.

[100] X. Cui, H. Tian, Y. Du, G. Shi, and Z. Zhou, “Normal incidence filters using symmetry-protected modes in dielectric subwavelength gratings,” *Sci. Rep.*, vol. 6, p. 6, Nov. 2016.

[101] S. Fan, W. Suh, and J. D. Joannopoulos, “Temporal coupled-mode theory for the Fano resonance in optical resonators,” *J. Opt. Soc. Am. A*, vol. 20, pp. 569–572, Mar. 2003.

[102] J. M. Bendickson, E. N. Glytsis, T. K. Gaylord, and D. L. Brundrett, “Guided-mode resonant subwavelength gratings: effects of finite beams and finite gratings,” *J. Opt. Soc. Am. A*, vol. 18, no. 8, pp. 1912–1928, 2001.

[103] E. Popov, A.-L. Fehrembach, Y. Brûlé, G. Demésy, and P. Boyer, “Two-dimensional grating for narrow-band filtering with large angular tolerances,” *Opt. Express*, vol. 24, pp. 14974–14985, June 2016.

[104] L. Mace, O. Gauthier-Lafaye, A. Monmayrant, and H. Camon, “Design of angularly tolerant zero-contrast grating filters for pixelated filtering in the mid-IR range,” *J. Opt. Soc. Am. A*, vol. 34, pp. 657–665, Jan. 2017.

[105] Y. Ding and R. Magnusson, “Doubly resonant single-layer bandpass optical filters,” *Opt. Lett.*, vol. 29, pp. 1135–1137, May 2004.

[106] A. C. Overvig, S. Shrestha, and N. Yu, “Dimerized high contrast gratings,” *Nanophotonics*, vol. 7, pp. 1157–1168, May 2018.

[107] R. Magnusson, “Wideband reflectors with zero-contrast gratings,” *Opt. Lett.*, vol. 39, pp. 4337–4340, Aug. 2014.

[108] T. K. Gaylord and M. G. Moharam, “Analysis and applications of optical diffraction by gratings,” *Proc. IEEE*, vol. 73, pp. 894–937, 1985.

[109] V. Liu and S. Fan, “S^4 : a free electromagnetic solver for layered periodic structures,” *Comput. Phys. Commun.*, vol. 183, pp. 2233–2244, Oct. 2012.

[110] R. Magnusson and M. Shokooh-Saremi, “Physical basis for wideband resonant reflectors,” *Opt. Express*, vol. 16, pp. 3456–3462, Mar. 2008.

[111] K. F. Man, K. S. Tang, and S. Kwong, “Genetic algorithms: concepts and applications,” *IEEE Trans. Ind. Electron.*, vol. 43, no. 5, pp. 519–534, 1996.

[112] E. D. Palik, *Handbook of Optical Constants of Solids*. Amsterdam, The Netherlands: Elsevier, 1998.

[113] A. Yahata, S. Urano, T. Inoue, and T. Shinohe, “Smoothing of Si trench sidewall surface by chemical dry etching and sacrificial oxidation,” *Jpn. J. Appl. Phys.*

[114] A.-L. Fehrembach, D. Maystre, and A. Sentenac, “Phenomenological theory of filtering by resonant dielectric gratings,” *J. Opt. Soc. Am. A*, vol. 19, pp. 1136–1144, June 2002.

[115] Y. Horie, S. Han, J.-Y. Lee, J. Kim, Y. Kim, A. Arbabi, C. Shin, L. Shi, E. Arbabi, S. M. Kamali, H.-S. Lee, S. Hwang, and A. Faraon, “Visible wavelength color filters using dielectric subwavelength gratings for backside-illuminated CMOS image sensor technologies,” *Nano Lett.*, vol. 17, pp. 3159–3164, Apr. 2017.

[116] O. Boyko, F. Lemarchand, A. Talneau, A.-L. Fehrembach, and A. Sentenac, “Experimental demonstration of ultrasharp unpolarized filtering by resonant gratings at oblique incidence,” *J. Opt. Soc. Am. A*, vol. 26, pp. 676–679, Feb. 2009.

[117] J. W. Yoon and R. Magnusson, “Fano resonance formula for lossy two-port systems,” *Opt. Express*, vol. 21, pp. 17751–17759, July 2013.

[118] E. Bonnet, A. Cachard, A. V. Tishchenko, and O. M. Parriaux, “Scaling rules for the design of a narrow-band grating filter at the focus of a free-space beam,” in *Photonic Crystal Materials and Nanostructures*, vol. 5450, (San Diego, CA, USA), SPIE, 2004.

[119] R. R. Boye and R. K. Kostuk, "Investigation of the effect of finite grating size on the performance of guided-mode resonance filters,," *Appl. Opt.*, vol. 39, pp. 3649–3653, July 2000.

[120] D. W. Peters, S. A. Kemme, and G. R. Hadley, "Effect of finite grating, waveguide width, and end-facet geometry on resonant subwavelength grating reflectivity," *J. Opt. Soc. Am. A*, vol. 21, pp. 981–987, June 2004.

[121] S. Ura, M. Nakata, K. Yanagida, J. Inoue, and K. Kintaka, "Cavity-resonator-integrated guided-mode resonance band-stop reflector," *Opt. Express*.

[122] T. Skauli, P. S. Kuo, K. L. Vodopyanov, T. J. Pinguet, O. Levi, L. A. Eyres, J. S. Harris, and M. M. Fejer, "Improved dispersion relations for GaAs and applications to nonlinear optics," *J. Appl. Phys.*, vol. 94, no. 6447, 2003.

[123] A. Liu, P. Wolf, J.-H. Schulze, and D. Bimberg, "Fabrication and characterization of integrable GaAs-based high-contrast grating reflector and Fabry-Perot filter array with GaInP sacrificial layer," *IEEE Photonics J.*, vol. 8, no. 2700509, 2016.

[124] A. Liu, B. Yang, P. Wolf, J. Zhang, and D. Bimberg, "GaAs-based subwavelength grating on an AlO_x layer for a vertical-cavity surface-emitting laser," *OSA Continuum*, vol. 3, no. 2, pp. 317–324, 2020.

[125] C. Chase, Y. Rao, W. Hofmann, and C. J. Chang-Hasnain, "1550 nm high contrast grating VCSEL," *Opt. Express*, vol. 18, no. 15, pp. 15461–15466, 2010.

[126] B. Hogan, L. Lewis, M. McAuliffe, and S. P. Hegarty, "Mid-infrared optical sensing using sub-wavelength gratings," *Opt. Express*, vol. 27, no. 3, pp. 3169–3179, 2019.

[127] T. Sun, S. Kan, G. Marriott, and C. J. Chang-Hasnain, "High-contrast grating resonators for label-free detection of disease biomarkers," *Sci. Rep.*, vol. 6, p. 7, June 2016.

[128] X.-L. Wang, G.-D. Hao, and T. Takahashi, "Enhancement of the evanescent wave coupling effect in a sub-wavelength-sized GaAs/AlGaAs ridge structure by low-refractive-index surface layers," *Opt. Express*, vol. 22, no. S6, pp. A1559–A1566, 2014.

[129] V. Karagodsky, F. G. Sedgwick, and C. J. Chang-Hasnain, "Theoretical analysis of subwavelength high contrast grating reflectors," *Opt. Express*.

[130] L. Poladian, F. Ladouceur, and P. Miller, "Effects of surface roughness on gratings," *J. Opt. Soc. Am. B*, vol. 14, no. 6, pp. 1339–1344, 1997.

[131] D. S. Rawal, V. R. Agarwal, H. S. Sharma, B. K. Sehgal, R. Muralidharan, and H. K. Malik, "Study of inductively coupled Cl_2/BCl_3 plasma process for high etch rate selective etching of via-holes in GaAs," *Vacuum*, vol. 85, no. 3, pp. 452–457, 2010.

[132] H. Rubin, D. Geerpuram, R. Westerman, M. Buliszak, R. Baskaran, and A. W. Hanson, "The effects of increasing the aspect ratio of GaAs backside vias," in *CS MANTECH Conference*, (Boston, MA), p. 4, Apr. 2012.

[133] K. Booker, Y. O. Mayon, C. Jones, M. Stocks, and A. Blakers, “Deep, vertical etching for GaAs using inductively coupled plasma/reactive ion etching,” *J. Vac. Sci. Technol. B*, vol. 38, no. 012206, 2020.

[134] J. W. Lee, M. W. Devre, B. H. Reelfs, D. Johnson, J. N. Sasserath, F. Clayton, D. Hays, and S. J. Pearton, “Advanced selective dry etching of GaAs/AlGaAs in high density inductively coupled plasmas,” *J. Vac. Sci. Technol. A*, vol. 18, July 2000.

[135] E. W. Berg and S. W. Pang, “Low-pressure etching of nanostructures and via holes using an inductively coupled plasma system,” *J. Electrochem. Soc.*, vol. 146, no. 2, pp. 775–779, 1999.

[136] M. Volatier, D. Duchesne, R. Morandotti, R. Arès, and V. Aimez, “Extremely high aspect ratio GaAs and GaAs/AlGaAs nanowaveguides fabricated using chlorine ICP etching with N_2-promoted passivation,” *Nanotechnology*, vol. 21, no. 134014, 2010.

[137] S. J. Pearton, U. K. Chakrabarti, F. Ren, C. R. Abernathy, A. Katz, W. S. Hobson, and C. Constantine, “New dry-etch chemistries for III-V semiconductors,” *Mater. Sci. Eng. B Solid State Mater. Adv. Technol.*, vol. 25, pp. 179–185, July 1994.

[138] S. Bouchoule, S. Azouigui, S. Guilet, G. Patriarche, L. Largeau, A. Martinez, L. Le Gratiet, A. Lemaitre, and F. LeLarge, “Anisotropic and smooth inductively coupled plasma etching of III-V laser waveguides using HBr-O_2 chemistry,” *J. Electrochem. Soc.*, vol. 155, no. 10, pp. H778–H785, 2008.

[139] K. Hjort, J. Soderkvist, and J.-A. Schweitz, “Gallium arsenide as a mechanical material,” *J. Micromech. Microeng.*, vol. 4, pp. 1–13, Feb. 1994.

[140] J.-H. Kim, D. H. Lim, and G. M. Yang, “Selective etching of AlGaAs/GaAs structures using the solutions of citric acid/ and de-ionized /buffered oxide etch,” *J. Vac. Sci. Technol. B*, vol. 16, pp. 558–560, Jan. 1998.

[141] P. Jiang and K. C. Balram, “Suspended gallium arsenide platform for building large scale photonic integrated circuits: passive devices,” *Opt. Express*, vol. 28, pp. 12262–12271, Apr. 2020.

[142] X. Zhou, I. Kulkova, T. Lund-Hansen, S. L. Hansen, P. Lodahl, and L. Midolo, “High-efficiency shallow-etched grating on GaAs membranes for quantum photonic applications,” *Appl. Phys. Lett.*, vol. 113, Dec. 2018.

[143] S. I. Azzam and A. V. Kildishev, “Photonic bound states in the continuum: from basics to applications,” *Adv. Optical Mater.*, vol. 9, no. 2001469, 2021.

[144] J. von Neumann and E. P. Wigner, “Über merkwürdige diskrete eigenwerte,” *Z. Phys.*, vol. 30, pp. 465–467, 1929.

[145] W. Yang, S. Tianbo, Y. Rao, M. Megens, T. Chan, B.-W. Yoo, D. A. Horsley, M. C. Wu, and C. J. Chang-Hasnain, “High speed optical phased array using high contrast grating all-pass filters,” *Opt. Express*, vol. 22, no. 17, pp. 20038–20044, 2014.

[146] T. Wang and S. Zhang, "Large enhancement of second harmonic generation from transition-metal dichalcogenide monolayer on grating near bound states in the continuum," *Opt. Express*, vol. 26, pp. 322–337, 2018.

[147] A. Kodigala, T. Lepetit, Q. Gu, B. Bahari, Y. Fainman, and B. Kanté, "Lasing action from photonic bound states in the continuum," *Nature*, vol. 541, pp. 196–199, 2017.

[148] C.-L. Zou, J.-M. Cui, F.-W. Sun, X. Xiong, X.-B. Zou, Z.-F. Han, and G.-C. Guo, "Guiding light through optical bound states in the continuum for ultrahigh-Q microresonators," *Laser Photonics Rev.*, vol. 9, no. 1, pp. 114–119, 2014.

[149] D. R. Abujetas, Barreda, F. Moreno, L. Amelie, J.-M. Geffrin, and J. A. Sanchez-Gil, "High-Q transparency band in all-dielectric metasurfaces induced by a quasi bound state in the continuum," *Laser Photonics Rev.*, vol. 15, no. 2000263, 2021.

[150] E. N. Bulgakov, D. N. Maksimov, P. N. Semina, and S. A. Skorobogatov, "Propagating bound states in the continuum in dielectric gratings," *J. Opt. Soc. Am. B*, vol. 35, no. 6, pp. 1218–1222, 1998.

[151] K. Sakoda, "Symmetry, degeneracy, and uncoupled modes in two-dimensional photonic lattices," *Phys. Rev. B*, vol. 52, pp. 7982–7986, Sept. 1995.

[152] J. M. Foley, S. M. Young, and J. D. Phillips, "Symmetry-protected mode coupling near normal incidence for narrow-band transmission filtering in a dielectric grating," *Phys. Rev. B*, vol. 89, p. 9, Apr. 2014.

[153] A. C. Overvig, S. C. Malek, M. J. Carter, S. Shrestha, and N. Yu, "Selection rules for symmetry-protected bound states in the continuum," *March 26, 2019*.

[154] J. W. Yoon, M. J. Jung, S. H. Song, and R. Magnusson, "Analytic theory of the resonance properties of metallic nanoslit arrays," *IEEE J. Quantum Electron.*, vol. 48, pp. 852–861, July 2012.

[155] B. C. P. Sturmberg, K. B. Dossou, L. C. Botten, R. C. McPhedran, and C. Martijn de Sterke, "Fano resonances of dielectric gratings: symmetries and broadband filtering," vol. Opt. Express, p. 24, Nov. 2015.

[156] M. F. Limonov, M. V. Rybin, A. N. Poddubny, and Y. S. Kivshar, "Fano resonances in photonics," *Nat. Photonics*, vol. 11, pp. 543–554, Sept. 2017.

[157] U. Fano, "Effects of configuration interaction on intensities and phase shifts," *Phys. Rev.*, vol. 124, pp. 1866–1878, July 1961.

[158] J. W. Yoon, K. H. Seol, S. H. Song, and R. Magnusson, "Critical coupling in dissipative surface-plasmon resonators with multiple ports," *Opt. Express*, vol. 18, pp. 25702–25711, Dec. 2010.

[159] H. Zhou, B. Zhen, C. W. Hsu, O. D. Miller, S. G. Johnson, J. D. Joannopoulos, and M. Soljacic, "Perfect single-sided radiation and absorption without mirrors," *Optica*, vol. 3, no. 10, pp. 1079–1086, 2016.

[160] D. Wang, Q. Wang, and D. Liu, "Polarization-independent filter for incidence between classic and full conical mountings," *IEEE Photonic. Tech. L.*, vol. 30, pp. 495–498, Mar. 2018.

[161] Y. Fang, W. Hou, and H. Zhang, "Advances in implantable medical device battery," *Chin. J. Med. Instrum.*, vol. 42, no. 4, pp. 272–275, 2018.

[162] J. M. Rabaey, M. Mark, D. Chen, C. Sutardja, C. Tang, S. Gowda, M. Wagner, and D. Werthimer, "Powering and communicating with mm-size implants," in *2011 Design, Automation & Test in Europe*, (Grenoble, France), pp. 1–6, Mar. 2011.

[163] H. Kim, H. Hirayama, S. Kim, K. J. Han, R. Zhang, and J. Choi, "Review of near-field wireless power and communication for biomedical applications," *IEEE Access*, vol. 5, pp. 21264–21285, 2017.

[164] D. Seo, R. Neely, K. Shen, U. Singhal, E. Alon, J. M. Rabaey, J. M. Carmena, and M. M. Maharbiz, "Wireless recording in the peripheral nervous system with ultrasonic neural dust," *Neuron*, vol. 91, pp. 529–539, Aug. 2016.

[165] J. Charthad, M. J. Weber, T. C. Chang, and A. Arbabian, "A mm-sized implantable medical device (IMD) with ultrasonic power transfer and a hybrid bi-directional data link," *IEEE J. Solid-State Circuits*, vol. 50, pp. 1741–1753, Aug. 2015.

[166] D. K. Piech, B. C. Johnson, K. Shen, M. M. Ghanbari, K. Y. Li, R. M. Neely, J. E. Kay, J. M. Carmena, M. M. Maharbiz, and R. Muller, "A wireless millimetre-scale implantable neural stimulator with ultrasonically powered bidirectional communication," *Nature Biomed. Eng.*, vol. 4, no. 2, pp. 207–222, 2020.

[167] E. A. Genina, A. N. Bashkatov, V. I. Kochubey, and V. V. Tuchin, "Optical clearing of human dura mater," *Opt. Spectrosc.*, vol. 98, no. 3, pp. 470–476, 2005.

[168] S. Lee, A. J. Cortese, A. P. Gandhi, E. R. Agger, P. L. McEuen, and A. C. Molnar, "A 250 μm $\times$ 57 μm microscale opto-electronically transduced electrodes (MOTEs) for neural recording," *IEEE Trans. Biomed. Circuits Syst.*, vol. 12, pp. 1256–1266, Dec. 2018.

[169] K. Podgorski and G. Ranganathan, "Brain heating induced by near-infrared lasers during multiphoton microscopy," *J. Neurophysiol.*, vol. 116, pp. 1012–1023, June 2016.

[170] "ANSI14 (LIo, America. American National Standard for Safe Use of Lasers (ANSI Z136. 1). Laser Institute of America, Orlando, Florida (2014)."

[171] E. Moon, M. Barrow, J. Lim, D. Blaauw, and J. D. Phillips, "Dual-junction GaAs photovoltaics for low irradiance wireless power transfer in submillimeter-scale sensor nodes," *IEEE J. Photovolt.*, vol. 10, pp. 1721–1726, Nov. 2020.

[172] V. G. Peters, D. R. Wyman, M. S. Patterson, and G. L. Frank, "Optical properties of normal and diseased human breast tissues in the visible and near infrared," *Phys. Med. Biol.*, vol. 35, pp. 1317–1334, May 1990.

[173] A. N. Bashkatov, E. A. Genina, V. I. Kochubey, Y. P. Sinichkin, A. A. Korobov, N. A. Lakodina, and V. V. Tuchin, "In vitro study of control of human dura mater optical properties by acting of osmotical liquids," in *Controlling Tissue Optical Properties: Applications in Clinical Study*, pp. 182–188, Nov. 2000.

[174] L. Wang, S. L. Jacques, and L. Zheng, "MCML–Monte Carlo modeling of light transport in multi-layered tissues," *Comput. Meth. Prog. Bio.*, vol. 47, pp. 131–146, June 1995.

[175] L. Wang and S. L. Jacques, "Monte Carlo Modeling of Light Transport in Multi-layered Tissues in Standard C-," 1998.

[176] H. Kuchiwaki, S. Inao, N. Ishii, Y. Ogura, and S. Ping, "Human dural thickness measured by ultrasonographic method: reflection of intracranical pressure," *J. Ultrasound Med.*, vol. 16, no. 02, pp. 725–730, 1997.

[177] "AUREA Technologies - Compact NIR Single Photon Detector Dual-mode photon counting solution - OEM design [900 nm - 1700 nm]."

[178] D. Bronzi, F. Villa, S. Tisa, A. Tosi, F. Zappa, D. Durini, S. Weyers, and W. Brockherde, "100 000 Frames/s 64 $\times$ 32 single-photon detector array for 2-D imaging and 3-D ranging," *IEEE J. Sel. Topics Quantum Electron.*, vol. 20, pp. 354–363, Dec. 2014.

[179] H. Haas, C. Chen, and D. O'Brien, "A guide to wireless networking by light," *Prog. Quantum Electron.*, vol. 55, pp. 88–111, Sept. 2017.

[180] E. Moon, D. Blaauw, and J. D. Phillips, "Small-area Si photovoltaics for low-flux infrared energy harvesting," *IEEE Trans. Electron. Devices*, vol. 64, pp. 15–20, Jan. 2017.

[181] A. Spott, E. J. Stanton, N. Volet, J. D. Peters, J. R. Meyer, and J. E. Bowers, "Heterogeneous integration for mid-infrared silicon photonics," *IEEE J. Sel. Top. Quantum Electron.*, vol. 23, no. 6, pp. 1–10, 2017.

[182] Q. Li and K. M. Lau, "Epitaxial growth of highly mismatched III-V materials on (001) silicon for electronics and optoelectronics," *Prog. Cryst. Growth Charact. Mater.*, vol. 63, no. 4, pp. 105–120, 2017.

[183] J. Zhang, G. Muliuk, J. Juvert, S. Kumari, J. Goyvaerts, B. Haq, C. Op de Beeck, B. Kuyken, G. Morthier, D. Van Thourhout, R. Baets, G. Lepage, P. Verheyen, J. Van Campenhout, A. Gocalinska, J. O'Callaghan, E. Pelucchi, K. Thomas, B. Corbett, A. J. Trindade, and G. Roelkens, "III-V-on-Si photonic integrated circuits realized using micro-transfer-printing," *APL Photon.*, vol. 4, p. 10, Nov. 2019.

[184] J. H. Lau, *Through-Silicon Vias for 3D Integration*. New York: McGraw-Hill, 2013.

[185] S. L. Burkett, M. B. Jordan, R. P. Schmitt, L. A. Menk, and A. E. Hollowell, "Tutorial on forming through-silicon vias," *J. Vac. Sci Technol. A*, vol. 38, no. 031202, 2020.

[186] W.-W. Shen and K.-N. Chen, "Three-dimensional integrated circuit (3D IC) key technology: through-silicon via (TSV)," *Nanoscale Res. Lett.*, vol. 12, no. 56, 2017.

[187] J. P. Gambino, S. A. Adderly, and J. U. Knickerbocker, "An overview of through-silicon-via technology and manufacturing challenges," *Microelectron. Eng.*, vol. 135, pp. 73–106, 2015.

[188] H. Stieglauer, E. Dengler, M. Hosch, P. Michel, C. Teyssandier, and H. Blanck, "High aspect ratio individual source through wafer vias for high frequency GaAs pHEMT processes," in *CS MANTECH Conference*, (Scottsdale, AZ), pp. 235–238, 2015.

[189] Q. Weibin and W. Jiaxian, "Highly controllable ICP etching of GaAs based materials for grating fabrication," *J. Semicond.*, vol. 33, p. 026001, Feb. 2012.

[190] L. A. Menk, D. Josell, T. P. Moffat, E. Baca, M. G. Blain, A. Smith, J. Dominguez, J. McClain, P. D. Yeh, and A. E. Hollowell, "Bottom-up copper filling of large scale through silicon vias for MEMS technology," *J. Electrochem. Soc.*, vol. 166, no. 1, pp. D3066–D3071, 2019.

[191] D. Yi, J. Li, and P. Zhu, "Study of nanoscratching process of GaAs using molecular dynamics," *Crystals*, vol. 8, no. 321, 2018.

[192] K.-J. Chui and M. Yu, "Electrical characterization of CMP-less via-last TSV under reliability stress conditions," in *2017 IEEE 67th Electronic Components and Technology Conference*, (Orlando, FL, USA), pp. 1529–1534, IEEE, 2017.

[193] J.-K. Koo and J.-H. Lee, "Electrochemical process for 3D TSV without CMP and lithographic processes," *Electron. Mater. Lett.*, vol. 10, no. 2, pp. 485–490, 2014.

[194] M. S. Chandrasekar and M. Pushpavanam, "Pulse and pulse reverse plating - conceptual, advantages and applications," *Electrochim. Acta*, vol. 53, pp. 3313–3322, Jan. 2008.

[195] P. Leisner, P. Moller, M. Fredenberg, and I. Belov, "Recent progress in pulse reversal plating of copper for electronics applications," *Trans. Inst. Met. Finish.*, vol. 85, no. 1, pp. 40–45, 2007.

[196] F.-Y. Shen, W.-P. Dow, A.-H. Liu, J.-Y. Lin, P.-H. Chang, and S.-M. Huang, "Periodic pulse reverse Cu plating for through-hole filling," *ECS Electrochem. Lett.*, vol. 2, pp. D23–D25, Feb. 2013.

[197] Y.-J. Chen, R.-Y. Chen, Y.-H. Fang, C.-H. Liang, W.-K. Hsu, C.-L. Chen, W.-C. Lin, C.-Y. Weng, J.-Y. Chu, and Y.-J. Chiu, "Hybrid III-V-on-SOI optical spot size convertor by self-aligned selective undercut dry etching of Si," *Opt. Lett.*, vol. 45, pp. 4188–4191, Aug. 2020.

[198] P. C. Andricacos, C. Uzoh, J. O. Dukovic, J. Horkans, and H. Deligianni, "Damascene copper electroplating for chip interconnections," *IBM J. Res. Dev.*, vol. 42, pp. 567–574, Sept. 1998.

[199] C.-H. Ji, F. Herrault, P. Hopper, P. Smeys, P. Johnson, and M. Allen, "Electroplated metal buried interconnect and through-wafer metal-filled via technology for high-power integrated electronics," *IEEE Trans. Adv. Packag.*, vol. 32, pp. 695–702, Aug. 2009.

[200] J. Ortigoza-Diaz, K. Scholten, C. Larson, A. Cobo, T. Hudson, J. Yoo, A. Baldwin, A. W. Hirschberg, and E. Meng, “Techniques and considerations in the microfabrication of parylene C microelectromechanical systems,” *Micromachines*, vol. 9, no. 422, 2018.

[201] A. Lecomte, A. Lecestre, D. Bourrier, B. Marie-Charline, L. Jalabert, E. Descamps, and C. Bergaud, “Deep plasma etching of parylene C patterns for biomedical applications,” *Microelectron. Eng.*, vol. 177, pp. 70–73, 2017.

[202] R. Caldwell, H. Mandal, R. Sharma, F. Solzbacher, P. Tathireddy, and L. Rieth, “Analysis of Al_2O_3-parylene C bilayer coatings and impact of microelectrode topography on long term stability of implantable neural arrays,” *J. Neural Eng.*, no. 046011, 2017.

[203] E. Meng, P.-Y. Li, and Y.-C. Tai, “Plasma removal of parylene C,” *J. Neural Eng.*, vol. 18, no. 045004, 2008.

[204] M. Miao, Y. Zhu, S. Ma, X. Sun, and Y. Jin, “Bottom-up filling of through silicon via (TSV) with parylene as sidewall protection layer,” in *2009 11th Electronics Packaging Technology Conference*, (Singapore), IEEE, 2009.

[205] J. H. Lau, *Flip Chip Technologies*. McGraw-Hill Professional, 1996.

[206] S.-C. Kim and Y.-H. Kim, “Review paper: flip chip bonding with anisotropic conductive film (ACF) and nonconductive adhesive (NCA),” *Curr. Appl. Phys.*, vol. 13, pp. S14–S25, 2013.

[207] J.-W. Nah and K.-W. Paik, “Investigation of flip chip under bump metallization systems of Cu pads,” *IEEE Trans. Compon. Packaging Manuf. Technol.*, vol. 25, no. 1, pp. 33–37, 2002.

[208] J. Easley, C. B. Martin, M. H. Ettenberg, and J. D. Phillips, “InGaAs/GaAsSb type-II superlattices for short-wavelength infrared detection,” *J. Electron Mater.*, vol. 48, no. 10, pp. 6025–6029, 2019.

[209] M.-J. Yim, J.-S. Hwang, W. Kwon, K. W. Jang, and K.-W. Paik, “Highly reliable non-conductive adhesives for flip chip CSP applications,” *IEEE Trans. Electron. Packag. Manuf.*, vol. 26, no. 2, pp. 150–155, 2003.

[210] P. Takmakov, K. Ruda, S. K. Phillips, I. S. Isayeva, V. Krauthamer, and C. G. Welle, “Rapid evaluation of the durability of cortical neural implants using accelerated aging with reactive oxygen species,” *J. Neural Eng.*, vol. 12, no. 026003, 2015.

[211] X. Xie, L. Rieth, L. Williams, S. Negi, R. Bhandari, R. Caldwell, R. Sharma, P. Tathireddy, and F. Solzbacher, “Long-term reliability of Al_2O_3 and parylene C bilayer encapsulated Utah electrode array based neural interfaces for chronic implantation,” *J. Neural Eng.*, vol. 11, no. 026016, 2014.

[212] J. Jeong, F. Laiwalla, J. Lee, R. Ritasalo, M. Pudas, L. Larson, V. Leung, and A. Nurmikko, “Conformal hermetic sealing of wireless microelectronic implantable chiplets by multilayered atomic layer deposition (ALD),” *Adv. Funct. Mater.*, vol. 29, no. 1806440, 2019.

[213] R. Windisch, B. Dutta, M. Kujik, A. Knobloch, S. Meinlschmidt, S. Schoberth, P. Kiesel, G. Borghs, G. H. Dohler, and P. Heremans, "40% efficient thin-film surface-textured light-emitting diodes by optimization of natural lithography," *IEEE Trans. Electron. Devices*, vol. 47, pp. 1492–1498, July 2000.

[214] X.-H. Li, R. Song, Y.-K. Ee, P. Kumnorkaew, J. F. Gilchrist, and N. Tansu, "Light extraction efficiency and radiation patterns of III-nitride light-emitting diodes with colloidal microlens arrays with various aspect ratios," *IEEE Photonics J.*, vol. 3, p. 11, June 2011.

[215] K. Kim, Y. Song, and J. Oh, "Nano/micro dual-textured antireflective subwavelength structures in anisotropically etched GaAs," *Opt. Lett.*, vol. 42, pp. 3105–3108, Aug. 2017.

[216] E. Matioli and C. Weisbuch, "Impact of photonic crystals on LED light extraction efficiency: approaches and limits to vertical structure designs," *J. Phys. D: Appl. Phys.*, vol. 43, p. 22, Apr. 2010.

[217] D. Pudis, L. Suslik, J. Skriniarova, J. Kovac, J. J. Kovac, I. Kubicova, I. Martincek, S. Hascik, and P. Schaaf, "Effect of 2D photonic structure in the LED surface on emission properties," *Appl. Surf. Sci.*, vol. 269, pp. 161–165, Oct. 2013.

[218] S.-H. Chuang, C.-S. Tsung, C.-H. Chen, S.-L. Ou, R.-H. Horng, C.-Y. Lin, and D.-S. Wuu, "Transparent conductive oxide films embedded with plasmonic nanostructure for light-emitting diode applications," *ACS Appl. Mater. Interfaces*, vol. 7, pp. 2546–2553, Jan. 2015.

[219] M. Boroditsky, R. Vrijen, T. F. Krauss, R. Coccioli, R. Bhat, and E. Yablonovitch, "Spontaneous emission extraction and Purcell enhancement from thin-film 2-D photonic crystals," *J. Light. Technol.*, vol. 17, pp. 2096–2112, Nov. 1999.

[220] E. Higurashi, T. Imamura, T. Suga, and R. Sawada, "Low-temperature bonding of laser diode chips on silicon substrates using plasma activation of Au films," *IEEE Photon. Technol. Lett.*, vol. 19, no. 24, pp. 1994–1996, 2007.